National Aeronautics and Space Administration

HELIOPHYSICS MISSION CONCEPT STUDY FOR THE 2024–2033 DECADAL SURVEY

INTERMESO

A Mission to Untangle Dynamic Mesoscale Structures Throughout the Heliosphere

SEPTEMBER 2022

Robert C. Allen, Principal Investigator
Robert.Allen@jhuapl.edu

Evan J. Smith, Mission Systems Engineer
Evan.Smith@jhuapl.edu

JOHNS HOPKINS
APPLIED PHYSICS LABORATORY

www.nasa.gov

22-04030

Data Release, Distribution, and Cost Interpretation Statements

This document is intended to support the 2024–2033 Solar and Space Physics (Heliophysics) Decadal Survey.

The data contained in this document may not be modified in any way.

Cost estimates described or summarized in this document were generated as part of a preliminary concept study, are model-based, assume a Johns Hopkins Applied Physics Laboratory (APL) in-house build, and do not constitute a commitment on the part of APL.

Cost reserves for development and operations were included as prescribed by the NASA ground rules for the Heliophysics Mission Concept Studies program. Unadjusted estimate totals and cost reserve allocations would be revised as needed in future more-detailed studies as appropriate for the specific cost-risks for a given mission concept.

Acknowledgments

The Johns Hopkins Applied Physics Laboratory would like to thank all of the InterMeso team members, the National Academies of Sciences, Engineering, and Medicine Solar and Space Physics (Heliophysics) Decadal Survey 2024–2033, and the NASA Heliophysics Division for supporting this study.

ROLE	NAME	AFFILIATION
Science Team		
Leadership	Robert C. Allen, Principal Investigator	APL
	Andy Santo, Project Management	APL
	Juliana Vievering, Hard X-ray instrumentation lead	APL
	Sarah K. Vines, Magnetometry lead	APL
	Lan Jian, Data management lead	GSFC
	Gang Li, Theory & Modeling lead	UAH
	Sue Lepri, Thermal to suprathermal ion composition lead	U. Mich
	Robert Wimmer-Schweingruber, Energetic particle lead	CAU
	David Malaspina, E-fields lead	LASP
	Phyllis Whittlesey, Low-energy electron lead	SSL
Science	Brian Anderson	APL
	George Ho	APL
	Parisa Mostafavi	APL
	Lynn Wilson	GSFC
	Stefano Livi	U. Mich
	Jim Raines	U. Mich
	Sämuel Krucker	FHNW
	Joseph Borovsky	SSI
	Daniel Verscharen	UCL
	Bennett Maruca	UD
	Noé Lugaz	UNH
Engineering Team		
Study Design Lead/Mission Systems Engineer	Evan Smith	APL
Systems	Clint Apland	APL
	Max Harrow	APL
Mission Design	Fazle Siddique	APL
	Ryan Bull	APL
Cost	Larry Wolfarth	APL
Schedule	Steve Price	APL
Guidance and Control	Jack Hunt	APL
	Brett Shapiro	APL
Power	Cristina Vigil	APL
	Tonle Bloomer	APL
Mechanical	Lisa Wu	APL
Designer	Kim Vodusek	APL
Thermal	Daniel Jeong	APL
Radio-Frequency Communications	Matt Cox	APL
Avionics	Mike Hoffman	APL
Flight Software/Automation	Nigel Tzeng	APL
Propulsion	Seth Kijewski	APL
Integration and Testing	Joe Pulkowski	APL
Ground	Mike Furrow	APL
	Bobby Seng	APL
Operations	Sarah Hamilton	APL
Radiation	Justin Likar	APL
Harness	Kyle Norman	APL

Mission Concept Study for the 2024–2033 Heliophysics Decadal Survey

INTERMESO

A Mission to Untangle Dynamic Mesoscale Structures Throughout the Heliosphere

Mesoscale dynamics are a fundamental science priority in space physics that fall within an observational gap of past, present, and planned missions. In the solar wind, mesoscales (spatial scales of 0.5 Mkm to tens of Mkm) are crucial for understanding the connection of the solar corona to an observer anywhere within the heliosphere. Exploring these scales also reveals the still-unresolved physics regulating particle acceleration and transport, interplanetary magnetic field topology, and the causes for variability in the composition and acceleration of solar wind plasma.

InterMeso addresses this fundamental knowledge gap through a constellation of four spacecraft in Earth-trailing heliocentric orbits near 1 au with observations spanning the mesoscale range. InterMeso can achieve its goals through robust, high-heritage architectures and instrumentation and with mission costs well within the scope of the Solar Terrestrial Probes program.

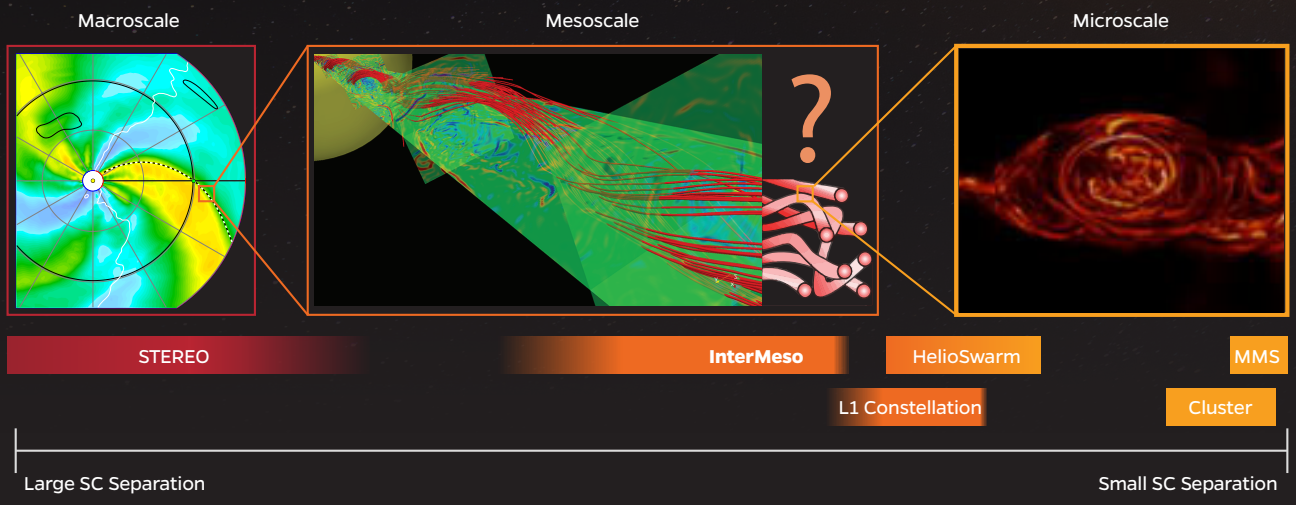

INTERMESO SCIENCE OBJECTIVE

Investigate the fundamental mesoscale nature of the variable solar wind and impacts on particle acceleration, evolution, and transport.

SCIENCE GOALS

1. Explore and identify the origin of the mesoscale variability of the background solar wind and transient solar wind structures
2. Understand and characterize the impact of these mesoscale variations on particle acceleration and transport

MISSION TIMELINE

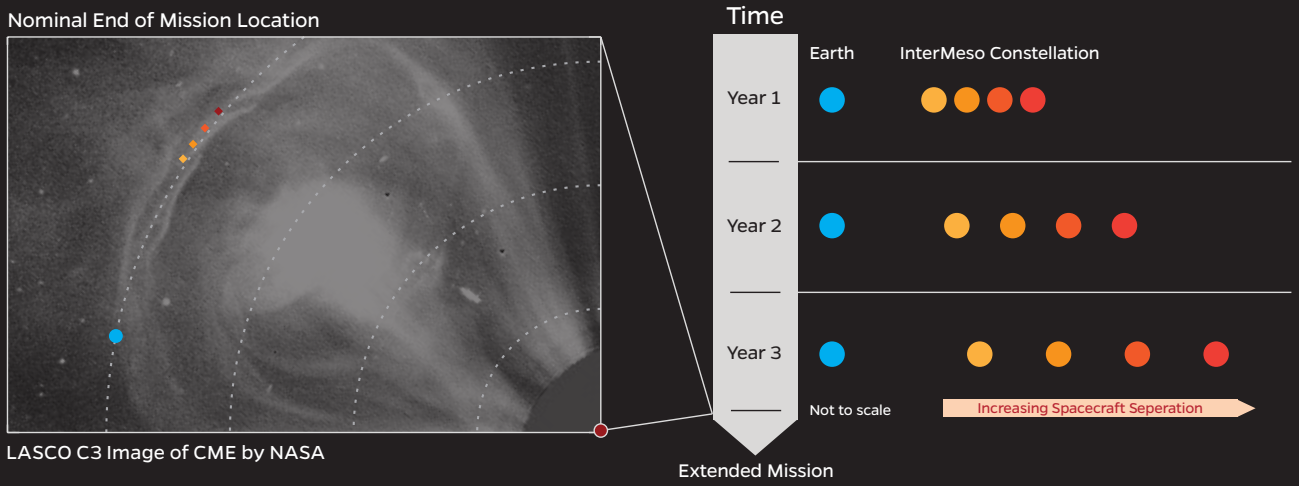

A MISSION TO UNTANGLE DYNAMIC MESOSCALE STRUCTURES THROUGHOUT THE HELIOSPHERE

SPACECRAFT CHARACTERISTICS

- Four spacecraft launched on a single Falcon 9 Reusable Launch Vehicle (56% total mass margin, 338.43 kg dry mass per spacecraft)
- Direct heliocentric orbit injection (1.52 km^2/s^2 C3) simplifies operations, total deterministic delta-V budget less than 50 m/s
- Robust, low-complexity spacecraft use high-heritage components in a single-string, selectively redundant implementation
- Three-axis stabilization enables uninterrupted science data collection during the 3-year science phase (44-month total mission duration)
- Ka-band science downlink returns a total mission data volume of 5.5 TB from all four spacecraft (1.38 TB per spacecraft)

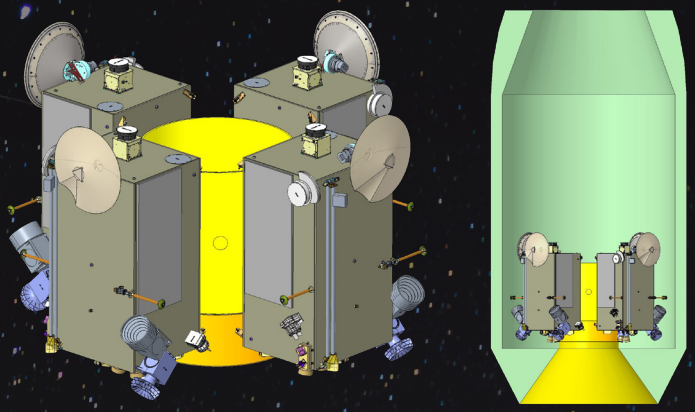

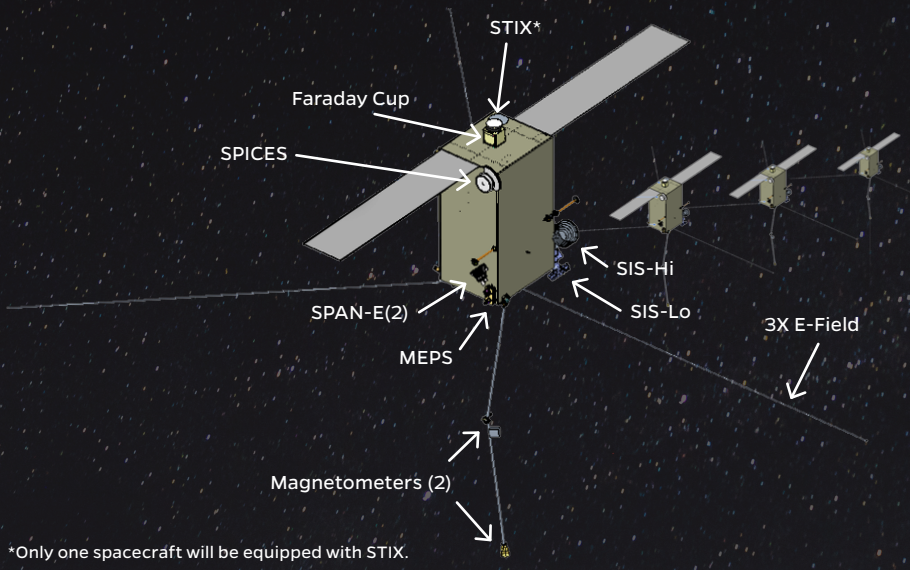

*Only one spacecraft will be equipped with STIX.

INSTRUMENTATION

- Bulk Solar Wind—Faraday Cup
- Thermal Ion Composition—SPICES
- Suprathermal Ion Composition—SIS-Lo
- Energetic Ion Composition—SIS-Hi
- Low Energy Electrons—SPAN-E
- Energetic Electrons—MEPS
- Magnetic Fields—Fluxgate Magnetometer
- AC Electric Fields & Radio—SWAVES
- Hard X-Ray—STIX*

COST

	FY$22K without LV	FY$22K with LV
A–D Subtotal	552,700	753,400
A–D Reserves	273,300	273,300
A–D PIMMC	826,000	1,026,700
E Subtotal	88,300	88,300
E Reserves	22,100	22,100
E PIMMC	110,400	101,400
Total PIMMC	**936,400**	**1,137,100**

PHASE A–D COSTS FOR RECENT SOLAR TERRESTRIAL PROBES MISSIONS

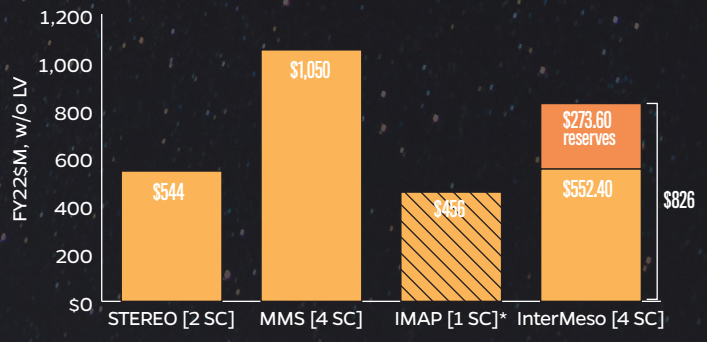

*Not including reserves, currently in development

APL JOHNS HOPKINS APPLIED PHYSICS LABORATORY

Heliophysics Decadal Survey

InterMeso Mission Concept Design Study Final Report

Table of Contents

Acknowledgments ii

Executive Summary 1

1. Scientific Investigation 2

1.1 Solar Terrestrial Probes Science Objective 2

1.2 Mission Concept Science Objectives 3

1.2.1 Obj. 1: Characterize and identify the origin of the mesoscale variability of the background solar wind and transient solar wind structures 3

1.2.2 Obj. 2: Characterize and understand the impact of these mesoscale variations on particle acceleration and transport 5

1.2.3 Significance, Impact, and Timeliness 8

1.3 Mission Concept Science Traceability 10

2. Mission Concept Investigation 14

2.1 Overview 14

2.2 Concept Maturity Level 14

2.3 Technology Maturity 14

2.4 Key Trades 15

3. Technical Overview 15

3.1 Instrument Payload Description 15

3.2 Flight System 15

3.2.1 Mechanical 15

3.2.2 Thermal 17

3.2.3 Propulsion 17

3.2.4 Attitude Control 17

3.2.5 Avionics 18

3.2.6 Flight Software 18

3.2.7 Radio-Frequency (RF) Communications 19

3.2.8 Power Generation, Storage, and Distribution 19

3.2.9 Redundancy and Fault Tolerance 20

3.3 Mission Design and Concept of Operations 21

3.3.1 Mission Design Overview 21

3.3.2 Launch and Commissioning Phase 22

3.3.3 Science Phase 23

3.3.4 Extended Mission 24

3.3.5 Concept of Operations Analogies 24

3.4 Ground-Based Observatories 24

3.5 Risk List 25

4. Development Schedule and Schedule Constraints 25
4.1 High-Level Mission Schedule 25
4.2 Science, Technology Development Plan(s) 26
4.3 Development Schedule and Constraints 26
5. Mission Life-Cycle Cost 27
5.1 Costing Methodology and Basis of Estimate 27
5.2 Cost Estimate 28
5.2.1 Phase E and Extended Mission Cost Estimates 29
5.2.2 Summary 29
Appendix A: APL Margin and Risk Definitions 30
Appendix B: Detailed Schedule (Phases B–D) 31
Appendix C: Detailed Instrument Descriptions 32
Appendix D: Supplemental Mission Design and Navigation Information 38
Appendix E: Supplemental Cost Estimate Information 39
References 46
List of Acronyms 51

List of Exhibits

Exhibit 1-1. (a) Modeled representation of typical topology of magnetic structures on the solar surface (adapted from Bian and Li, 2021). (b) As these structures convect outward to 1 au, they can undergo processes such as expansion and stochastic meandering but may preserve their characteristics as granule to supergranule relics on the Sun (cartoon adapted from Borovsky, 2008). The nature of flux tube structure at 1 au remains a fundamental open question. 3

Exhibit 1-2. The power spectral density of magnetic field fluctuations at time of solar wind plasma beta near 1 au shows two spectral breaks (see Verscharen et al., 2019). The injection range is characterized by a power spectral density slope of $(1/\lambda)^{-1}$, while the inertial range has a slope of $(1/\lambda)^{-5/3}$ in the spacecraft frame. The critical frequencies marked are the correlation length (f_{tc}), proton inertial length (f_{dp}) and ion-gyro scale (f_{rp}), and the electron inertial length (f_{de}) and electron-gyro scale (f_{re}). While the upcoming HelioSwarm mission will explore the transition between the inertial and dissipation ranges (tan region), InterMeso, for the first time, will reveal the spatiotemporal dynamics between the injection and inertial range (yellow region). Adapted from Verscharen et al. (2019). 4

Exhibit 1-3. (a) Relevant scale sizes of CME structures at 1 au (from Ala-Lahti et al., 2020). The fraction of 20–126 keV ion time intensity profiles that remain unchanged between two observing points as a function of spacecraft separation both (b) in the plane of the shock and (c) along the shock normal shows distinct variability that may be related to the variable scale sizes of CME sub-structuring (from Neugebauer et al., 2006). The mesoscale structuring and subsequent effects on particle acceleration remain outstanding open questions in heliophysics. 5

Exhibit 1-4. (a) Simulation of large-scale CME structure near 1 au yielding (b) longitudinal variations in event-integrated particle spectra. (c) Mesoscale structuring of a CME shock inferred from radio wave observations (adapted from Bale et al., 1999) with (d) potential observations from four spacecraft highlighting variations and impacts on particle dynamics. Mesoscale structuring of CMEs and effects on particle acceleration are poorly understood and cannot be addressed by previous, current, or planned missions. 6

Exhibit 1-5. (a) Release times of energetic electrons for various path lengths and energies (dots) with onset-to-peak (peak-to-end) phases of hard X-rays represented by the green and gray dashed regions. (b–d) Yohkoh/HXT hard X-ray observations of the flare related to the energetic electron observations with red contouring (d) from GOES soft X-ray. Adapted from Li et al. (2020). Comparisons between multipoint observations of hard X-ray and energetic electrons are needed to constrain coronal dynamics. 7

Exhibit 1-6. (a) Field line meandering (from Ashraf and Li, 2019) and (b) stochastic motion (from Bian and Li, 2021) are important mechanisms that cause the location of energetic electrons reaching 1 au to dramatically deviate from the nominal Parker Spiral. The relative contributions of these processes on particle transport are unknown but are critical to understanding particle dynamics. 7

Exhibit 1-7. (a) The location of the STEREO spacecraft during a flare event and (b) the approximate footpoint of both spacecraft relative to the flare site. (c–e) Energetic electron observations at both spacecraft showing clear differences at 1 au over 10's degrees of longitude. Adapted from Klassen et al. (2016). Transport of energetic electrons from flare sites to 1 au is complex and requires multipoint measurements at mesoscale separations to constrain. 8

Exhibit 1-8. (a) Cartoon of the observation locations relative to a CIR-associated reverse shock inferred from (b) energetic particle spectra (adapted from Zhao et al., 2016). (c) Distributed observations at mesoscale separations are needed to (d) constrain the transport effect on particle spectra without ambiguities from temporal evolution (adapted from Mason et al., 1999). 9

Exhibit 1-9. Mesoscale dynamics are fundamental to solar wind dynamics, enabling interaction between macro- and micro-scale dynamics, but currently fall within an observational gap. Left panel from Allen et al. (2020), middle panel adapted from Maruca et al. (2021), and right panel from Lazarian et al. (2020). InterMeso targets fundamental knowledge gaps of solar wind dynamics and structure at these critical scale lengths. 9

Exhibit 1-10. The convective thickness of structures requires sub-minute resolution to explore the mesoscale variability of the solar wind. 10
Exhibit 1-11. Randomized placement of a four-spacecraft constellation throughout both a Gaussian (top row) and Sigmoidal (bottom row) distribution allows for different functional fits. Filled-in circles in the top row are examples of the 1000 random placements of spacecraft constellations resulting in the shown colored fits. The solid black curve on the top row is the corresponding fit from the shown example placements. The initial distribution the fits are attempting to recreate is shown by the dashed curve. Four spacecraft are the optimal benefit-to-cost configuration for mesoscale variations. 11
Exhibit 1-12. InterMeso Science Traceability Matrix. 13
Exhibit 2-1. Key trades table. 14
Exhibit 3-1. Payload mass and power table. 15
Exhibit 3-2. Flight system element mass and power table. 16
Exhibit 3-3. InterMeso spacecraft block diagram. 16
Exhibit 3-4. Visualization of the four InterMeso spacecraft integrated onto an ESPA-Grande equivalent launch configuration, allowing for single manifest within a 5-m fairing. 17
Exhibit 3-5. STEREO reaction wheel MetGlass covers satisfied magnetic cleanliness requirements. This mitigation tactic allows for the use of reaction wheels on InterMeso without compromising the need for a magnetically clean spacecraft. 18
Exhibit 3-6. InterMeso will use high-heritage FSW architecture without the need for significant software development. 19
Exhibit 3-7. Initial surface charging analysis of an InterMeso spacecraft at 1 au. Current charging mitigation procedures can accommodate the cleanliness requirements for low energy electron measurements by SPAN-E. 20
Exhibit 3-8. Fault tolerance table. 20
Exhibit 3-9. Flight system element summary table. 21
Exhibit 3-10. Baseline mission timetable. 21
Exhibit 3-11. Spacecraft configuration relative to Earth at the end of the nominal mission. InterMeso will explore the range of mesoscale separations in the pristine solar wind while maintaining a relatively close proximity to Earth. 22
Exhibit 3-12. (a) Change in Earth-relative drift rate over the course of the mission. The “initial” line represents the drift rate targeted by the launch vehicle. (b) Cumulative combined days the InterMeso spacecraft will spend at different inter-spacecraft separations over the prime mission (black) plus extended mission (red). Cumulative combined days is the sum of the number of days spent at each separation for each spacecraft pair (i.e., spacecraft 1&2, 1&3, 1&4, 2&3, 2&4, and 3&4). 22
Exhibit 3-13. Mission design table. 23
Exhibit 3-14. Mission operations and ground data systems table. 24
Exhibit 3-15. Risk list. 25
Exhibit 3-16. Risk table. 25
Exhibit 4-1. InterMeso phase and review date summary. 26
Exhibit 4-2. Mission-level milestones. 26
Exhibit 4-3. InterMeso phase and review date summary. 26
Exhibit 4-4. InterMeso has significant schedule margin above normal institutional requirements, lowering risk. 27
Exhibit 4-5. Schedule margin table. 27
Exhibit 5-1. Cost methodology table. 28
Exhibit 5-2. Estimated Phase A–E costs for the InterMeso mission (in millions of FY22 dollars) by WBS element. 28

Exhibit 5-3. Phase A–D cost of InterMeso with 50% reserves compared to the previous three STP-class missions. InterMeso is well within the family of costs for the STP program. 29
Exhibit 5-4. Estimated Phase A–D InterMeso budget profile table (in millions of FY22 dollars). Cells may not add across due to rounding. 29
Exhibit A-1. Definition of risk likelihood. 30
Exhibit A-2. Definition of risk consequence 30
Exhibit B-1. Detailed InterMeso schedule for Phases B–D. 31
Exhibit C-1. Photo of the Europa Clipper PIMS Faraday cup used as the basis for InterMeso. InterMeso would only require one cup with less shielding. Currently TRL 7 with pathway to higher TRL after launch in 2024. 32
Exhibit C-2. InterMeso Faraday cup specifications. 32
Exhibit C-3. Schematic of the InterMeso SPICES instrument, currently under NASA-funded development to TRL 6 by September 2022. 33
Exhibit C-4. InterMeso SPICES specifications. 33
Exhibit C-5. Photo of the SIS-Lo prototype, currently TRL 6. 33
Exhibit C-6. InterMeso SIS-Lo specifications. 34
Exhibit C-7. Photos of SIS-Hi prototype components, currently TRL 6. 34
Exhibit C-8. InterMeso SIS-Hi specifications. 34
Exhibit C-9. Photo of the PSP SPAN-B instrument, which is a single SPAN-E telescope. InterMeso will fly an exact copy of this proven technology, currently TRL 9. 35
Exhibit C-10. InterMeso SPAN-E specifications. 35
Exhibit C-11. Schematics of MEPS with the 8 FOVs shown. With heritage drawing from instruments such as Solar Orbiter EPT, this instrument is currently TRL 6. 35
Exhibit C-12. InterMeso MEPS specifications. 35
Exhibit C-13. Heritage fluxgate magnetometer from STEREO. The InterMeso FGM-boom assembly is currently TRL 8. 36
Exhibit C-14. InterMeso FGM specifications. 36
Exhibit C-15. Electric field stacers from STEREO/WAVES. The InterMeso electric field antennas are currently TRL 7. 36
Exhibit C-16. InterMeso E-Fields instrument specifications. 37
Exhibit C-17. Photo of Solar Orbiter STIX. The InterMeso STIX is currently TRL 8. 37
Exhibit C-18. InterMeso STIX specifications. 37
Exhibit D-1. Earth–Sun–Probe angle for each spacecraft (left) and the relative separation between the first spacecraft and the remaining three over the course of the mission (right). 38
Exhibit D-2. Reconstructed orbit determination uncertainty in radial, in-track, and cross-track directions along with the residual sum of squares (RSS) during the science orbit. 38
Exhibit E-1. Percentage of nonrecurring and recurring costs by subsystem, based on the median of the STEREO and VAP missions. 40
Exhibit E-2. Estimated instrument costs (in millions of FY22 dollars). 41
Exhibit E-3. Estimated costs of four InterMeso spacecraft (in millions of FY22 dollars). 43
Exhibit E-4. Monte Carlo results of mission cost (in billions of FY22 dollars). 44
Exhibit E-5. Spacecraft subsystem cost growth from start of Phase B to end of Phase D for multi-spacecraft STEREO and VAP missions. 45

Executive Summary

Mesoscale dynamics are a fundamental process in space physics, but fall within an observational gap of current and planned missions. Particularly in the solar wind, measurements at the mesoscales (hundreds of R_E to a few degrees heliographic longitude at 1 au) are crucial for understanding the connection between the corona and an observer anywhere within the heliosphere. Mesoscale dynamics may also be key to revealing the currently unresolved physics regulating particle acceleration and transport, magnetic field topology, and the causes of variability in the composition and acceleration of solar wind plasma. Studies using single-point observations do not allow for investigations into mesoscale solar wind dynamics and plasma variability, nor do they allow for the exploration of the sub-structuring of large-scale solar wind structures like coronal mass ejections (CMEs), corotating/stream interaction regions (CIRs/SIRs), and the heliospheric plasma sheet.

The Interplanetary Mesoscale Observatory (InterMeso) mission seeks to ***investigate the fundamental mesoscale nature of the variable solar wind and its impacts on particle acceleration, evolution, and transport*** through addressing its two science objectives:

1) Characterize and identify the origin of the mesoscale variability of the background solar wind and transient solar wind structures.
2) Characterize and understand the impact of these mesoscale variations on particle acceleration and transport.

To address this fundamental gap in our knowledge of the heliosphere at these scales, the Interplanetary Mesoscale Observatory (InterMeso) concept employs a multipoint approach using four identical spacecraft in Earth-trailing orbits near 1 au. Varying drift speeds of the InterMeso spacecraft enable the mission to span a range of mesoscale separations in the solar wind, achieving significant and innovative science return. Simultaneous, longitudinally separated measurements of structures corotating over the spacecraft also allow for disambiguation of spatiotemporal variability, tracking of the evolution of solar wind structures, and determination of how the transport of energetic particles is impacted by these variabilities.

The payload of each InterMeso spacecraft must measure the bulk solar wind plasma populations and magnetic field, as well as the suprathermal-to-energetic particle content, including composition. Hard X-ray measurements from at least one spacecraft are also required to provide measurements of flare-related processes, release times, and connections to accelerated particles at 1 au. Radio and Langmuir wave observations are also required to trace the connectivity of the spacecraft to a solar source as well as to characterize the in situ plasma and wave environments. As such, the notional payload of each InterMeso spacecraft consists of a vector magnetometer, ion composition and electron detectors spanning thermal to energetic ranges, and alternating current (AC) electric field instrumentation. One of the spacecraft will also carry a hard X-ray indirect imager. Combining these multipoint observations, taken throughout and/or along large-scale structures, elucidates spatial sub-structure in the magnetic field and particle populations and effects of that variation on acceleration.

InterMeso is a Solar Terrestrial Probes-class mission for consideration of inclusion in the 2024-2033 Solar and Space Physics Decadal Survey. This report details the point design for InterMeso, currently at a concept maturity level of 4, including spacecraft, trajectory, payload and accommodations, launch vehicle, and mission life cycle cost.

1. Scientific Investigation

1.1 Solar Terrestrial Probes Science Objective

The solar wind is a multi-scale and highly dynamic system with interplay between the micro-, meso-, and macro-scales. Decades of single-point observations have led to great insight into the large-scale variability in the solar wind and its transient phenomena, such as coronal mass ejections (CMEs), stream and corotating interaction regions (SIR/CIRs), and solar energetic particle (SEP) events associated with flares and/or CMEs. These observations have revealed differences between high-speed streams originating from coronal holes, typical slow solar wind, and Alfvénic slow solar wind (see *D'Amicis et al.*, 2019) and established the current paradigm under which the solar wind is interpreted today.

Previous studies from the Solar Terrestrial Relations Observatory (STEREO) mission and other serendipitous multipoint observations have allowed investigations of spatial variations of the solar wind and transients over large distances. For instance, the radial evolution of the expanding solar wind has been studied statistically using observations from Helios (*Perrone et al.*, 2018), while the radial evolution of CIRs has been studied within the orbit of Earth (e.g., *Richter & Luttrell*, 1986; *Schwenn*, 1990; *Jian et al.*, 2008; *Allen et al.*, 2021a,b) and between Earth and Mars (e.g., *Geyer et al.*, 2021). Multipoint observations of CIRs, and their associated energetic particles, over large longitudinal separations have also revealed significant temporal evolution of the structures as they corotate over tens of degrees longitude (*Mason et al.*, 2009; *Jian et al.*, 2019; *Allen et al.*, 2021a). Additionally, radial (e.g., *Burlaga et al.*, 1981; *Liewer et al.*, 2020) and longitudinal (e.g., *Kilpua et al.*, 2009; *Farrugia et al.*, 2011; *Kollhoff et al.*, 2021) studies of CME structures have found significant variations over these large separations.

On smaller, ion kinetic scales (<1000 km), the solar wind and transients have been found to be highly turbulent and structured, with clear signs of coupling processes over a large range of spatiotemporal scales (e.g., *Bandyopadhyay et al.*, 2018; *Roberts et al.*, 2020). While the Magnetospheric Multiscale (MMS) and Cluster missions, designed to target kinetic scales, have demonstrated the importance and richness of small-scale and highly dynamic plasma processes, these scales are "on the receiving end" of the turbulent cascade that is driven by the large-scale solar wind structures (*Verscharen et al.*, 2019). As such, the intermediate scale, between the small, kinetic-scale dynamics explored by MMS and Cluster, and the larger scale structuring and variations observed by STEREO and multi-mission comparisons, represents the critical scale needed to understand cross-scale processes in the solar wind. *This intermediate scale—the mesoscale—is crucial for understanding the connection of the corona to an observer anywhere within the heliosphere*, as well as for revealing the currently unresolved physics regulating particle transport, magnetic field topology, and the variability in composition and acceleration of solar wind plasma.

The mesoscale solar wind currently falls within a gap both observationally and in spatiotemporal scales of current simulations, and as such is a critical missing link in our fundamental understanding of the heliosphere. A new mission targeting this critical gap of mesoscale dynamics would enable investigations into how solar sources imprint themselves into the solar wind at 1 au and beyond via mesoscale structuring, how mesoscale variability evolves as it propagates from the Sun, and how the intrinsic structure of the solar wind impacts the structure of transients and particle acceleration and transport. The mesoscale regime of the solar wind may likely be the missing piece to long-sought questions of sources of solar wind, particle acceleration, and particle transport. Gaining the ability to probe the mesoscale solar wind will allow for leaps in our understanding of these outstanding questions.

As such, we pose the following Solar Terrestrial Probes (STP) Science Objective: Investigating the fundamental mesoscale nature of the variable solar wind and its impacts on particle acceleration, evolution, and transport.

Targeted Science Questions for Obj. 1: Characterize and identify the origin of the mesoscale variability of the background solar wind and transient solar wind structures

1. What do the predominant scale sizes of the mesoscale solar wind and interplanetary magnetic field (IMF) reveal about the origins of these structures?
2. How do large-scale, persistent structures transition into dynamic turbulence?
3. How do mesoscale variabilities of the solar source manifest variations in seed particle properties and composition at 1 au?
4. How does the mesoscale solar wind imprint itself on solar wind transients and interplanetary shock structures?

Impact: Understanding the structure of the solar wind and transients is fundamental for determining the connection and evolution of plasma and fields from the solar surface to any location in the heliosphere (e.g., Mars' atmosphere).

1.2 Mission Concept Science Objectives

To address the STP Science Objective of *Investigating the fundamental mesoscale nature of the variable solar wind and its impacts on particle acceleration, evolution, and transport*, the Heliophysics community requires a mission to: (1) Characterize and identify the origin of the mesoscale variability of the background solar wind and transient solar wind structures and (2) Characterize and understand the impact of these mesoscale variations on particle acceleration and transport.

1.2.1 Obj. 1: Characterize and identify the origin of the mesoscale variability of the background solar wind and transient solar wind structures

The solar surface exhibits structure on granule and supergranule scales (shown by the model results in **Exhibit 1-1a**). As solar magnetic structures convect out with the solar wind, they can undergo meandering due to footpoint motion, reconnection, and, possibly more importantly at 1 au, stochastic motion and turbulent evolution (e.g., *Borovsky*, 2008; *Ashraf & Li*, 2019; *Bian & Li*, 2021). As such, once flux tubes reach 1 au, they can be tangled into a complex meso-structure (illustrated in **Exhibit 1-1b**) (*Borovsky*, 2008). These processes and structuring can lead to various effects, such as "dropout" phenomena in energetic particles (*Mazur et al.*, 2000). *However, the fundamental structuring and coherence of flux tubes in interplanetary space remain largely unknown.*

Moving from the large-scale structures to mesoscale and smaller ranges, the nature of injection range fluctuations in the solar wind is not well understood, nor is the transition at the break point between the injection range and the inertial range (see the review by *Verscharen et al.*, 2019). Persistent, large-scale structures may transition to

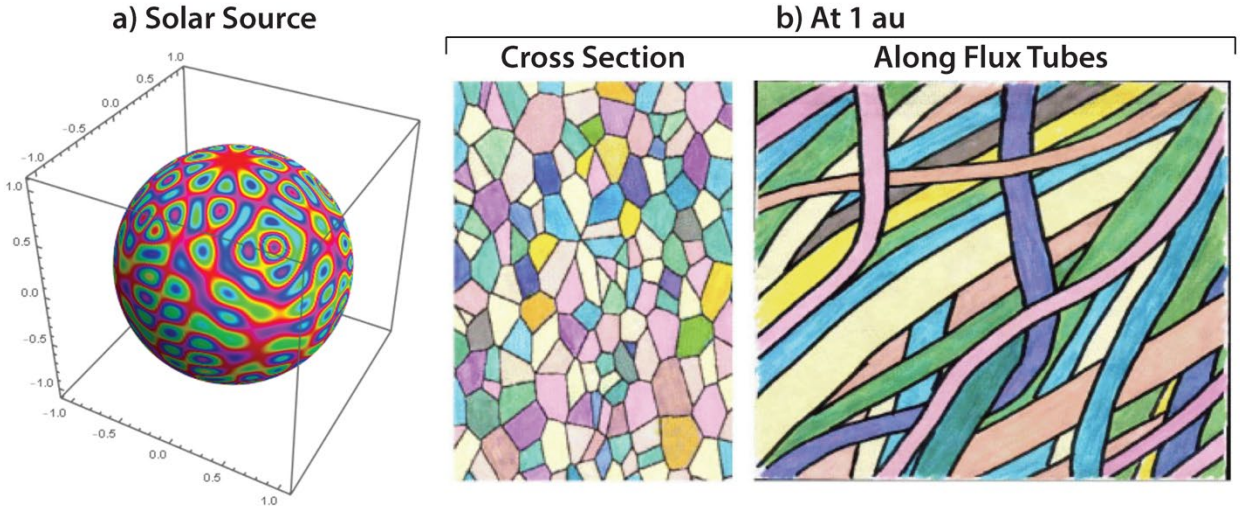

Exhibit 1-1. *(a) Modeled representation of typical topology of magnetic structures on the solar surface (adapted from* Bian and Li*, 2021). (b) As these structures convect outward to 1 au, they can undergo processes such as expansion and stochastic meandering but may preserve their characteristics as granule to supergranule relics on the Sun (cartoon adapted from* Borovsky*, 2008).* The nature of flux tube structure at 1 au remains a fundamental open question.

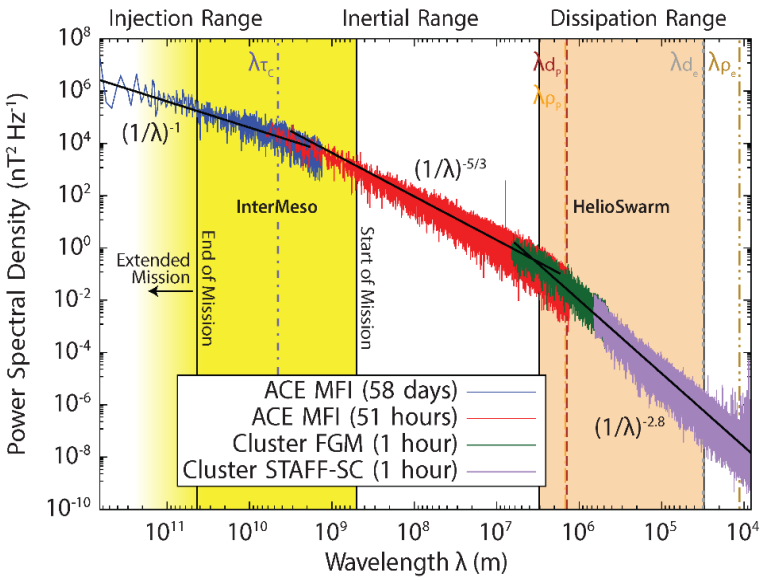

Exhibit 1-2. *The power spectral density of magnetic field fluctuations at time of solar wind plasma beta near 1 au shows two spectral breaks (see* Verscharen et al.*, 2019). The injection range is characterized by a power spectral density slope of $(1/\lambda)^{-1}$, while the inertial range has a slope of $(1/\lambda)^{-5/3}$ in the spacecraft frame. The critical frequencies marked are the correlation length (f_{tc}), proton inertial length (f_{dp}) and ion-gyro scale (f_{rp}), and the electron inertial length (f_{de}) and electron-gyro scale (f_{re}). While the upcoming HelioSwarm mission will explore the transition between the inertial and dissipation ranges (tan region),* InterMeso, for the first time, will reveal the spatiotemporal dynamics between the injection and inertial range *(yellow region). Adapted from* Verscharen et al. *(2019).*

dynamic structures at scales near 10^9–10^{10} m (**Exhibit 1-2**). However, this critical transitionary scale between injection range and inertial ranges has been elusive from a single-spacecraft vantage point, as these observations are limited in the ability to distinguish temporal variations and those resulting from convection of spatially variable solar wind over an observer. While the currently planned HelioSwarm mission will, for the first time, robustly explore the spatiotemporal transition between the inertial range and dissipation range, the injection-to-inertial range transition will remain unexplored. HelioSwarm is a NASA Heliophysics Medium-Class Explorer (MIDEX) mission currently in development that aims to study solar wind turbulence (at scales of 50–3000 km), and consists of nine spacecraft (one hub and eight node spacecraft) in a lunar resonant orbit (see https://eos.unh.edu/helioswarm/mission for additional details). *Only through multipoint observations with separations on the order of this critical scale can we robustly explore this fundamental transition in the solar wind.*

In addition to the currently unconstrained, fundamental mesoscale structuring of the solar wind, sub-structuring of transient events is also not well understood. The small number of studies that have utilized fortuitous, but sporadic, multi-mission conjunctions to investigate the mesoscale structuring of CME shocks have shown that CME-associated shocks and magnetic ejecta have smaller-scale structuring, although the degree of such structuring is largely not understood (e.g., *Bale et al.*, 1999; *Knock et al.*, 2003; *Pulupa & Bale*, 2008; *Koval & Szabo*, 2010, *Lugaz et al.*, 2018). As shown in **Exhibit 1-3a**, the various scale lengths of the solar wind, CME sheath, and CME ejecta are expected to be different from one another (*Ala-Lahti et al.*, 2020). Additionally, comparisons of shocks between the Advanced Composition Explorer (ACE) and Wind missions have found that energetic particle time-intensity profiles often change over mesoscales indicating important effects of mesoscale structuring on particle acceleration and transport (**Exhibit 1-3b** and **1-3c**, *Neugebauer et al.*, 2006). *Observations such as these indicate that the "large-scale-only" view of the solar wind is an incomplete picture of the fundamental structure of the solar wind and the important processes that define its evolution. Dedicated multipoint observations are needed to reveal these fundamental physical processes.*

Current, past, and planned multipoint missions have separations that are either too large or too small to investigate mesoscale structuring. For example, while MMS and Cluster missions have begun to unravel kinetic-scale solar wind variations, and future contributions from the HelioSwarm mission will allow for in-depth investigations into solar wind turbulence, all of these missions have too small inter-spacecraft separations to study mesoscale structuring and dynamics. Missions such as STEREO, along with opportune conjunctions between various assets in the Heliophysics System Observatory are, on the other hand, often at distances too large for mesoscale and cross-scale physics. *As such, new multipoint observations are required to disambiguate spatiotemporal structuring at this critical spatial range spanning ~0.5 Mkm to tens of Mkm.*

Targeted Science Questions for Obj. 2: Characterize and understand the impact of these mesoscale variations on particle acceleration and transport

1. How does mesoscale solar wind variability and intermittency impact variability in particle acceleration?
2. How does mesoscale structuring of solar wind transients and interplanetary shocks affect particle acceleration?
3. How do mesoscale variations of the background solar wind impact the connectivity of an observer to the solar source or acceleration site?
4. How do mesoscale dynamics such as field line meandering and stochastic motion affect the diffusion of particles in the solar wind?

Impact: Constraining the effect of mesoscale structuring on particle acceleration and transport is key in advancing our understanding of energetic particle populations within the heliosphere.

1.2.2 Obj. 2: Characterize and understand the impact of these mesoscale variations on particle acceleration and transport

Particle acceleration is fundamentally dependent upon local conditions in the acceleration regions and, as such, mesoscale variations in the solar wind and along/within transients will affect acceleration processes. For example, a CME expanding into solar wind streams with spatial pressure variations may lead to deformation of its structure (e.g., *Owens et al.*, 2017), resulting in spatially varying shock structure in the mesoscale range. Such mesoscale variations along a shock surface led to localized differences in shock parameters affecting particle acceleration, and so could potentially explain the variations observed in **Exhibit 1-3b-c**. *Detailed observations at multiple points along such structures are required to determine the mesoscale effect on CME particle acceleration.*

Radio wave observations have demonstrated the presence of mesoscale variations in shock structure (e.g., *Bale et al.*, 1999; **Exhibit 1-4c**); however, it remains unknown to what degree the mesoscale structuring affects particle acceleration. While current models can reproduce large-scale variation in event-integrated particle

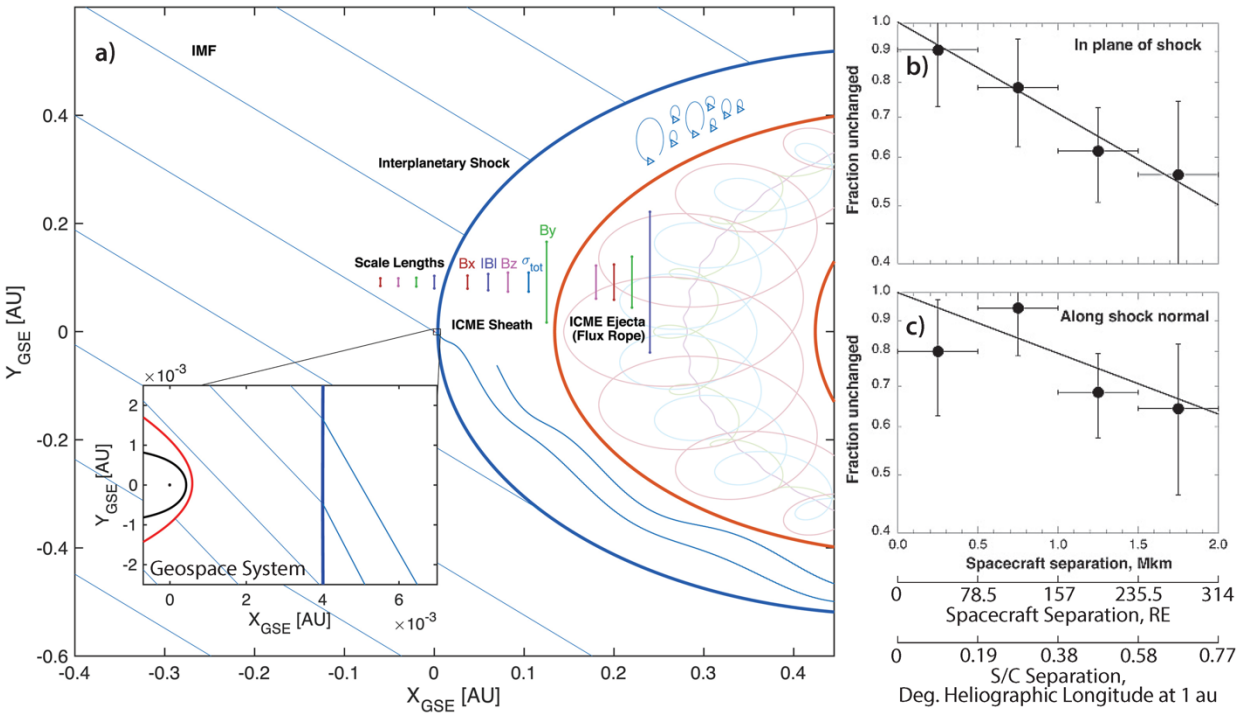

Exhibit 1-3. *(a) Relevant scale sizes of CME structures at 1 au (from* Ala-Lahti et al.*, 2020). The fraction of 20–126 keV ion time intensity profiles that remain unchanged between two observing points as a function of spacecraft separation both (b) in the plane of the shock and (c) along the shock normal shows distinct variability that may be related to the variable scale sizes of CME sub-structuring (from* Neugebauer et al.*, 2006).* The mesoscale structuring and subsequent effects on particle acceleration remain outstanding open questions in heliophysics.

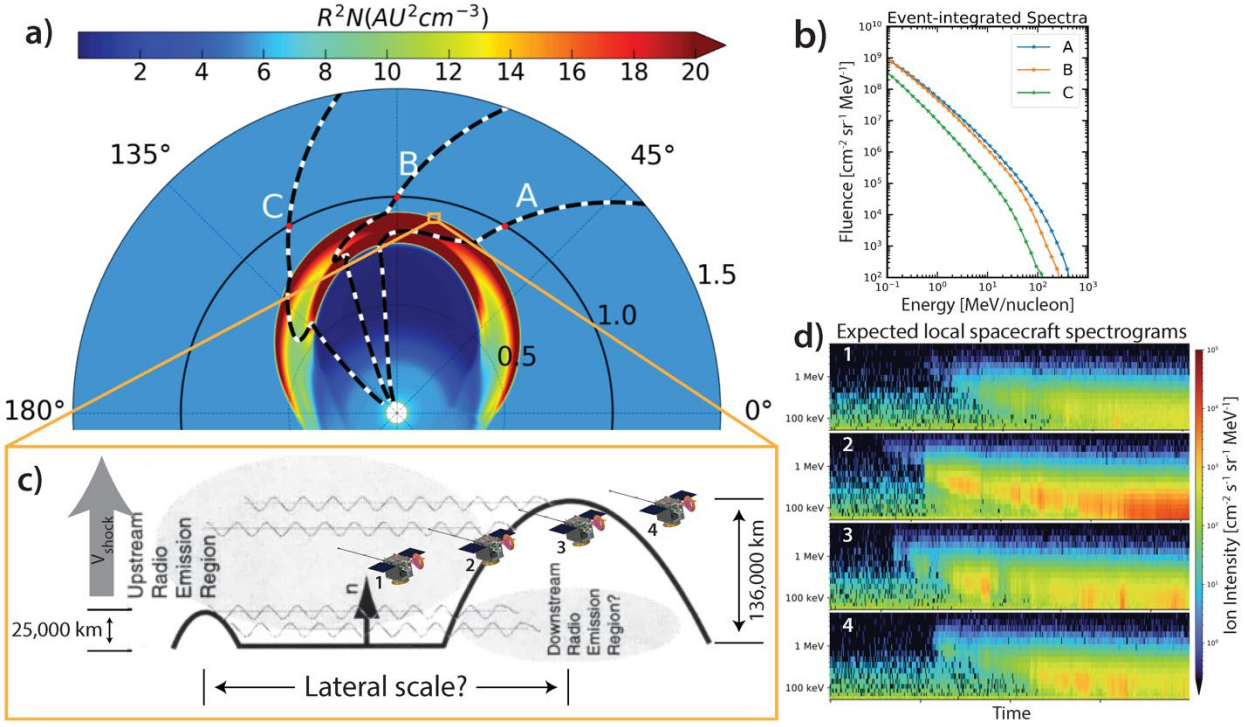

Exhibit 1-4. *(a) Simulation of large-scale CME structure near 1 au yielding (b) longitudinal variations in event-integrated particle spectra. (c) Mesoscale structuring of a CME shock inferred from radio wave observations (adapted from* Bale et al.*, 1999) with (d) potential observations from four spacecraft highlighting variations and impacts on particle dynamics.* Mesoscale structuring of CMEs and effects on particle acceleration are poorly understood and cannot be addressed by previous, current, or planned missions.

spectra along an interplanetary shock (**Exhibit 1-4a-b**), which have been observed by conjunctions of spacecraft at large separations (e.g., *Hu et al.*, 2018), these approaches are unable to capture the effects of mesoscale structuring or short time cadence evolution (**Exhibit 1-4d**). For example, an event-integrated spectra includes particles accelerated from various locations along the shock structure, but the seed populations and freshly accelerated ions will be more localized to the mesoscale variations of the structure. *Better understanding the role that mesoscale structure plays in controlling the variability of particle acceleration along an interplanetary shock is critical for investigating the causes of observed variation between events and potential seed populations.*

Additionally, our understanding of flare acceleration of energetic electrons will be greatly advanced through a robust exploration of mesoscale particle variations. For instance, *Li et al.* (2020) found that the injection timing of energetic electrons compared to hard X-ray observations suggests the presence of two distinct electron populations in an impulsive solar energetic electron event (**Exhibit 1-5**). The presence or absence of these electron populations can differentiate between different types of magnetic reconnection at the flare site (e.g., interchange reconnection versus reconnection between two closed field lines). However, the determination of the path length that the energetic electrons traversed from the flare to the observer is the primary source of ambiguity in these observations, which may be a result of mesoscale variations impacting particle transport. For example, field line meandering and/or stochastic motion can lead to uncertainties of where a source region maps to of up to 10° in longitude at 1 au (**Exhibit 1-6b**, *Bian & Li*, 2021). Observing energetic electrons at multiple spacecraft with a close separation (<10° total span) will allow for the determination of acceleration time scales of electrons at solar flares, through fractional velocity dispersion analysis (FVDA, *Zhao et al.*, 2019) or other analysis techniques, and so for differentiating among proposed reconnection mechanisms. *Along with insight into in situ acceleration mechanisms at 1 au, new multipoint observations at mesoscale separations will provide critical constraints on the flare-related particle acceleration processes.*

The complexities of transport between the corona and 1 au are apparent in impulsive SEP events. For example, when the two STEREO spacecraft were within 34° heliographic longitude of one another in 2014 (**Exhibit 1-**

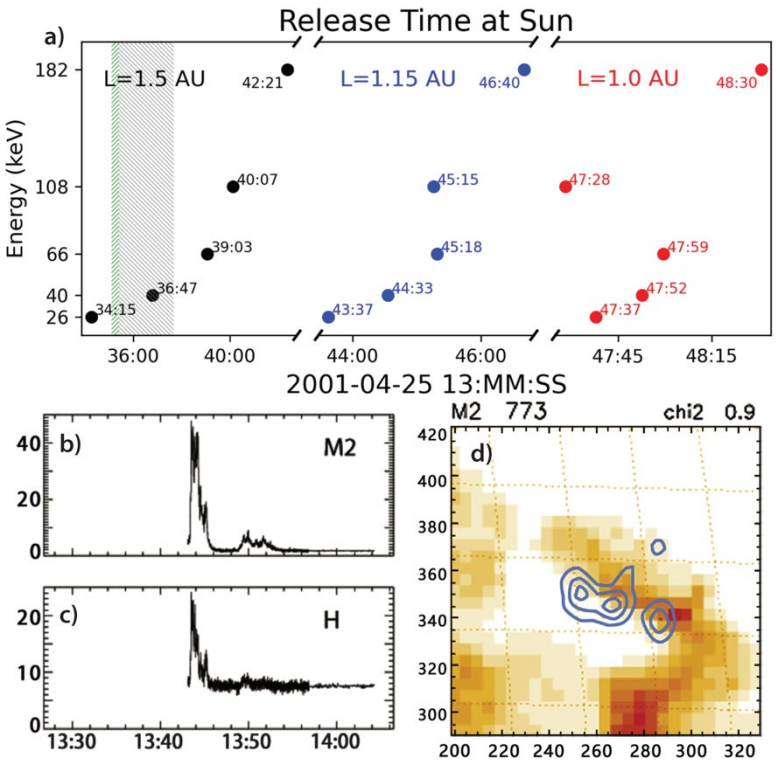

Exhibit 1-5. *(a) Release times of energetic electrons for various path lengths and energies (dots) with onset-to-peak (peak-to-end) phases of hard X-rays represented by the green and gray dashed regions. (b–d) Yohkoh/HXT hard X-ray observations of the flare related to the energetic electron observations with red contouring (d) from GOES soft X-ray. Adapted from* Li et al. *(2020).* Comparisons between multipoint observations of hard X-ray and energetic electrons are needed to constrain coronal dynamics.

7a), a flare event occurred at an active region near the footpoints of both spacecraft (**Exhibit 1-7b**). During this event, as shown in **Exhibit 1-7c**, STEREO-A, despite the footpoint being slightly further from the active region, observed a higher peak in 55–65 keV electron intensity with an onset time about an hour earlier, and with higher anisotropy, than STEREO-B (*Klassen et al.*, 2016). Because transport of flare-accelerated energetic electrons depends on background solar wind structure, particle acceleration at flare sites, and the mechanisms driving cross-field diffusion, this event presents a clear example of the importance of mesoscale variations on the transport of energetic electrons from the flare site in the corona to 1 au. *As such, a robust multipoint investigation at mesoscale separations is required to disentangle the complexities of particle transport in the inner heliosphere.*

For particle transport from local acceleration sites associated with transients, mesoscale variations may also play an important role. As energetic particles propagate along a field line away from an acceleration site, such as from reverse shocks at CIRs, various processes (e.g., adiabatic cooling and particle scattering) leading to hardening of the lower-energy spectra are thought to occur (e.g., *Fisk & Lee*, 1980). However, this spectral hardening has not been observed as often, or as significantly, as expected (e.g., *Mason & Sanderson*, 1999; *Desai et al.*, 2020; *Allen et al.*, 2021a; *Joyce et al.*, 2021). To explain this discrepancy, several theories have been developed, such as compressive, non-shock-related acceleration (e.g., *Giacalone et al.*, 2002; *Fisk & Gloeckler*, 2006; *Ebert et al.*, 2012; *Chen et al.*, 2015) and/or modifications to the magnetic topology, such as sub-Parker spirals (e.g., *Murphy et al.*, 2002; *Schwadron*, 2002; *Schwadron et al.*, 2020).

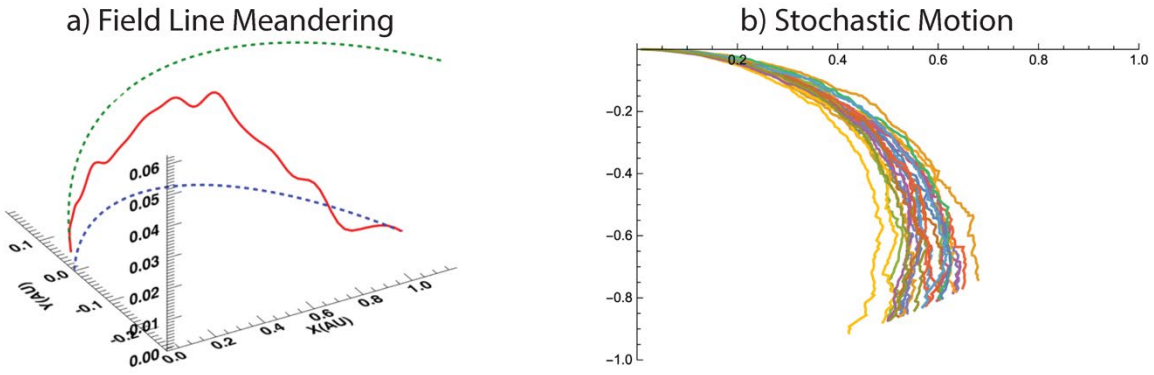

Exhibit 1-6. *(a) Field line meandering (from* Ashraf and Li*, 2019) and (b) stochastic motion (from* Bian and Li*, 2021) are important mechanisms that cause the location of energetic electrons reaching 1 au to dramatically deviate from the nominal Parker Spiral.* The relative contributions of these processes on particle transport are unknown but are critical to understanding particle dynamics.

While these other processes may explain the observed weak modulation of the particle spectra, a CIR observation utilizing a fortuitous multi-spacecraft vantage point seems to suggest strong path-length-dependent modulation (*Zhao et al.*, 2016; **Exhibit 1-8a-b**). In this event, a CIR shock was observed at STEREO-B when it was ~23° from Earth, however the shock was not observed at ACE, and the CIR evolved too significantly relative to STEREO-A for comparison. STEREO-B and ACE measurements indicate strong path-dependent modulation of the observed particle spectra (**Exhibit 1-8b**). However, the required assumption of negligible temporal evolution of the CIR between observations does not fully capture the possible variations of the shock and dynamics regulating particle acceleration and transport, adding ambiguity to the findings. Constraining the true path length to the reverse shock and spatiotemporal variations of shock-related acceleration is difficult with single-point observations. *Only simultaneous, multipoint observations from different points within a CIR and its rarefaction region allows for differentiation between path-length-dependent modulation and competing transport and acceleration processes.*

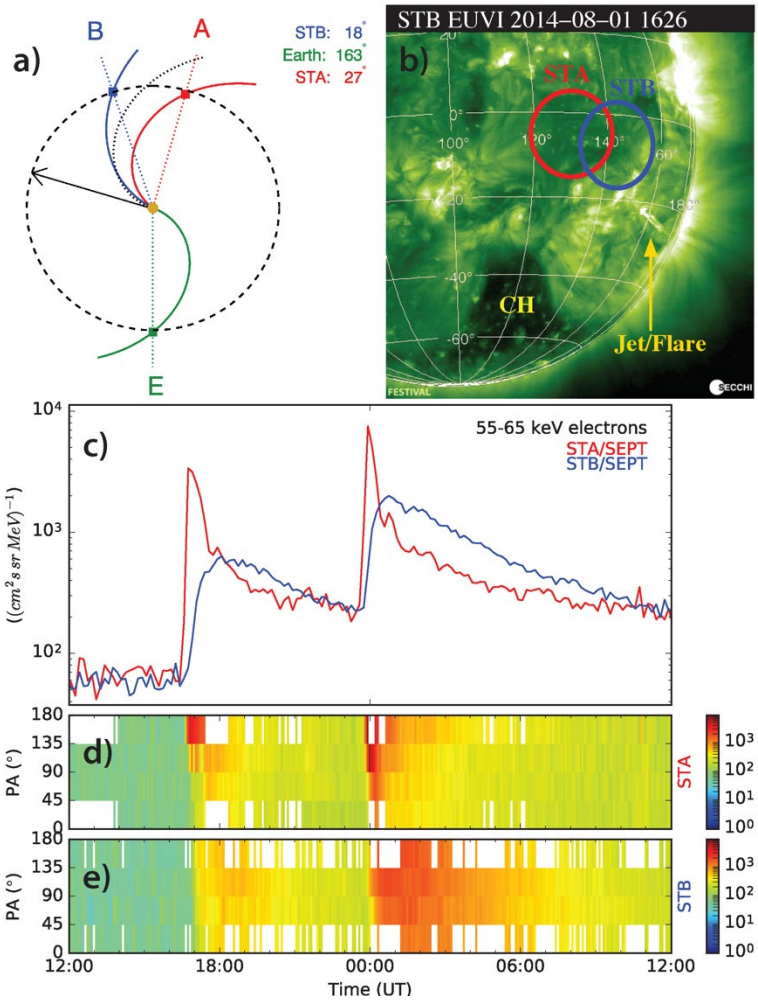

Exhibit 1-7. *(a) The location of the STEREO spacecraft during a flare event and (b) the approximate footpoint of both spacecraft relative to the flare site. (c–e) Energetic electron observations at both spacecraft showing clear differences at 1 au over 10's degrees of longitude. Adapted from* Klassen et al. *(2016).* Transport of energetic electrons from flare sites to 1 au is complex and requires multipoint measurements at mesoscale separations to constrain.

1.2.3 Significance, Impact, and Timeliness

Despite aligning with the key science goals (SG) of the previous National Academy of Science's Solar and Space Physics Decadal Report (*NAS*, 2012), the science goals of InterMeso have remained elusive, highlighting the need for a new mission architecture to solve these still open questions. Specifically, InterMeso goals are directly related to SG4 "Discover and characterize fundamental processes that occur both within the heliosphere and throughout the universe," SG3 "Determine the interaction of the Sun with the solar system…," and SG1 "Determine the origins of the Sun's activity and predict the variations in the space environment." Additionally, InterMeso directly addresses the Heliophysics decadal Solar and Heliospheric Physics science challenge 3 "Determine how magnetic energy is stored and explosively released and how the resultant disturbances propagate through the heliosphere." InterMeso goals are also relevant to the Heliophysics NASA Roadmap focus areas F2, H1, W1, W2, and W3 (*NASA*, 2014).

Fundamentally understanding the mesoscale (hundreds of R_E to a few degrees heliographic longitude at 1 au, i.e., in-between the inertial and injection ranges) structure of the solar wind and transients and its subsequent effects on particle acceleration and transport will be paradigm shifting in our insight into the heliosphere, as mesoscale dynamics are vital for resolving long-standing questions of the community. *As such, a new mission with an enabling, multipoint architecture is essential to address these objectives.* InterMeso will fill a critical observational gap in the current Heliophysics System Observatory (HSO) as mesoscale solar wind structure and

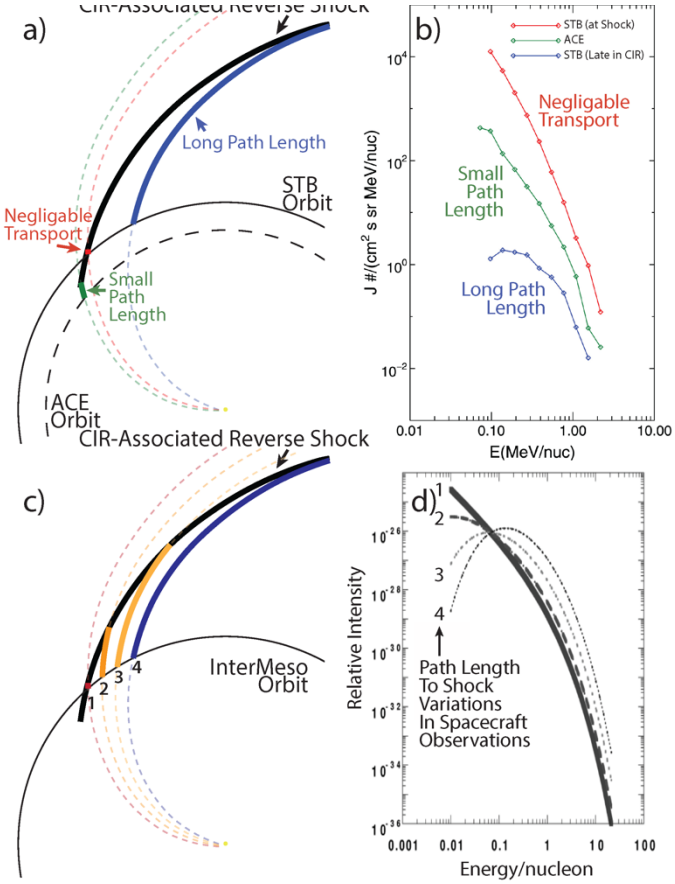

Exhibit 1-8. *(a) Cartoon of the observation locations relative to a CIR-associated reverse shock inferred from (b) energetic particle spectra (adapted from* Zhao et al.*, 2016). (c)* Distributed observations at mesoscale separations are needed to (d) constrain the transport effect on particle spectra without ambiguities from temporal evolution *(adapted from* Mason et al.*, 1999).*

dynamics falls between the global scales studied by the in situ instrumentation on STEREO (*Kaiser et al.*, 2008) and occasional opportune conjunctions within the HSO, and the kinetic scales unlocked by MMS (*Burch et al.*, 2016), Cluster (*Escoubet et al.*, 2001), and the HelioSwarm mission (illustrated in **Exhibit 1-9**).

The goal of InterMeso, to resolve the critical physics and consequences of the mesoscale solar wind and transients, is also particularly timely for the next decade. With the continued operation of ground-based solar observatories (e.g., Daniel K. Inouye Solar Telescope [DKIST]; *Tritschler et al.*, 2016) and solar/heliographic imaging satellite missions, InterMeso measurements will have complementary remote sensing observations of the solar footpoints of the spacecraft. The upcoming discoveries from the Polarimeter to Unify the Corona and Heliosphere (PUNCH; https://punch.space.swri.edu/) mission will enable a better understanding of the initial mesoscale structuring of the coronal young solar wind, and so will feed directly into the interpretations of mesoscale variability at 1 au from InterMeso, furthering our insight into the evolution of this mesoscale variability between the solar source and Earth at 1 au. Understanding of the transition from the inertial to dissipation range of plasma turbulence from HelioSwarm, coupled with understanding of the injection-to-inertial range

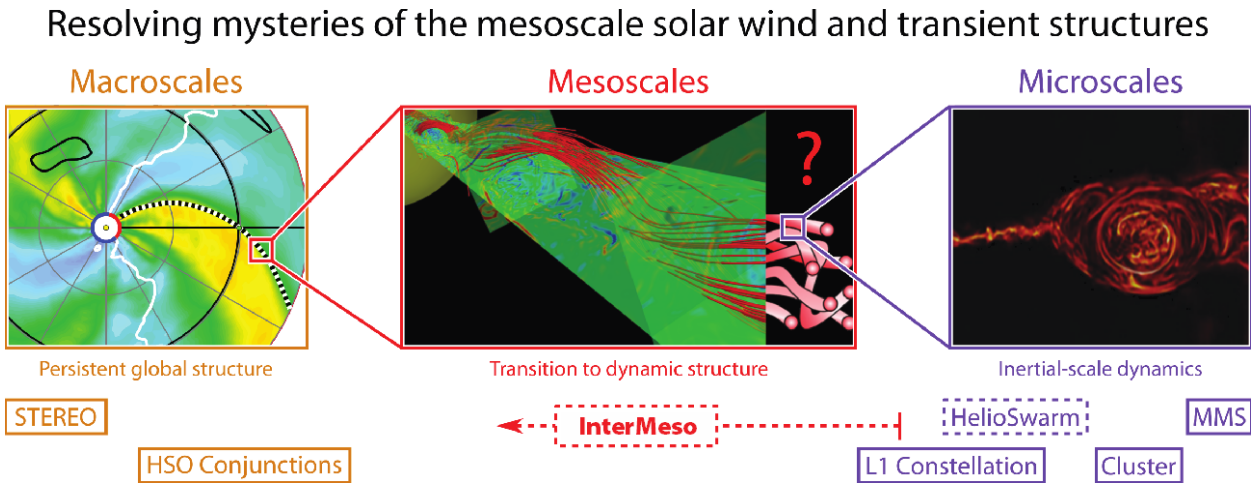

Exhibit 1-9. *Mesoscale dynamics are fundamental to solar wind dynamics, enabling interaction between macro- and micro-scale dynamics, but currently fall within an observational gap. Left panel from* Allen et al. *(2020), middle panel adapted from* Maruca et al. *(2021), and right panel from* Lazarian et al. *(2020).* InterMeso targets fundamental knowledge gaps of solar wind dynamics and structure at these critical scale lengths.

from InterMeso, would for the first time provide a broad picture of plasma variability in the mesoscale solar wind. Additionally, the European Space Agency (ESA) Vigil mission to L5 (https://www.esa.int/Space_Safety/Vigil), in partnership with the National Oceanic and Atmospheric Administration (NOAA), is planned to launch in 2027 and will include a heliospheric imager that can provide broader context for the in situ observations of the InterMeso mission. The potential synergies between InterMeso and upcoming missions (e.g., HelioSwarm, PUNCH, and Vigil) motivate such an architecture within the next decade.

1.3 Mission Concept Science Traceability

The overarching science goals of InterMeso flow into eight targeted science questions, shown in the Science Traceability Matrix (STM) provided in **Exhibit 1-12**. Addressing these questions requires simultaneous, multipoint observations with inter-spacecraft separations ranging from ~0.5 Mkm to tens of Mkm (i.e., hundreds of R_E to a few degrees in heliographic longitude at 1 au). Maintaining the constellation at a near-1 au heliocentric distance enables observations of both well-formed and still-steepening shocks of CMEs and SIR/CIRs.

All InterMeso spacecraft require measurements of the low-energy, bulk solar wind plasma. This includes sub-minute cadence observations of the bulk proton population for speeds ranging from 250 to 1000 km/s and densities from 1 to 100 cm^{-3}. This range of measurements with necessary accuracy can be accomplished with modern Faraday cup instrumentation (e.g., *Case et al.*, 2020). Thermal ion (1 keV/e to tens of keV/e) composition measurements on a less than few minute cadence will be critical to disambiguate changes in flux tube composition (see **Exhibit 1-10**). This will require the ability to distinguish between various species and charge states including H, He^{2+}, C^{5-6+}, N^{5-6+}, O^{6-7+}, and Fe^{6-12+} and can be satisfied by modern iterations of the Ulysses and ACE Solar Wind Ion Composition Spectrometer (SWICS) instrument design (*Gloeckler et al.*, 1992). Low-energy electron observations spanning from a few eV to tens of keV, i.e., including the core, halo, and strahl populations, are also needed and be achieved with the inclusion of a Parker Solar Probe (PSP) Solar Probe Analyzers-Electrons (SPAN-E)-type instrument (*Kasper et al.*, 2016).

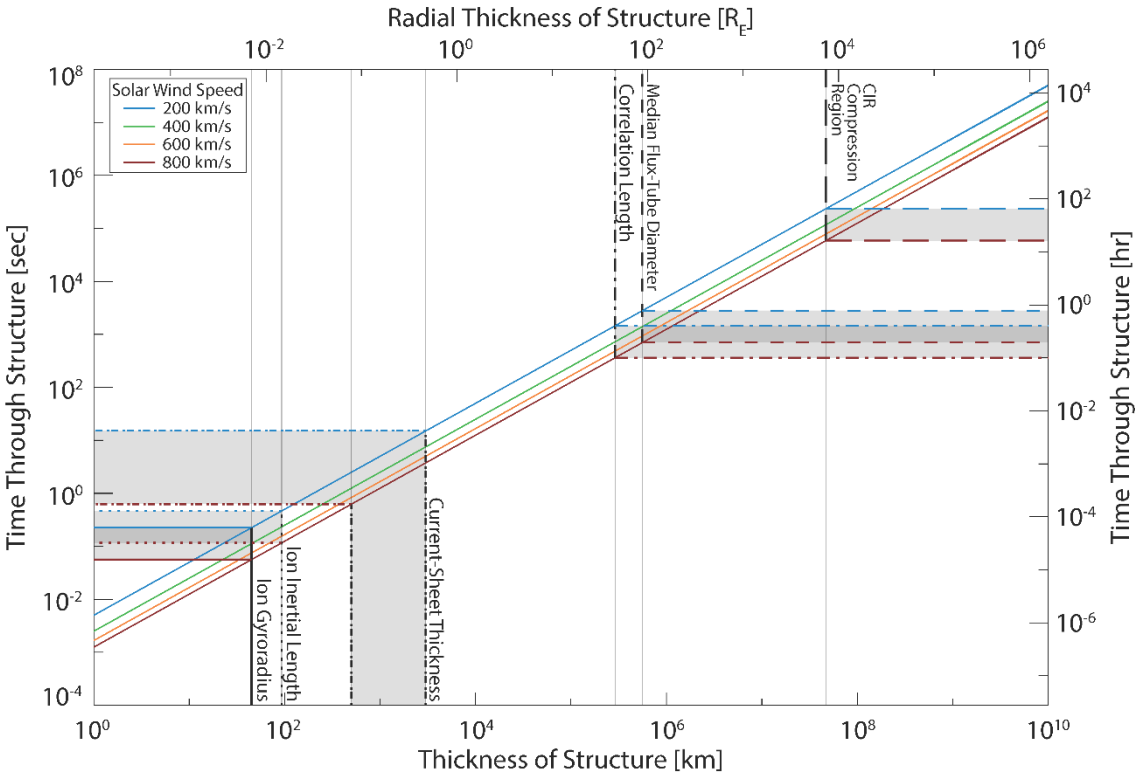

Exhibit 1-10. *The convective thickness of structures requires sub-minute resolution to explore the mesoscale variability of the solar wind.*

Additionally, suprathermal and energetic ion/electron measurements are required to explore anisotropies and, importantly, differentiate various ion species for investigating mass-per-charge-dependent processes of particle acceleration and transport. Suprathermal ion (5–100 keV/nuc) and energetic ion (0.1–10 MeV/nuc) measurements with mass determination (i.e., H, ^{3}He, ^{4}He, C, N, O, Fe) are required on a cadence of several minutes and tens of minutes, respectively, which is within the capabilities of current generation versions of the Solar Orbiter Suprathermal Ion Spectrograph (SIS; *Rodríguez-Pacheco et al.*, 2020; *Wimmer-Schweingruber et al.*, 2021) instrument. Energetic electron observations (a few tens of keV to a few MeV) are needed with capabilities of determining first-order anisotropy on a few second cadence to characterize mesoscale variations in SEP events, which can be achieved with Solar Orbiter Energetic Particle Telescope (EPT)-like instrumentation (*Rodríguez-Pacheco et al.*, 2020; *Wimmer-Schweingruber et al.*, 2021).

To probe mesoscale magnetic structuring and impacts of plasma waves and turbulence on particle transport, observations of the magnetic field and radio emissions released from flare events and shock acceleration are required. Vector magnetic field measurements must have a full-scale range of at least ±100 nT with 0.1 nT or better resolution at cadences of 16–64 vectors/s, obtainable by current fluxgate instrumentation (e.g., PSP/FIELDS; *Bale et al.*, 2016). Radio wave observations ranging from 10^{-18} to 10^{-12} $V^2/m^2/Hz$ over the frequency range of 0.1 kHz to 20 MHz, achievable with STEREO SWAVES (*Bougeret et al.*, 2008) or Solar Orbiter Radio Plasma Waves (RPW; *Maksimovic et al.*, 2020)-type instrumentation, are also needed. Accurate timing and characterization of electron acceleration near the solar surface necessitates observations of hard X-rays with an indirect imager (e.g., *Krucker et al.*, 2020) along with radio wave observations to determine both the source location and electron characteristics. The X-ray instrument must measure hard X-ray spectra, images, and time series with an energy range between 5 and 100 keV, and is achievable with Solar Orbiter Spectrometer Telescope for Imaging X-rays (STIX)-type instrumentation (*Krucker et al.*, 2020).

As such, the baseline payload for this mission requires each spacecraft of the constellation to be outfitted with: ***(1)*** bulk solar wind instrument, ***(2)*** thermal ion composition instrument, ***(3)*** suprathermal ion composition telescope, ***(4)*** energetic ion composition telescope, ***(5)*** low-energy electron instrumentation, ***(6)*** energetic electron telescopes, ***(7)*** DC vector magnetic field sensor, and ***(8)*** high-frequency electric field radio wave instrumentation. Additionally, only one of the spacecraft must be equipped with ***(9)*** a hard X-ray indirect imager due to the relatively close separation needed for the InterMeso spacecraft to span the mesoscale regime. Notional candidate instruments have been identified (**Section 3.1** and **Appendix C**) and are used in this report to baseline costing and accommodations. *No enabling technologies are required for this mission architecture, as all instruments and subsystems are at a minimum of Technology Readiness Level (TRL) 6.* All of the identified

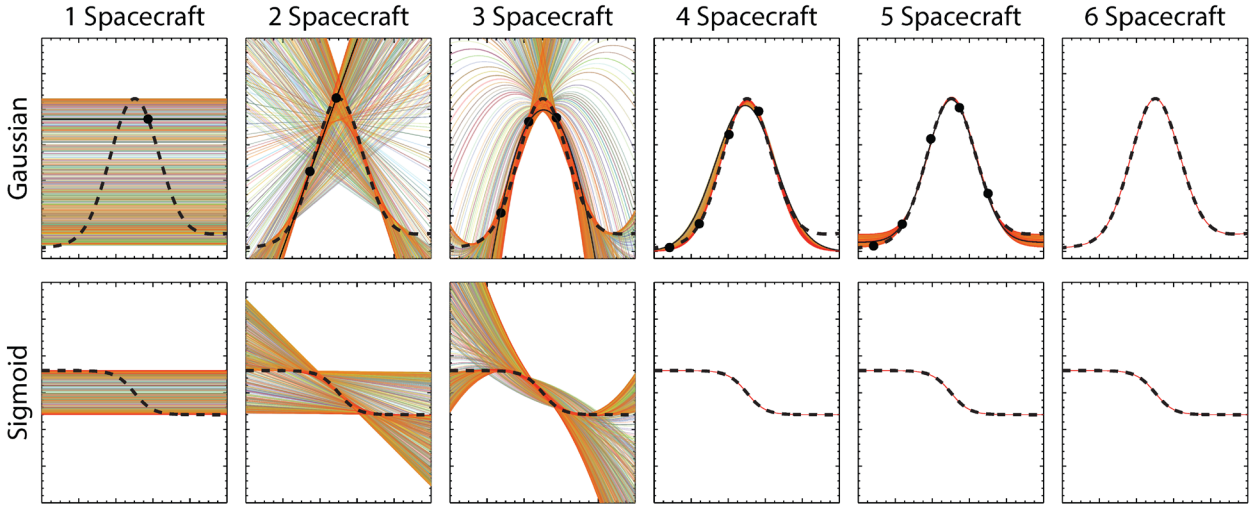

Exhibit 1-11. *Randomized placement of a four-spacecraft constellation throughout both a Gaussian (top row) and Sigmoidal (bottom row) distribution allows for different functional fits. Filled-in circles in the top row are examples of the 1000 random placements of spacecraft constellations resulting in the shown colored fits. The solid black curve on the top row is the corresponding fit from the shown example placements. The initial distribution the fits are attempting to recreate is shown by the dashed curve.* Four spacecraft are the optimal benefit-to-cost configuration for mesoscale variations.

notional payload instruments are able to reach, if not exceed, the measurement requirements for this mission (as discussed in **Appendix C**).

Closure of the science objectives given in **Exhibit 1-12** requires simultaneous multipoint observations with longitudinal separations that span the range of mesoscale dynamics in the solar wind at 1 au. **Exhibit 1-11** illustrates the ability to reconstruct longitudinal variations following either a Gaussian (top) or sigmoidal (bottom) distribution by taking a representative distribution (dashed line) and placing 1000 randomly placed constellations of equally spaced observing points within the domain. For the Gaussian reconstructions, a single spacecraft can only result in a single value, two spacecraft can provide a linear variation, three spacecraft provide a quadratic, while four and more spacecraft can constrain different orders of Gaussian fits. Similarly, the sigmoidal distribution can be represented by a single value, linear fit, quadratic fit, or sigmoidal fit. As demonstrated in **Exhibit 1-11**, increasing the number of spacecraft increases the ability to discern characteristic longitudinal profiles relevant to structures in the solar wind, particularly Gaussian-type distributions (i.e., the spread of energetic particles from an acceleration region) and sigmoidal-type variations (i.e., current sheets or changes in topology across flux tubes). Distinguishing more complex topological variabilities, such as "ripples" in a large-scale shock structure (e.g., *Bale et al.*, 1999), or better constraining the non-planarity and radius of curvature of interplanetary shocks (e.g., *Neugebauer & Giacalone*, 2005), also benefit from increasing numbers of longitudinally separated observations.

While additional spacecraft can increase the science return of InterMeso, four points of measurement within relevant scales provide the highest benefit-to-cost for expected variability of mesoscale phenomena with features manifesting as either a Gaussian or sigmoidal distribution (shown in **Exhibit 1-11**). With fewer than four spacecraft, the ability to reconstruct the distribution becomes significantly deteriorated. However, while a constellation with more than four spacecraft can serve to hone the resulting reconstructions of longitudinal variation in mesoscale phenomena, the added value, particularly when including available mission resources and cost, diminishes with additional spacecraft. As such, the InterMeso mission architecture targets four spacecraft as a baseline to determine spatiotemporal variations and elucidate mesoscale structure.

Exhibit 1-12. *InterMeso Science Traceability Matrix.*

Overarching Goal	InterMeso Objectives	Targeted Science Questions	Science Requirement	Measurement Requirements: Bulk Solar Wind	Thermal Ion Composition	Suprathermal Ion Composition	Energetic Ion Composition	Low-Energy Electrons	Energetic Electrons	Magnetic Field	Radio Waves	Hard X-ray	Inter-S/C Separations	Supporting Observations & Models
Investigating the fundamental mesoscale nature of the variable solar wind and impacts on particle acceleration, evolution, and transport.	**1.** Characterize and identify the origin of the mesoscale variability of the background solar wind and transient solar wind structures	**1.1** What do the predominant scale sizes of the mesoscale solar wind and IMF reveal about the origins of these structures?	Conduct correlation analysis between spacecraft to determine the relevant scale sizes of the solar wind and fluxtubes. Need the ability to discern when changing between flux tubes: proton entropy, ion composition (tied to source), strahl electron properties. Compare these scale sizes to expected solar variability (i.e., from granule/supergranule) vs. variability caused by dynamics in the inner heliosphere.	Density: 1–100 cc Speed: 250–1000 km ΔE/E = 20% Speed accuracy <10% Density accuracy <10% Temp accuracy <30% Sub minute	Energy: 1–10's keV/e ΔE/E = 20% Angular resolution <10° Species: H, He^{1-2+}, C^{4-6+}, N^{5-6+}, O^{5-7+}, Fe^{6-12+} < few minutes	No	No	Energy: few eV – tens keV ΔE/E = 20% Angular resolution: 20% Full VDF Few seconds	No	Full-scale range: ±100 nT Noise: <0.05 nT/sqrt(Hz) Resolution: 0.1 nT Sample rate: 16 vectors/s	Full-scale Range: 0.1–0.5 mV/m Sensitivity: 10e-18 – 10e-12 $V^2/m^2/Hz$ Frequency Range: 0.1 – 200 kHz Spectrum Cadence: 0.25 s	No	~5.5e5 km (flux tube cross-section) ~2e6 – ~6.5e6 km (granule/supergranule expansion at 1 au)	Solar Magnetogram DKIST (and other remote solar observatories) Simulation advancements to resolve mesoscales Connectivity Tools
		1.2 How do large-scale, persistent structures transition into dynamic turbulence?	Measure the azimuthal turbulence both within and across flux tubes encompassing the inertial and injection range. Distinguish periods dominated by Alfvénic and slow-mode-like fluctuations. Determine potential differences in azimuthal turbulence in longitudinally separated parcels of plasma with composition measurements to identify different solar sources.	Density: 1–100 cc Speed: 250–1000 km ΔE/E = 20% Speed accuracy <10% Density accuracy <10% Temp accuracy <30% Sub minute	Energy: 1–10's keV/e ΔE/E = 20% Angular resolution <10° Species: H, He^{1-2+}, C^{4-6+}, N^{5-6+}, O^{5-7+}, Fe^{6-12+} < few minutes	No	No	Energy: few eV – tens keV ΔE/E = 20% Angular resolution: 20% Full VDF Few seconds	No	Full-scale range: ±100 nT Noise: <0.05 nT/sqrt(Hz) Resolution: 0.1 nT Sample rate: 64 vectors/s	Full-scale Range: 0.1–0.5 mV/m Sensitivity: 10e-18 – 10e-12 $V^2/m^2/Hz$ Frequency Range: 0.1–200 kHz Spectrum Cadence: 0.25 s	No	~4e5 km during commissioning 1e6 km to 1e9 km	PUNCH as input Inputs from L1 and L5 Global MHD & Flux rope Simulations
		1.3 How do mesoscale variabilities of the solar source manifest variations in seed particle properties and composition at 1 au?	Determine the thermal/suprathermal ion spectra for main species (H, He, C, O, Fe) at high time cadence under both quiescent solar wind and across boundaries. Use locally accelerated particles in ESP events or at CIRs to understand the role of seed particles in suprathermal-to-energetic ion composition. Constrain mesoscale variations in these populations compared to solar wind structures (1.1). Determine if the mesoscale structuring of background solar wind maps to variability in seed particle populations. Determine if this points to variability of seed particle production in different solar structures (i.e., granules), or if this is from a broader reservoir.	Density: 1–100 cc Speed: 250–1000 km ΔE/E = 20% Speed accuracy <10% Density accuracy <10% Temp accuracy <30% Sub minute	Energy: 1–10's keV/e ΔE/E = 20% Angular resolution <10° Species: H, He^{1-2+}, C^{4-6+}, N^{5-6+}, O^{5-7+}, Fe^{6-12+} < few minutes	Energy: 5-100 keV/nuc ΔE/E = 10% Species: H, ^3He, ^4He, C, N, O, Fe M/ΔM > 50 Few minutes	Energy: 0.1–10 MeV/nuc ΔE/E = 30% Mass: H, ^3He, ^4He, C, N, O, Fe tens of minutes	Energy: few eV – tens keV ΔE/E = 20% Angular resolution: 20% Full VDF Few seconds	No	Full-scale range: ±100 nT Noise: <0.05 nT/sqrt(Hz) Resolution: 0.1 nT Sample rate: 8 vectors/s	No	No	~5.5e5 km (flux tube cross-section) ~2e6 – ~6.5e6 km (granule/supergranule expansion at 1 au)	Solar imaging Solar magnetograms CIR modeling (data assimilation into MHD)
		1.4 How does the mesoscale solar wind imprint itself on solar wind transients and interplanetary shock structures?	Determine morphological variability of transient structures (such as IP shocks, CMEs) expanding into the mesoscale solar wind. Determine if the variability across transient structures and shocks match that of the background solar wind (1.1) or if there are higher order perturbations or constraints. Need ability to discern connection to source (shock or the Sun) through strahl/energetic electrons.	Density: 1–100 cc Speed: 250–1000 km ΔE/E = 20% Speed accuracy <10% Density accuracy <10% Temp accuracy <30% Sub minute	Energy: 1–10's keV/e ΔE/E = 20% Angular resolution <10° Species: H, He^{1-2+}, C^{4-6+}, N^{5-6+}, O^{5-7+}, Fe^{6-12+} < few minutes	No	No	Energy: few eV – tens keV ΔE/E = 20% Angular resolution: 20% Full VDF Few seconds	Energy: few tens keV to few MeV 1st order anisotropy few seconds	Full-scale range: ±100 nT Noise: <0.05 nT/sqrt(Hz) Resolution: 0.1 nT Sample rate: 64 vectors/s	Full-scale Range: 0.1–0.5 mV/m Sensitivity: 10e-18 – 10e-12 $V^2/m^2/Hz$ Frequency Range: 0.1–200 kHz Spectrum Cadence: 0.25 s	Products: HXR spectra, images, & time series Energy: ~5–100 keV Energy Resolution: ~1 keV below 10 keV and ~0.1*E above 10 keV Angular resolution: ~10 arcsec Few seconds	~5.5e5 km (flux tube cross-section) ~2e6 – ~6.5e6 km (granule/supergranule expansion at 1 au)	L5-based & STEREO heliographic imager Ground-based radio arrays Simulation advancements to resolve mesoscales
	2. Characterize and understand the impact of these mesoscale variations on particle acceleration and transport	**2.1** How does mesoscale solar wind variability and intermittency impact variability in particle acceleration?	Compare mesoscale variations in the suprathermal and energetic particle range to possible variations in wave instability occurrence predictions such as lower-hybrid waves, magnetosonic waves, ion-acoustic waves, electron cyclotron drift instability, and Langmuir waves. Compare mesoscale variations in suprathermal and energetic particles to evidence of solar wind intermittency.	Density: 1–100 cc Speed: 250–1000 km ΔE/E = 20% Speed accuracy <10% Density accuracy <10% Temp accuracy <30% Sub minute	Energy: 1–10's keV/e ΔE/E = 20% Angular resolution <10° Species: H, He^{1-2+}, C^{4-6+}, N^{5-6+}, O^{5-7+}, Fe^{6-12+} < few minutes	Energy: 5-100 keV/nuc ΔE/E = 10% Mass: H, ^3He, ^4He, C, N, O, Fe M/ΔM > 50 Few minutes	Energy: 0.1–10 MeV/nuc ΔE/E = 30% Mass: H, ^3He, ^4He, C, N, O, Fe tens of minutes	Energy: few eV – tens keV ΔE/E = 20% Angular resolution: 20% Full VDF Few seconds	No	Full-scale range: ±100 nT Noise: <0.05 nT/sqrt(Hz) Resolution: 0.1 nT Sample rate: 64 vectors/s	Full-scale Range: 0.1–0.5 mV/m Sensitivity: 10e-18 – 10e-12 $V^2/m^2/Hz$ Frequency Range: 0.1–200 kHz Spectrum Cadence: 0.25 s	No	~5.5e5 km (flux tube cross-section) ~2e6 – ~6.5e6 km (granule/supergranule expansion at 1 au)	Simulation advancements to resolve mesoscales
		2.2 How does mesoscale structuring of solar wind transients and interplanetary shocks affect particle acceleration?	Determine mesoscale variations in longitudinally spread signatures of shock drift acceleration, diffusive shock acceleration, and fast Fermi processes to constrain the extent that mesoscale structuring may modulate these processes. Need ability to discern plasma variations across shocks, and measure variations in A/Q for energetic ions.	Density: 1–100 cc Speed: 250–1000 km ΔE/E = 20% Speed accuracy <10% Density accuracy <10% Temp accuracy <30% Sub minute	Energy: 1–10's keV/e ΔE/E = 20% Angular resolution <10° Species: H, He^{1-2+}, C^{4-6+}, N^{5-6+}, O^{5-7+}, Fe^{6-12+} < few minutes	Energy: 5-100 keV/nuc ΔE/E = 10% Mass: H, ^3He, ^4He, C, N, O, Fe M/ΔM > 50 Few minutes	Energy: 0.1–10 MeV/nuc ΔE/E = 30% Mass: H, ^3He, ^4He, C, N, O, Fe tens of minutes	Energy: few eV – tens keV ΔE/E = 20% Angular resolution: 20% Full VDF Few seconds	Energy: few tens keV to few MeV 1st order anisotropy few seconds	Full-scale range: ±100 nT Noise: <0.05 nT/sqrt(Hz) Resolution: 0.1 nT Sample rate: 64 vectors/s	Full-scale Range: 0.1–0.5 mV/m Sensitivity: 10e-18 – 10e-12 $V^2/m^2/Hz$ Frequency Range: 0.1–200 kHz Spectrum Cadence: 0.25 s	No	~3e5 – 1e7 km (nominal IP shock radius of curvature) 1's deg. (CIR interfaces, connection to reverse shocks)	L5-based & STEREO heliographic imager Ground-based radio arrays Simulation advancements to resolve mesoscales
		2.3 How do mesoscale variations of the background solar wind impact the connectivity of an observer to the solar source or acceleration site?	Ability to examine the timing of hard X-rays and the timing of in situ electrons to determine transit time from most probable flare location and time. Determine mesoscale variations in the injection timing and path length of energetic particles from source to observer and compare this to changes in particle population properties. Determine mesoscale variability in ion drop out events.	Density: 1–100 cc Speed: 250–1000 km ΔE/E = 20% Speed accuracy <10% Density accuracy <10% Temp accuracy <30% Sub minute	Energy: 1–10's keV/e ΔE/E = 20% Angular resolution <10° Species: H, He^{1-2+}, C^{4-6+}, N^{5-6+}, O^{5-7+}, Fe^{6-12+} < few minutes	Energy: 5-100 keV/nuc ΔE/E = 10% Mass: H, ^3He, ^4He, C, N, O, Fe M/ΔM > 50 Few minutes	Energy: 0.1–10 MeV/nuc ΔE/E = 30% Mass: H, ^3He, ^4He, C, N, O, Fe tens of minutes	Energy: few eV – tens keV ΔE/E = 20% Angular resolution: 20% Full VDF Few seconds	Energy: few tens keV to few MeV 1st order anisotropy few seconds	Full-scale range: ±100 nT Noise: <0.05 nT/sqrt(Hz) Resolution: 0.1 nT Sample rate: 8 vectors/s	Full-scale Range: 0.1–0.5 mV/m Sensitivity: 10e-18 – 10e-12 $V^2/m^2/Hz$ Frequency Range: 0.1–20 MHz Spectrum Cadence: 0.25 s	Products: HXR spectra, images, & time series Energy: ~5–100 keV Energy Resolution: ~1 keV below 10 keV and ~0.1*E above 10 keV Angular resolution: ~10 arcsec Few seconds	1's deg. (CIR interfaces, connection to reverse shocks)	Solar Magnetogram Solar remote sensing observations Connectivity Tools Transport models
		2.4 How do mesoscale dynamics such as field line meandering and stochastic motion affect diffusion of particles in the solar wind?	Ability to detect energetic electrons with refined time resolution at multiple spacecraft separated in longitude. Determine mesoscale variability in ion drop out events.	Density: 1–100 cc Speed: 250–1000 km ΔE/E = 20% Speed accuracy <10% Density accuracy <10% Temp accuracy <30% Sub minute	Energy: 1–10's keV/e ΔE/E = 20% Angular resolution <10° Species: H, He^{1-2+}, C^{4-6+}, N^{5-6+}, O^{5-7+}, Fe^{6-12+} < few minutes	Energy: 5-100 keV/nuc ΔE/E = 10% Mass: H, ^3He, ^4He, C, N, O, Fe M/ΔM > 50 Few minutes	Energy: 0.1–10 MeV/nuc ΔE/E = 30% Mass: H, ^3He, ^4He, C, N, O, Fe tens of minutes	Energy: few eV – tens keV ΔE/E = 20% Angular resolution: 20% Full VDF Few seconds	Energy: few tens keV to few MeV 1st order anisotropy few seconds	Full-scale range: ±100 nT Noise: <0.05 nT/sqrt(Hz) Resolution: 0.1 nT Sample rate: 8 vectors/s	Full-scale Range: 0.1–0.5 mV/m Sensitivity: 10e-18 – 10e-12 $V^2/m^2/Hz$ Frequency Range: 0.1–20 MHz Spectrum Cadence: 0.25 s	Products: HXR spectra, images, & time series Energy: ~5–100 keV Energy Resolution: ~1 keV below 10 keV and ~0.1*E above 10 keV Angular resolution: ~10 arcsec Few seconds	1's deg. (full span ~10°)	Stochastic motion models with particle transport

2. Mission Concept Investigation

2.1 Overview

To address the science objectives and measurement requirements **Section 1**, detailed trades of mission architecture, concept of operations (CONOPS), I&T, and notional instrumentation have been explored. This section outlines the end result of this investigation, with additional details provided in appendices. Key to the science of InterMeso, the mission requires multiple, longitudinally separated spacecraft in the solar wind near 1 au with varying inter-spacecraft separations over the course of the mission. As such, the end concept consists of four, near-identical spacecraft placed in an Earth-trailing orbit with unique drift rates allowing them to slowly separate over the life of the mission. *This baseline architecture demonstrates, with conservative margin, that this concept is not only actionable without additional technology development but at a reasonable cost.*

2.2 Concept Maturity Level

The InterMeso mission concept has been developed to CML-4 as a preferred point design. The proposed flight system design includes subsystem and box-level details with margins assigned according the Johns Hopkins Applied Physics Laboratory (APL) Quality Management System (QMS) standards. Details of margin definitions can be found in **Appendix A**. Cost, schedule and risk assessments were conducted and shown to fall within acceptable ranges of NASA Heliophysics Mission Concept Study guidelines. Key trades that went into point design formation are outlined in **Section 2.4**.

2.3 Technology Maturity

All technologies selected for InterMeso are either TRL 6+ or are on a development path to be there prior to the Solar and Space Physics (Heliophysics) decadal survey release. Four instruments at TRL 6 (or on schedule to be there by September 2022) are the lowest TRL items included in the mission. These instruments are SPICES, SIS-Lo, SIS-Hi, and MEPS. SPICES is the only instrument not currently at TRL 6 due to its high-voltage power

Area	Trade Space, Result Bold	Rationale
Risk Classification	**Risk Classification C** Risk Classification B	• Risk Class C posture is in line with Van Allen Probes (VAP), MMS, and STEREO • Substantial cost savings, Class B would require nearly double the flight units per spacecraft or the addition of a fifth spacecraft • Selective Redundancy added to bolster design reliability in cost effective manner • Functional redundancy is also achievable in some subsystems without substantial effects to cost
Spacecraft Procurement	**Make Custom Spacecraft Bus** Buy COTS spacecraft Bus	• Not feasible to accommodate all instrument field-of-views with COTS buses • Unique magnetic cleanliness, surface charging and power-switching frequency standardization requirements are not compatible with COTS spacecraft buses
Multi-spacecraft Launch Configuration	**ESPA Grande with C22** Four-Spacecraft Stacked Configuration Flat Plate Adapter	• Identical Payload Adapter (PLA) interfaces across all spacecraft eliminate complexities associated with stacked launch configurations including the need for unique signal passthroughs or extra structure on base spacecraft • Well-defined, industry-standard PLA interface enables single-spacecraft environmental testing (if needed) and minimizes the interface tailoring associated with other options
Heliocentric Orbit Insertion	**Direct Injection** Lunar-Phasing Orbits (STEREO solution)	• Lowers overall spacecraft delta-V budget • Simplifies operations (only one deterministic maneuver, no Earth orbit phase) • Single traverse of Van Allen belts • STEREO required complex, multi-burn lunar-phasing orbits to target different earth-relative drift directions, InterMeso spacecraft all travel in the same earth-relative drift direction
Science Downlink Frequency	**Ka-Band Science Downlink** X-band Science Downlink	• Maximizes data return within the high-gain antenna (HGA) size constraints imposed by the launch configuration (four spacecraft in a single launch vehicle) • Alleviates need for increased Deep Space Network (DSN) time later in the mission and through most of the extended mission • Consistent with study guidelines
Attitude Control	**Reaction Wheels** Thruster-only Control	• Better pointing accuracy satisfies both instrument pointing and Ka-band downlink requirements, more analysis would be required to prove thruster-only control is adequate • Saves consumables and increases potential extended mission length

Exhibit 2-1. *Key trades table.*

supply (HVPS). NASA is currently funding development of the SPICES HVPS Engineering Model and associated testing at the University of Michigan under NASA contract, with delivery due in September 2022.

2.4 Key Trades

Multiple solutions were considered for each design decision with cost and risk impacts primary driving decisions. Key trade studies that drove the design are listed in **Exhibit 2-1**.

3. Technical Overview

3.1 Instrument Payload Description

Nine instruments comprise the InterMeso payload. All spacecraft are outfitted with eight of these instruments while only one spacecraft features a Hard X-ray indirect imager. All instrument types needed to fulfill the requirements of the STM (**Exhibit 1-12**) are all available from a variety of instrument providers. For this study, a slate of representative candidate instruments was selected and are further discussed in detail in **Appendix C**. All of these candidate instruments are at or above TRL 6, or will be prior to the Solar and Space Physics (Heliophysics) decadal survey release, *without any additional technology investment or development*. All assumed instruments have flight software equivalents that do not need significant code development. A summary of all instrument mass and power is provided in **Exhibit 3-1**. Throughout this study, spacecraft design assumes 15% allocated margin for instrument mass and 30% total margin for instrument power and data.

3.2 Flight System

The flight system consists of four near-identical single-string spacecraft operating independent of one another. All spacecraft launch together on a single launch vehicle directly into an Earth-trailing orbit. *This direct-injection method enables a simple flight system design that maintains a consistent Sun-relative attitude with no eclipses.* Flight system element mass and power are given in **Exhibit 3-2** with spacecraft block diagram in **Exhibit 3-3**.

3.2.1 Mechanical

Launch Vehicle and instrument accommodation are the primary drivers of the mechanical design. *To reduce cost and complexity in launch, the four InterMeso spacecraft can fit on a single Evolved Expendable Launch Vehicle (EELV) Secondary Payload Adapter (ESPA)-Grande equivalent and within a standard 5-m fairing* (shown in the stowed configuration in **Exhibit 3-4**). The STIX-like hard X-ray indirect imager accommodation is the only difference between the spacecraft with only one spacecraft requiring a STIX instrument, the other spacecraft include STIX mass/thermal simulators.

Instrument fields of view (FOVs) primarily fall into one of three categories: Parker Spiral/Anti-Parker Spiral facing, Sun-facing, or global, 4π-steradian coverage. The location of the Parker Spiral/Anti-Parker Spiral facing instruments, including SIS-Lo, SIS-Hi and MEPS, are the most highly constrained. Mounting these instruments

	Mass			Average Power		
	CBE (kg)	% Cont.	MEV (kg)	CBE (W)	% Cont.	MEV (W)
(1) Faraday Cup	5.90	15	6.79	5.00	15	5.75
(2) Thermal Ion Composition (SPICES)	13.14	15	15.11	24.17	15	27.80
(3) Suprathermal Ion Composition (SIS-Lo)	3.70	15	4.26	0.80	15	0.92
(4) Energetic Ion Composition (SIS-Hi)	2.40	15	2.76	0.40	15	0.46
(5) Lower-Energy Electron Distribution (SPAN-E)	4.80	15	5.52	4.40	15	5.06
(6) Energetic Electron Distribution (MEPS)	4.80	15	5.52	10.00	15	11.50
(7) Fluxgate Magnetometers, Boom, Electronics Box	13.86	15	1.71	4.97	15	5.72
(8) Electric Field (AC Only)	7.53	15	8.66	10.54	15	12.12
(9) Indirect Hard X-Ray Telescope (STIX, only on one spacecraft)	7.00	15	8.05	8.00	15	9.20
Total Payload Mass	**69.40**	**15**	**79.81**	**68.28**	**15**	**78.52**

Exhibit 3-1. *Payload mass and power table.*

	Mass			Average Power (Science Downlink Mode)		
	CBE (kg)	% Cont.	MEV (kg)	CBE (W)	% Cont.	MEV (W)
Instruments	69.40	15	79.81	68.28	15	78.52
Structures & Mechanisms	71.10	15	81.77	-	-	-
Thermal Control	18.00	9	19.53	16.91	15	17.41
Propulsion (Dry Mass)	20.34	1	20.54	4.62	1	4.67
Attitude Control	32.23	5	33.84	84.70	5	88.94
Command & Data Handling	8.42	8	9.13	26.07	10	28.55
Telecommunications	25.12	7	26.81	90.10	6	95.11
Power	61.82	12	69.04	33.50	10	36.83
Single-Spacecraft Dry Mass/Total Power	338.43	11	377.28	333.9	8	361.74
Total Flight Element Dry Mass	**1353.72**	**11**	**1509.11**	**-**	**-**	**-**

Exhibit 3-2. *Flight system element mass and power table.*

on the spacecraft decks parallel to the ecliptic plane satisfies all FOV requirements. Sun-facing instruments, including the Faraday cup, STIX and SPICES, are all mounted on the Sun-facing deck. The two SPAN-E units are mounted on opposite decks enabling 4π-steradian coverage. Magnetometers are accommodated on a 4.5-m-long boom extending in the anti-sunward direction with one magnetometer mounted halfway down the boom and the other at the tip. Electric field antennas are mounted on the anti-sunward deck, equally spaced 120° around the Sun–spacecraft line.

The primary structure, constructed from aluminum honeycomb panels, consists of a box, measuring 2 × 1.1 × 1.0 m, with an internal ring and spoke design. The internal structure is designed to accommodate the unique load path created with the ESPA Grande (or equivalent) payload adapter during launch. Both the internal spoke panels and box structure are used to mount spacecraft and instrument components internally. The internal cylinder

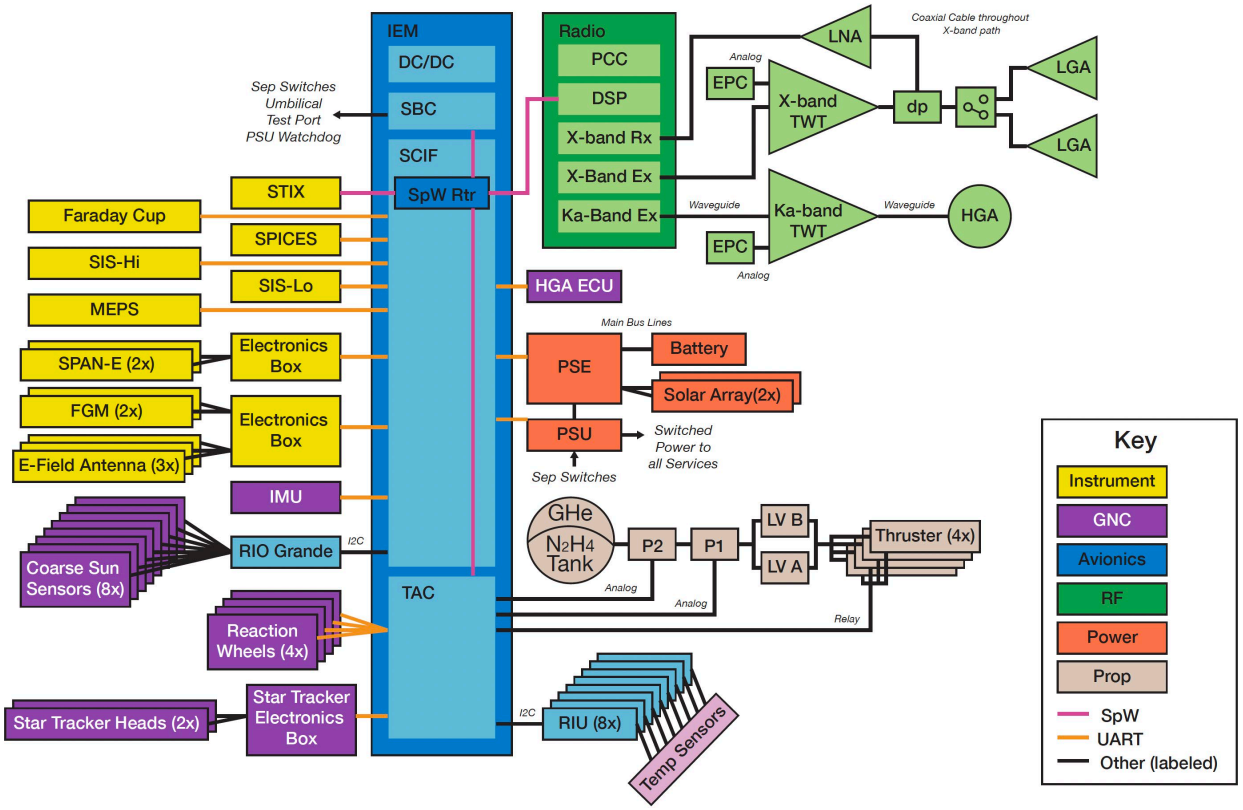

Exhibit 3-3. *InterMeso spacecraft block diagram.*

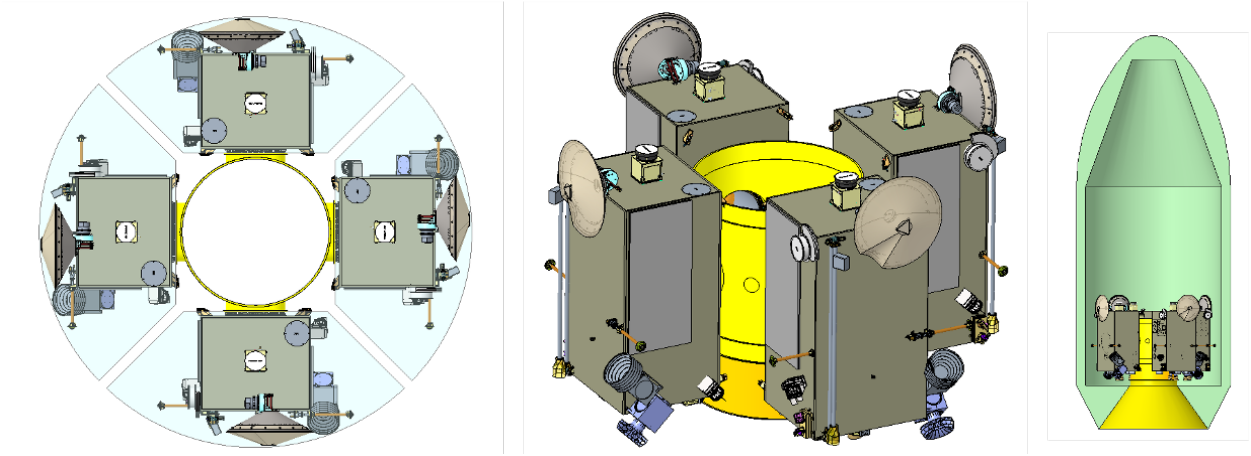

Exhibit 3-4. *Visualization of the four InterMeso spacecraft integrated onto an ESPA-Grande equivalent launch configuration, allowing for single manifest within a 5-m fairing.*

houses the hydrazine tank and interfaces directly to the payload adapter. The HGA is the only articulated mechanism on each spacecraft. The articulation is required to allow simultaneous HGA downlink operations and science data collection. Only small, infrequent gimbal movements are required to keep the instruments properly pointed and the HGA on Earth. Deployable mechanisms include two solar arrays, three electric field antenna and a magnetometer boom. All deployments have redundant actuation services, minimizing risk.

3.2.2 Thermal

InterMeso's simple thermal design is enabled by its near constant solar distance (0.96 au to 1.05 au), lack of eclipses and consistent, Sun-relative spacecraft attitude. Each spacecraft is blanketed entirely in multilayer insulation (MLI) with the exception of the radiators and component/instrument penetrations. Five of the six spacecraft panels are consistently non-Sun-facing, offering flexibility in radiator placement. A majority of the spacecraft, including the propulsion system, is kept within temperature ranges via thermostats, heaters, and internal component heat dissipation coupled to the structure. The battery and the SPICES and STIX instruments require thermal isolation to stay within their temperature limits. K-core doublers or aluminum thermal ribs may be required to distribute heat in the final design.

3.2.3 Propulsion

A blowdown monopropellant hydrazine system provides delta-V and momentum dumping capability for the spacecraft. A maximum total delta-V requirement of 75 m/s is assumed for each spacecraft based on mission design analysis. This encompasses both the deterministic delta-V, presented in **Section 3-2**, and statistical delta-V. The system consists of four thrusters, a single tank, and components required to control the flow of propellant and monitor system health and performance (see **Exhibit 3-3**). Aerojet Rocketdyne AR-111G 4.4 N catalytic monopropellant hydrazine thrusters are assumed for this study with analysis performed using mission-averaged performance data. The propellant and helium pressurant, separated by a silicon-free elastomeric diaphragm, are stored in a single titanium tank manufactured by Northrop Grumman Innovation Systems. The remaining components used to monitor and control the flow of propellant will be selected from a large catalog of components with substantial flight heritage on APL and another spacecraft. Latch valves may require compensation magnets to meet magnetic cleanliness requirements. Momentum management requires roughly 0.4 kg of propellant a year for a maximum of 1.5 kg of propellant required during the primary mission. Tanks were intentionally over-sized to allow for flexibility in the extended mission planning. Fully filled, the tanks enable a system delta-V of 225 m/s, providing robust margin on the requirements. *The InterMeso propulsion system is fully capable of exceeding design requirements with high-heritage components at low risk.*

3.2.4 Attitude Control

A three-axis, closed-loop attitude control system (ACS) satisfies all pointing and stability requirements derived from science, downlink, and maneuver operations. Additional accommodation requirements are imposed by the

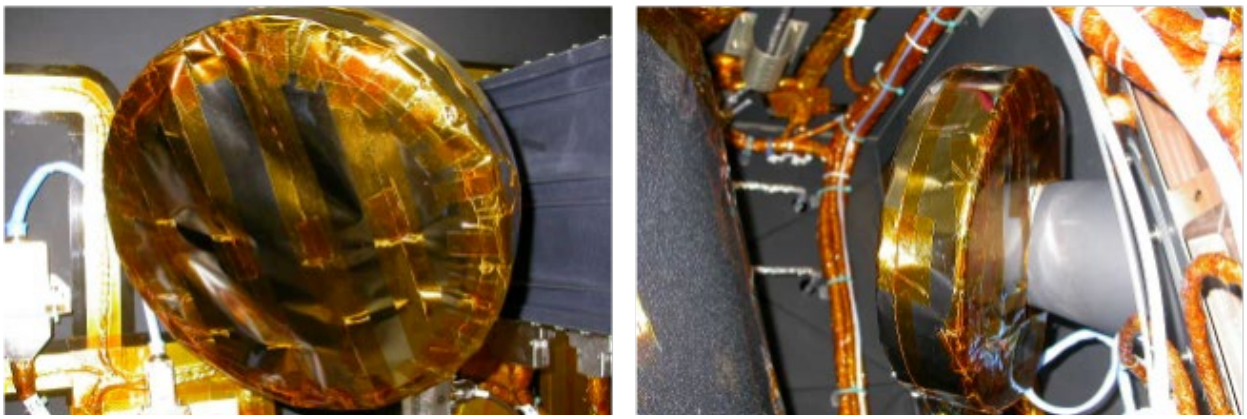

Exhibit 3-5. *STEREO reaction wheel MetGlass covers satisfied magnetic cleanliness requirements.* This mitigation tactic allows for the use of reaction wheels on InterMeso without compromising the need for a magnetically clean spacecraft.

magnetic field, electric field, and low-energy electron measurements. The ACS easily achieves the science and Ka-band downlink control requirements of 0.15°, 3-sigma about all three axes and the STIX-required stability of 5 arcsec over a 10-s interval. Star trackers provide inertial attitude knowledge to much better than the 0.1° required by science observations.

All requirements are satisfied using commercial off-the-shelf (COTS) components with multiple potential vendors. Two star trackers sharing an electronics box and an inertial measurement unit (IMU) are used for nominal attitude determination (**Exhibit 3-3**). The system is fault tolerant to one tracker failure or an IMU failure after the drift-rate setting burns 8 months after launch. Eight Sun sensors are used for safing operations and initial attitude determination after launch vehicle separation. Actuators include reaction wheels, thrusters, and an HGA gimbal with one degree of freedom. Four, 12 Nms reaction wheels provide attitude control in nominal operations (**Exhibit 3-3**). The reaction wheels are shielded with high heritage and flight proven MetGlass, similar to STEREO as shown in **Exhibit 3-5**, and include filter boxes to minimize electromagnetic interference. The thrusters are used for delta-V maneuvers, momentum management and attitude control during maneuvers. The HGA gimbal enables simultaneous Ka-band downlink and science data collection throughout the science phase.

3.2.5 Avionics

A single-string system consisting of an Integrated Electronics Module (IEM) and eight Remote Interface Units (RIU) contains all the hardware essential to run onboard flight software (FSW), provide data interfaces for all components, store science and engineering data, provide thruster control, and provide a sync pulse for power supply switching frequency synchronization (**Exhibit 3-3**).

The IEM consists of a Single Board Computer (SBC), a Spacecraft Interface Card (SCIF), a Thruster/Actuator Controller (TAC), and the DC/DC converter. The SBC includes a single radiation-hardened, UTC-700 100-MHz processor with 256 MB of SDRAM, 8 MB of MRAM for code storage, and 256 GB of flash storage for science and engineering data storage. *This SBC architecture leverages existing technologies developed for the Parker Solar Probe (PSP) and the Double Asteroid Redirection Test (DART) missions.* The SCIF is responsible for interfacing with the majority of the spacecraft components via SpaceWire, UART, or I2C interfaces. The SCIF SpaceWire router distributes virtual time codes throughout the system using the radio precision oscillator as its clock source. The SCIF also provides a sync pulse to the power supply switching frequencies across the spacecraft to minimize interference with the electric field instruments suite. *This technique was demonstrated on multiple missions, most recently PSP.* RIUs provide distributed, multi-channel data acquisition for temperature sensors and other housekeeping data.

3.2.6 Flight Software

The science data storage and downlink are the primary, mission-specific drivers of the InterMeso FSW design. FSW uses a layered architecture to encapsulate functionality into multiple, distinct applications as shown in **Exhibit 3-6**. *Limited new application development is required for InterMeso due to substantial re-use from past missions.* AES-128 encryption, being developed for the Interstellar Mapping and Acceleration Probe (IMAP), is

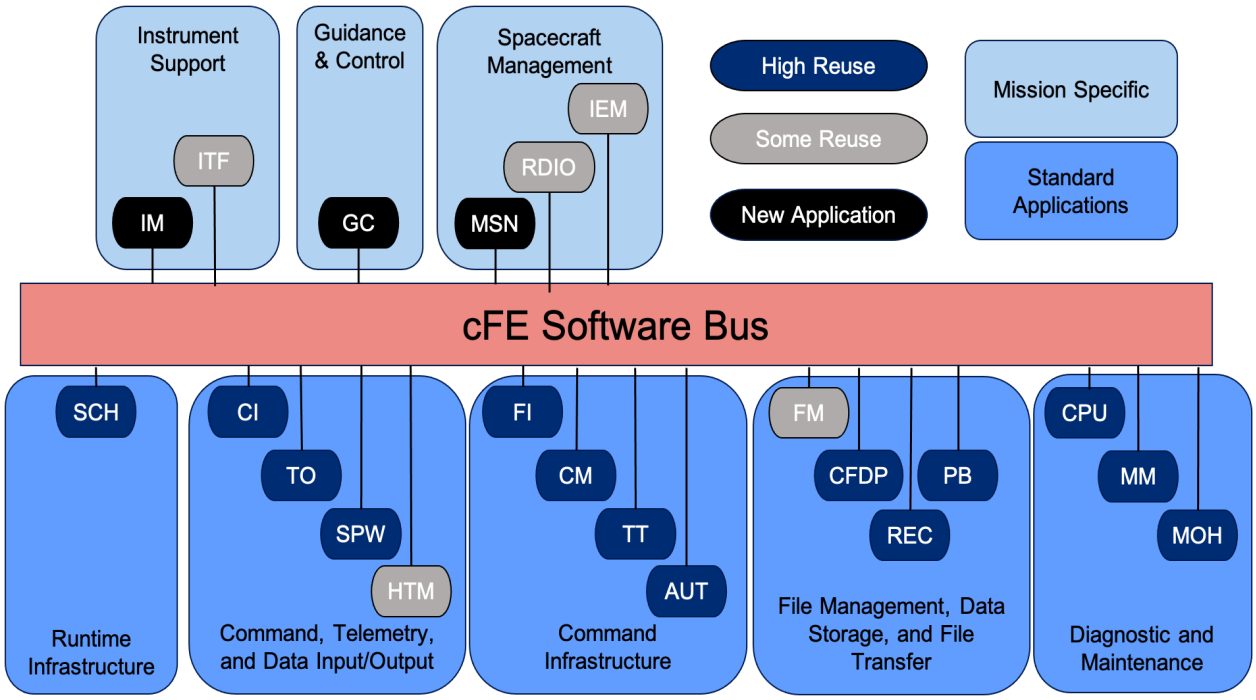

Exhibit 3-6. InterMeso will use high-heritage FSW architecture without the need for significant software development.

employed to comply with NASA's new uplink encryption guidelines. Downlink data rates are capped at 900 kbps to keep central processing unit (CPU) usage margins in acceptable ranges during simultaneous data collection and downlink operations.

3.2.7 Radio-Frequency (RF) Communications

A single-string, dual-band RF system provides low-rate uplink and downlink capability at any inertial attitude throughout the mission while also enabling high-rate science downlink during the science phase. Two X-band-only low-gain antennas (LGAs) provide near omnidirectional uplink and downlink during launch, trajectory correction maneuvers, and safe mode operations. A 0.9-m, Ka-band-only HGA allows for high-rate downlink. Gimbaling the HGA in the ecliptic plane enables simultaneous science recording and downlink through the primary mission and extended mission. During Ka-band downlink, CCSDS File Delivery Protocol (CFDP) transactions are completed via X-band uplink. The high-heritage APL Frontier Radio includes Ka-band transmit capability as well as X-band transmit and receive capability. The radio also includes an evacuated miniature crystal oscillator providing primary clocking for the entire spacecraft. Two, independent, COTS traveling wave tube amplifiers enable non-simultaneous Ka-band downlink and X-band downlink. The 80-W Ka-band traveling-wave tube amplifier (TWTA) produces 34 W of RF power while the 46-W X-band TWTA produces 22 W of RF power. Compensation magnets will be placed around both traveling wave tubes based on magnetic characterization testing occurring after integration to satisfy magnetic cleanliness requirements.

3.2.8 Power Generation, Storage, and Distribution

Near constant solar range, minimal unique power modes, lack of eclipses, and minimal solar array off-pointing all allow for a simple power generation, storage, and distribution subsystem design. Special considerations for magnetic cleanliness and surface charging are included to guarantee high-quality magnetic field and low-energy electron measurements. A peak power tracking topology composed of two deployed solar arrays, a lithium-ion battery, and high-heritage electronics boxes meets all system requirements.

Each solar array includes 1.5 m^2 of triple junction gallium arsenide (GaAs) based solar cells with individual cell bypass diodes. Combined, the total solar cell area of 3 m^2 is expected to produce 507 W at the end of life (accounting for environmental degradation). Strings of solar cells are arranged to reduce the magnetic signature of the arrays enabling high fidelity magnetic field measurements. Black Kapton backing, 6-mm-thick cover glass

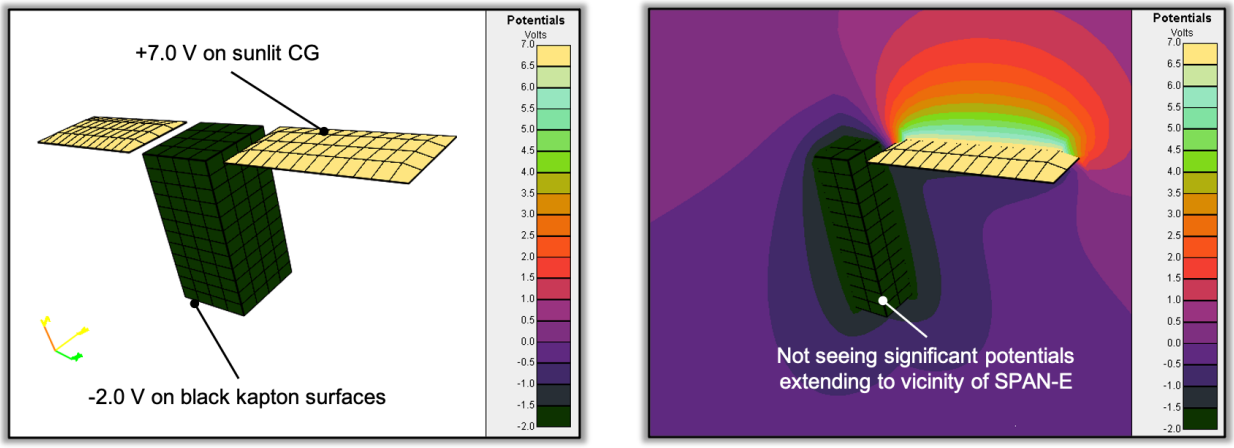

Exhibit 3-7. *Initial surface charging analysis of an InterMeso spacecraft at 1 au.* Current charging mitigation procedures can accommodate the cleanliness requirements for low energy electron measurements by SPAN-E.

with anti-reflective (AR) coatings over indium-tin-oxide coating, and wing grouting are implemented to mitigate surface charging affecting low-energy electron measurements. Initial analysis of surface charging effects after these mitigation strategies, shown in **Exhibit 3-7**, indicate low voltage potentials near the SPAN-E mounting location, enabling low-energy electron observations.

The 25 A-Hr lithium-ion battery, previously flown on PSP, provides power during the launch operations and provides supplemental power during peak load operations. Battery design includes custom wire routing to minimize the net magnetic dipole moment and field as demonstrated on PSP. The Power System Electronics (PSE) and Power Switching Unit (PSU), two high-heritage electronics boxes, are used to implement an unregulated, battery-dominated main bus ranging between 22 and 35 V.

3.2.9 Redundancy and Fault Tolerance

Selective and operational redundancy strategies are employed throughout the flight systems balancing perceived reliability risks and cost impacts. System redundancy and fault tolerance implementations are highlighted in **Exhibit 3-8**.

Subsystem	Component	Fault Tolerance Description
ACS	Reaction Wheels	Four-wheel design tolerant of single wheel failure
ACS	Star Trackers	Two heads design tolerant against single head failure
ACS	IMU	Star tracker rate determination capability tolerant to IMU failure during the science phase of the mission
ACS	Sun Sensors	Provides independent, time-insensitive attitude verification capability
RF	LGAs	Two LGAs tolerant to a damaged LGA or some cases of a stuck RF switch
Power	Buck Converters	Multiple buck converters tolerant to single buck converter failure
Power	Solar Array Strings	Multiple strings tolerant to single-string failure
Power	Battery Cells	Multiple Battery Cells tolerant of single cell failure (only used during launch)
Power	Hardware Command Loss Timer	Enabled full spacecraft power-cycle after an extended loss of communications
Power/Avionics	Launch Vehicle (LV) Separation	Separation detection is conducted independently by two different subsystems, both fault tolerant of at least one separation switch failure
Propulsion	Latch Valves	Parallel latch valves are tolerant against a single latch valve failed closed
Avionics	Remote Interface Unit (RIUs)	Two strings of RIUs make pressure and temperature telemetry tolerant to a single RIU string failure
Avionics	SRAM and MRAM	Error detection and correction make system tolerant to radiation induced single bit errors

Exhibit 3-8. *Fault tolerance table.*

Flight System Element Parameters	Value
Design Life, months (Commissioning + Science)	44 months
Structure	
Structure material	Aluminum Honeycomb
Number of articulated structures	One (HGA)
Number of deployed structures	Six (Magnetometer boom, two solar arrays, three electric field antennas)
Thermal Control	
Type of thermal control used	MLI blankets, radiators, and thermostatically controlled heaters with selectively isolated components (battery, SPICES, and STIX)
Propulsion	
Estimated delta-V budget, m/s	75 m/s ± 3 m/s (Attitude Control System)
Propulsion type(s) and associated propellant(s)/oxidizer(s)	Chemical Propulsion (hydrazine)
Number of thrusters and tanks	Four thrusters One tank
Specific impulse of each propulsion mode, seconds	215 s
Attitude Control	
Control method	3-axis
Control reference	Solar (Safe), Stars (all other modes)
Attitude control capability, degrees	0.1° 3-sigma
Attitude knowledge limit, degrees	0.01° 3-sigma
Agility requirements	None
Articulation/#–axes	One-axis HGA gimbal
Sensor and actuator information	Eight coarse Sun sensors (0.5° 1-sigma) Two star trackers (<10-arcsec accuracy 3-sigma) One MIMU (≤0.005°/hr bias 1-sigma, ≤0.005°/hr ARW 1-sigma) Four RWAs (75-mNm torque, 12-Nms angular momentum storage per wheel)
Command & Data Handling	
Flight Element housekeeping data rate, kbps	<10 kbps
Data storage capacity, Mbit	265000 Mbit
Maximum storage record rate, kbps	100 kbps
Maximum storage playback rate, kbps	900 kbps
Power	
Type of array structure	Rigid deployment
Array size, meters × meters	Two equally sized arrays with a total area of 3 m^2
Solar cell type	Triple junction GaAs
Expected power generation at beginning of life (BOL) and end of life (EOL), watts	507 (EOL)
On-orbit average power consumption, watts	334 W (CBE)
Battery type	Li-ion
Battery storage capacity, amp-hours	25 A-hr

Exhibit 3-9. *Flight system element summary table.*

3.3 Mission Design and Concept of Operations

3.3.1 Mission Design Overview

The InterMeso mission design and concept of operations seek to remain flexible while minimizing planning complexity, unique on-orbit activities, DSN time, and ultimately cost. **Exhibit 3-10** gives a notional timeline for the mission with a launch in 2033 to coincide with the ascending phase of the solar cycle, but this is adjustable via daily launch opportunities throughout the 2030 decade with little variation in C3 requirements. Spacecraft are operationally independent with dedicated uplink and downlink capabilities. All spacecraft remain in proximity of each other for the first 8 months of the mission for commissioning. After commissioning the spacecraft perform rate-setting burns, the only deterministic delta-V burns, giving them unique

Event	Date
Launch	01 August 2033
Science Phase Start	30 March 2034
End of Nominal Mission	30 March 2037

Exhibit 3-10. *Baseline mission timetable.*

heliographic drift rates. These burns mark the start of the three-year Science Phase which concludes with the final geometry shown in **Exhibit 3-11**.

3.3.2 Launch and Commissioning Phase

All four spacecraft are launched together into heliocentric, Earth-trailing orbit, and all with the same initial drift rate before maneuvers separate the spacecraft. The initial drift rate during commissioning is the intermediate drift rate, as compared to the final spacecraft respective drifts, selected to minimize spacecraft delta-V burden (i.e., two spacecraft speed up, and two slow down). **Exhibit 3-12a** shows the initial drift rate set by the launch vehicle (green line) as well as the drift rates of each InterMeso spacecraft throughout the mission. This trajectory also maintains an inter-spacecraft separation of <0.01 au at all times while keeping the entire constellation between a heliographic distance of ~0.97 and 1.05 au over the course of the prime mission.

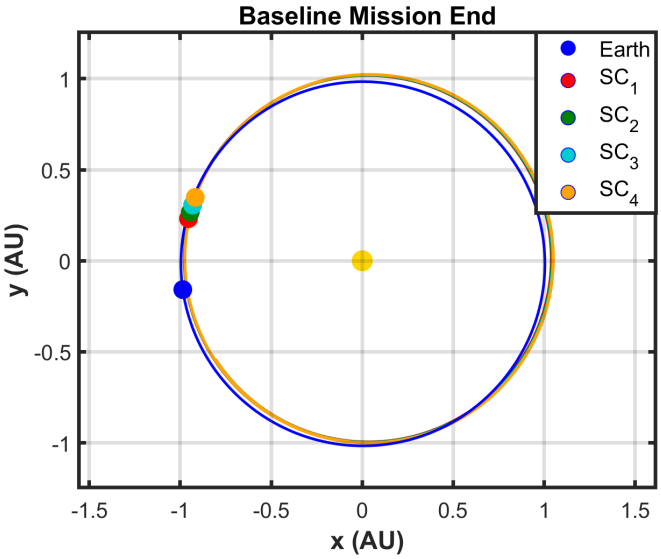

Exhibit 3-11. *Spacecraft configuration relative to Earth at the end of the nominal mission.* InterMeso will explore the range of mesoscale separations in the pristine solar wind while maintaining a relatively close proximity to Earth.

These drift rates allow the spacecraft to slowly separate and allow sampling of the solar wind at inter-spacecraft separations spanning the full range of mesoscale dynamics (as illustrated in **Exhibit 1-2**). **Exhibit 3-12b** illustrates the cumulative combined days at various inter-spacecraft separations for both the three-year prime mission (black line) and for the inclusion of a two-year extended mission (red-dotted line). The inclusion of the 2-year extended mission phase, especially, provides additional opportunity for sampling mesoscale structuring near the transition from the inertial to the injection range; however, this additional sampling is not required for addressing the primary science goals.

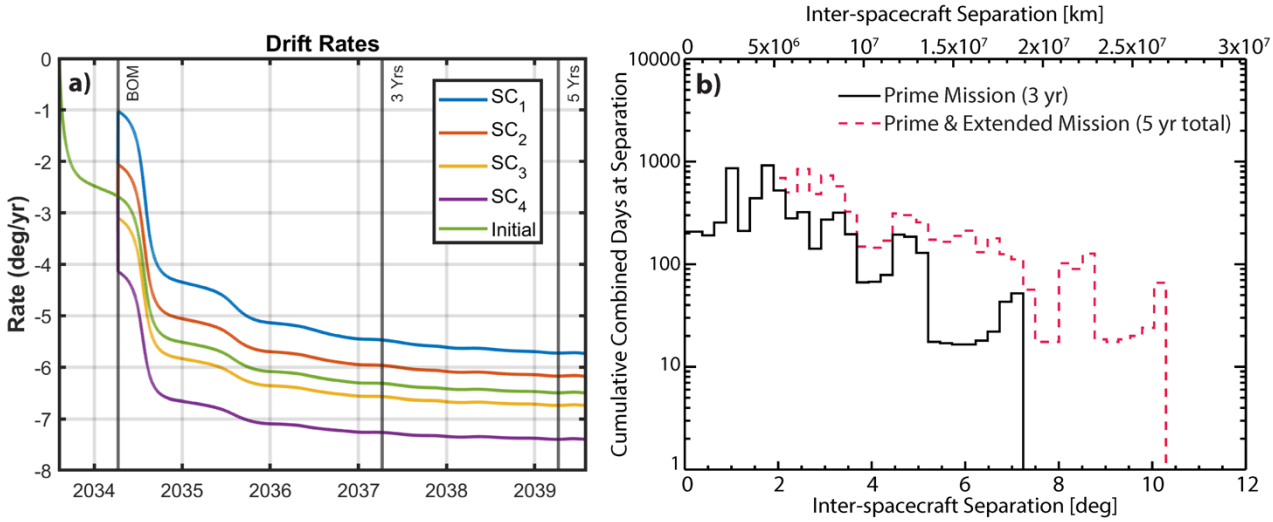

Exhibit 3-12. *(a) Change in Earth-relative drift rate over the course of the mission. The "initial" line represents the drift rate targeted by the launch vehicle. (b) Cumulative combined days the InterMeso spacecraft will spend at different inter-spacecraft separations over the prime mission (black) plus extended mission (red). Cumulative combined days is the sum of the number of days spent at each separation for each spacecraft pair (i.e., spacecraft 1&2, 1&3, 1&4, 2&3, 2&4, and 3&4).*

InterMeso is not launch vehicle capability constrained but requires a 5-m fairing due to volume constraints. Ample delta-V margin easily accommodates expected launch vehicle insertion errors, with the expected statistical delta-V from insertion errors corresponding to an Atlas V / Falcon 9 class launch vehicle around 4 m/s. The launch vehicle initiates spacecraft separation which triggers an on-board, autonomous post-separation sequence. The autonomous sequence establishes contact with the ground before continuing through the only two mission critical events: detumble and solar array deployment. Commissioning continues for the next 8 months completing all deployments, checkout activities, inter-spacecraft calibrations and outgassing. Eight months after launch the spacecraft reach perihelion, the optimal location to set individual drift rates.

Drift rates are set via deterministic delta-V burns that are tailored for each spacecraft. These burns are vectored perpendicular to the Sun line in either in the RAM or anti-RAM direction, with magnitudes less than 45 m/s. Each spacecraft carries enough propellant to perform the distribution burns at any point in the orbit but propellant usage is minimized with burns near perihelion. Launch information and details on the individual burse are provided in **Exhibit 3-13**.

3.3.3 Science Phase

The science phase begins immediately after the drift rate burns. All instruments are powered and constantly collecting data at a rate of 89.7 kbps (current best estimate [CBE]) in the science phase. The data are divided into two groups, survey data collected at 19.4 kbps (CBE) and burst data collected at 70.3 kbps (CBE). All survey data are downlinked throughout the mission within a week of collection. After downlink, survey data are evaluated on a weekly to biweekly cadence to determine time periods of interest. Burst data from time periods of interest, such as near shock crossings, are then downlinked in subsequent contacts interleaved with newer survey data. Burst data are maintained on-board the spacecraft for at least 3 weeks before deletion and at least 4

Parameter	Value		Units
Launch C_3	1.52		km^2/s^2
Launch RA & Dec of Outgoing Asymptote	RA	305.5	deg
	Dec	0	
Initial Drift Rate Targeted by Launch Vehicle	4		deg/year
Drift Rates Targeted by Spacecraft	SC-A	2.5	
	SC-B	3.5	
	SC-C	4.5	
	SC-D	5.5	
Deterministic delta-V	SC-A	44.3	m/s
	SC-B	11.6	
	SC-C	11.2	
	SC-D	39.0	
Mission Lifetime	44		months
Maximum Eclipse Period	None in baseline mission		
Launch Site	CCAFS		
Dry Mass **with** Allocated Margin	377.3 (per vehicle)		kg
Propellant Mass **without** Allocated Margin	16.5 (per vehicle) 66 (total)		
Propellant Allocated Margin	233		%
Propellant Mass **with** Allocated Margin	55 (per vehicle) 220 (total)		kg
Launch Adapter Mass **with** Allocated Margin	279.37		
Total Launch Mass **with** Allocated Margin	2008.5		
Launch Vehicle	Option 2		Type
Launch Vehicle Lift Capability	3135		kg
Unallocated Launch Vehicle Mass Margin	1127		
	56		%
Total Launch Vehicle Mass Margin	1436		kg
	85		%

Exhibit 3-13. *Mission design table.*

Downlink Information	Early Commissioning	Late Commissioning	Primary Mission Science Phase
Number of Contacts per Week (Includes all four spacecraft)	14 contacts, 112 hr/wk total	8 contacts, 64 hr/wk total	4 contacts, 22 hr/wk total
Number of Weeks for Mission Phase	8 weeks	24 weeks	156 weeks
Downlink Frequency Band	8.4 GHz (X-band)	32 GHz (Ka-band)	32 GHz (Ka-band)
Single-Spacecraft Data Rate	286 kbps	900 kbps	900 kbps
Transmitting Antenna Type and Gain	LGA, 6.2 dBi	HGA (0.9 m), 46.6 dBi	HGA (0.9 m), 46.6 dBi
Transmitter Peak Power	22 W	34 W	34 W
Downlink Receiving Antenna Gain	78 dBi	78 dBi	78 dBi
Transmitting Power Amplifier Output	22 W	34 W	34 W
Total Mission Daily Data Volume (includes all 4 spacecraft)	2060 MB/day	3700 MB/day	1270 MB/day
Uplink Information	**Early Commissioning**	**Late Commissioning**	**Primary Mission Science Phase**
Number of Uplinks per Day	14 contacts, 112 hr/wk	8 contacts, 64 hr/wk	~4 contacts, 22 hr/wk
Uplink Frequency Band	7.2 GHz	7.2 GHz	7.2 GHz
Telecommand Data Rate	0.500	0.500	0.125
Receiving Antenna Type and Gain	LGA, 6.5 dBi	LGA, 6.5 dBi	LGA, 6.5 dBi

Exhibit 3-14. *Mission operations and ground data systems table.*

hours of burst data are downlinked each week per spacecraft. This data selection scheme is similar to what is used on Parker Solar Probe and the Magnetospheric Multiscale Mission (MMS), except with a significantly more relaxed burst selection cadence than the latter.

3.3.4 Extended Mission

InterMeso offers multiple extended mission possibilities to enable flexibility based on future realized science gaps or opportunities. After the primary mission the spacecraft continue to drift away from Earth, as well as continue to separate from each other, at near constant rates. Data rates and DSN weekly loading are maintained for the first year of the extended mission. Subsequent years require either more DSN time or a reduction in data volume (e.g., reduced or eliminated burst mode selections). Sufficient additional propellant is included on each spacecraft to either null the drift rates (i.e., fix the inter-spacecraft separations) or capture the spacecraft in an L5 orbit. Drift rate nulling idealistically occurs at any annual perihelion during the extended mission, locking in constant spacecraft-Earth ranges and inter-spacecraft separation distances. The spacecraft could be placed in either an equally spaced configuration, or repositioned into a staggered inter-spacecraft separation, as motivated by the scientific community. *Insight throughout the prime mission will best dictate the optimal extended mission architecture for science return which the flexible mission design can accommodate.*

3.3.5 Concept of Operations Analogies

InterMeso's concept of operations most closely resembles the Double Asteroid Redirection Test (DART) for the commissioning phase and the Solar Terrestrial Relations Observatory (STEREO) for the science phase. No commissioning activities are time sensitive and all offer numerous backup opportunities. After completion of the operationally intensive early-commissioning activities in the first 2 months the mission enters a quiescent period with predominantly unattended ground contacts, similar to DART. The science phase shares similar DSN time per spacecraft needs with STEREO. Unlike STEREO, these contacts are predominantly unattended, similar to Van Allen Probes and DART. Information on the Concept of Operations are provided in **Exhibit 3-14**.

3.4 Ground-Based Observatories

No ground-based observations are planned for baseline science. However, many additive synergies exist between InterMeso observations and ground-based observatory measurements (e.g., DKIST and the Multi-slit Solar Explorer, MUSE).

ID	Statement [L × C Score]	Description/Mitigation
A	If any single-point failures in the current architecture occur, THEN mission will be unable to meet Level 1 requirements **[Technical 2 × 5]**	• Selective redundancy employed throughout the system in areas of greatest perceived risk, see **Section 3.2.9**, Redundancy and Fault Tolerance
B	IF adequate Environmental Test Facilities are not available during Phase C, THEN then Phase D and SIR will be delayed. **[Schedule 2 × 3]**	• Multiple units can be tested simultaneously • Additional environmental facilities may need to be added to keep up with component throughput
C	IF a hardware failure is experienced during spacecraft environmental testing on a unit other than the first unit THEN previously delivered hardware will need to be proven unaffected or potentially retested **[Cost/ schedule 1 × 4]**	• Qualification testing on the first two spacecraft increases the likelihood of finding common failures with that set • Acceptance testing for the last two spacecraft reduces the likelihood of failures occurring
D	IF a hardware failure is experienced during box-level environmental testing on a unit other than the first unit THEN previously delivered hardware will need to be proven unaffected or potentially retested **[Cost/schedule 1 × 3]**	• Qualification testing on the first unit increases the likelihood of finding common failures early in testing • Acceptance testing later units reduces the likelihood of failures occurring on subsequent units
E	IF adequate Fabrication Facilities for flight builds are not available during Phase C THEN then Phase D and SIR will be delayed **[Schedule 1 × 3]**	• Multiple units can be assembled simultaneously • Additional environmental facilities may need to be added to keep up with component throughput
F	IF adequate Integration and Test staffing is not available during Phase D THEN the launch readiness date will be impacted **[Schedule 1 × 3]**	• Involving Integration and Test staff with box development and testing makes staffing ramp up more gradual

Exhibit 3-15. *Risk list.*

3.5 Risk List

The top mission risks are shown in **Exhibit 3-15** and listed along with mitigation plans in **Exhibit 3-16**. They are classified as either technical, schedule, or cost/schedule. Likelihood (L) and consequence (C) has been assessed for each. *The design of InterMeso with selective redundancies and the high heritage of its components and instruments make it a low-risk mission for consideration in the next decade.*

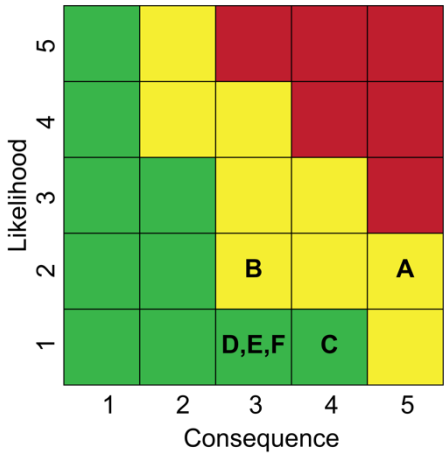

Exhibit 3-16. *Risk table.*

4. Development Schedule and Schedule Constraints

4.1 High-Level Mission Schedule

The InterMeso development schedule draws heavily from previous mission schedules, notably STEREO, input from key providers, and recent concept development efforts in the same class. A high-level notional mission schedule, presented in **Exhibits 4-1, 4-2,** and **4-3**, baselines a launch in 2033 and includes ample margin. A detailed presentation of the notional schedule is presented in **Appendix B**. As discussed in **Section 3.3**, the mission architecture allows for daily launch opportunities across a multi-year launch window providing substantial flexibility in Phase A start dates. No preformulation work is required before the start of Phase A. Instrument schedules were benchmarked using comparable instrument schedules from STEREO, PSP, Solar Orbiter, Europa Clipper, and direct input from instrument teams at the University of Michigan and the University of California, Berkeley.

4.2 Science, Technology Development Plan(s)

No new technology development plans need to be developed for InterMeso. The only technology not currently at TRL 6, the HVPS on SPICES, is under development via a NASA contract with expected completion in September 2022.

4.3 Development Schedule and Constraints

Project Phase	Approximate Duration (months)
A – Concept Study	9.4
B – Preliminary Design	14.5
C – Final Design & Fabrication	43.0
D – Obs I&T, Launch & Checkout	44.9
E – Primary Mission Operations	42.0
F – Extended Mission Operations	12.0
Start of Phase B to PDR	13.5
Start of Phase B to CDR	27.0
Start of Phase B to Delivery of First Instrument	39.9
Start of Phase B to Delivery of Last Instrument	53.7
Start of Phase B to Delivery of First spacecraft Component	38.0
Start of Phase B to Delivery of Last spacecraft Component	52.3
System-Level Integration & Testing	32.0
Project Total Funded Schedule Reserve	10.2
Total Development Time Phases B–D **(with Margin)**	102.5

Exhibit 4-1. *InterMeso phase and review date summary.*

The InterMeso mission features a flexible launch schedule with numerous backup launch options and ample margin. Daily launch opportunities exist throughout the beginning of the 2030 decade with little to no difference in required launch performance. Year to multi-year launch slips can be accommodated with a minimal impact to the science return. For this study launch, a 2033 launch was assumed to coincide with the ascending phase of the solar cycle. However, the prime science of InterMeso will have data sufficiency for any launch occurring during the ascending phase, likely ranging from 2033 to 2037. Schedule margin is well above institutional requirements and has been distributed throughout Phases C and D as shown in **Exhibits 4-4** and **4-5**.

Mission-Level Milestone	Date
System Requirements Review (SRR)	06/13/25
Preliminary Design Review (PDR)	05/04/26
Critical Design Review (CDR)	06/17/27
Mission/Science Operations Review (MOR/SOR)	09/05/29
System Integration Review (SIR)	01/02/30
Pre-Environmental Review (PER)	12/31/30
Operational Readiness Review (ORR)	01/26/33
Pre-Ship Review (PSR)	02/22/33
Mission Readiness Review (MRR)	07/01/33
Launch Readiness Review (LRR)	07/27/33
Launch Readiness Date (LRD)	08/01/33

Exhibit 4-2. *Mission-level milestones.*

SPAN-E instrument delivery is the projected critical path in Phase C, although final deliveries from all instrument teams are expected within a 6-month window (excluding STIX which is only delivering one flight unit). Flight Unit fabrication and environmental test facilities are expected to be used at capacity for a majority of Phase C with significant scheduling rigor required regardless of the implementing institution. Substantial effort by the implementing institution is required to manage facility schedules and determine if projected throughput is adequate. All spacecraft and instrument components are scheduled for delivery before the beginning of any spacecraft integration activities.

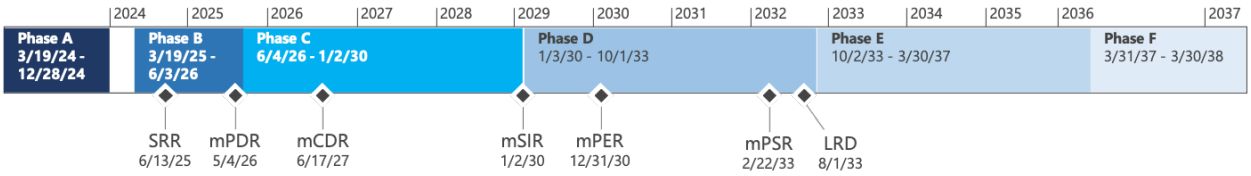

Exhibit 4-3. *InterMeso phase and review date summary.*

Phase D is projected to take about 3.5 years with the spacecraft integrated and tested in pairs. Pair integration start times are staggered by about a year to give enough time for the first pair to begin environmental testing before starting integration of the second. After completion of the environmental test the first pair of spacecraft go into storage while the second pair completes their environmental test campaign. This "buddy system" approach constrains the throughput expected from the harness and ground system equipment suppliers to production levels achieved on the Van Allen Probe and STEREO missions.

Funded Schedule Margin	Duration (Work Days)
Phase C	80.0
Phase D (I&T Site)	115.0
Phase D (Launch Site)	20.0

Exhibit 4-5. *Schedule margin table.*

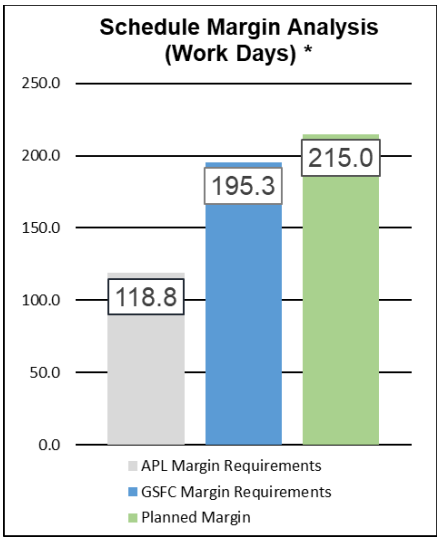

Exhibit 4-4. InterMeso has significant schedule margin above normal institutional requirements, lowering risk.

5. Mission Life-Cycle Cost

The total estimated cost of the baseline InterMeso mission (Phases A–E) with fees and unallocated cost reserves is $1,137 million in FY22 dollars. This estimate includes $200.7 million for Launch Vehicle and Services (LV&S), specifically, an Option-2 launch vehicle with 5-m fairing and launch vehicle adapter. Unallocated cost reserves are calculated as 50% of estimated Phase B–D costs excluding the price of LV&S, and 25% of estimated Phase E costs. DSN charges, while not included in the mission cost, are estimated to be $12.9 million through the end of Phase E. *This concept is ready for immediate implementation with no pre-Phase-A funding or technology development required.*

5.1 Costing Methodology and Basis of Estimate

Exhibit 5-1 summarizes the cost methodologies used to generate total mission costs.

WBS ID	WBS Description	Baseline Estimating Method and Supporting Information Summary
PH A	Phase A	• Historical trend for NASA robotic missions not requiring extensive technology development
01, 02, 03	Program Management, Systems Engineering, Safety & Mission Assurance	• Cost factor (16.5%) derived from APL and NASA historical mission data is applied to the sum of estimated costs of Instruments (WBS 05), Spacecraft (06), and System Integration & Test (10)
04	Science	• Sum of (1) engineering cost estimates for instrument support/calibration/etc. (2) part time Principal Investigator & Principal Scientist support and (3) analogy-based estimate for Science Operations Center (SOC) development
05	Instruments	• Instrument Management & Oversight cost is estimated by applying a cost factor derived from historical mission data (8.5%) to Instrument (WBS 05) estimated costs • Cost of the first flight unit covers delivery of one Engineering and one Flight Model (EM, FM) and General Support Equipment (GSE) • Except for the Thermal Ion Composition (SPICES) instrument, first flight unit costs were estimated by averaging 70th-percentile system-level cost estimate results from NASA Instrument Cost Model (NICM9) and SEER for Space model • For SPICES, the first flight unit cost estimate averaged 70th-percentile estimates from the subsystem-level NICM9 model and the TruePlanning cost framework • The cost of each additional flight unit (cost-to-copy factor) is 36% of the first flight unit cost, consistent with [Warfield and Roust, 1998]

WBS ID	WBS Description	Baseline Estimating Method and Supporting Information Summary
06	Spacecraft	• Spacecraft Hardware Subsystem-level costs are estimated by averaging STEREO, adjusted for InterMeso spacecraft subsystem MEV masses, and 70th-percentile results from the Galorath SEER for Space parametric modeling framework • Spacecraft FSW/Autonomy costs are estimated with staff-month profiles derived from PSP and recent APL missions
07	Mission Operations (MOPS)	• STEREO Mission Operations actuals with adjustments to support 2 additional spacecraft
08	Launch Vehicle & Services (LV&S)	• Option 2 price via Launch Vehicle & Services guidance • Prices for ESPA Ring and C-22 adapter hardware are drawn from previous estimates and will be paid for by implementing organization
09	Ground Data Systems (GDS)	• Detailed engineering estimate was prepared covering personnel, IT and communications hardware, and software licenses and development • Estimate assumes the availability of existing APL hardware infrastructure and software architecture
10	System Integration & Testing (SI&T)	• Estimate based on analysis of reported costs of integrating multi-spacecraft STEREO and Van Allen Probes (VAP) missions • SI&T costs were cross-checked against the cost history of the four-spacecraft Magnetospheric Multiscale (MMS) mission • Note: SEER and PCEC results understate estimate based on APL experience integrating and testing multiple spacecraft
E	Phase E Costs	• Cost based on analysis of costs of operating the multi-spacecraft VAP mission via unattended operations

Exhibit 5-1. *Cost methodology table.*

5.2 Cost Estimate

Total mission cost is summarized in **Exhibit 5-2** with an annualized spending presented in **Exhibit 5-4** and **5-5**. Additional cost estimating details are presented in **Appendix E**. As shown in **Exhibit 5-3**, *the Phase A–D cost of InterMeso is comparable to recent STP-class solar wind and/or multipoint missions.*

WBS ID	Description	Cost ($M FY22)	Basis, Comments
Ph A	Phase A	$ 6.0	Assumption based on previous missions
01, 02, 03	PMSEMA	$ 68.7	A-D wrap up based on recent STP missions
04	Science	$ 22.8	Estimated from recent STP missions
05	Payloads	$ 149.3	See **Exhibit E-2** for details
	Instrument Management & Oversight	$ 11.7	
	Instruments	$ 137.6	
06	Spacecraft	$ 205.1	See **Exhibit E-3** for details
	Hardware	$ 189.7	
	FSW Development	$ 15.4	
07	Mission Ops (B–D)	$ 24.1	Based on STEREO, scaled for 4 spacecraft
08	Launch Vehicle & Services (LV&S)	$ 200.7	Option 2 LV&S, including Launch Vehicle Adapter
09	Ground Data Systems	$ 14.9	InterMeso specific estimate from GDS lead
10	I&T	$61.8	Includes testbeds
A-D BASE	**Baseline (without reserves and LV&S)**	**$ 552.7**	**Excluding Option 2 LV&S price**
A-D BASE	**Baseline (without reserves)**	**$ 753.4**	**Including Option 2 LV&S price**
A-D RES	Unallocated Cost Reserves	$ 273.3	50% of Phase B–D Baseline costs, excluding $200.7M Option 2 LV&S price
Ph A-D	**Phases A–D with Reserves**	**$ 1026.7**	
E	**Phase E Baseline**	**$ 88.3**	**Including all costs except DSN charges**
E RES	**Phase E Cost Reserves**	**$ 22.1**	**25% of Phase E Baseline**
A-E BASE	**Phases A–E**	**$ 841.7**	**Baseline (including LV&S), excludes Cost Reserves**

Exhibit 5-2. *Estimated Phase A–E costs for the InterMeso mission (in millions of FY22 dollars) by WBS element.*

There is high confidence that InterMeso can be implemented for less than the estimated mission cost with reserves, in part for the following reasons:

- All InterMeso hardware will be at or above TRL 6 and *no additional pre-Phase-A or Phase-A/B funding is required for technology development activity.* All spacecraft hardware and instruments described in this report have been delivered to previous missions except for the Thermal Ion Composition (SPICES). University of Michigan is now developing SPICES TRL-6 test hardware with NASA funding for September 2022 delivery.
- Costs to deliver exact copies of instruments and spacecraft components was drawn from cost histories of APL multi-spacecraft missions such as STEREO and Van Allen Probes (VAP). For these missions only

one copy was delivered, rather than three copies following the original needed for InterMeso. *InterMeso may realize additional savings on the second and third copies of the instruments.*

- Parametric estimates were conservatively generated using 70th-percentile values based on MEV inputs (i.e., including 15% mass margin and 30% power margin) and include management and oversight costs. *As several instruments are high heritage, the margins applied are robust.*

As a result, the proposed Phase A–D cost, with reserves and LV&S, of just over $1,026 million ($826 million without LV&S) appears to be a conservative estimate for a Class-C mission that is ready to implement as soon as the Solar and Space Physics (Heliophysics) Decadal Survey is published without need for additional technology development.

	FY24	FY25	FY26	FY27	FY28	FY29	FY30	FY31	FY32	FY33	Total
Baseline excluding LV&S	$4	$28	$56	$92	$105	$88	$71	$54	$37	$19	**$553**
Reserves	-	$13	$28	$46	$52	$44	$36	$27	$19	$9	**$273**
LV&S	-	-	-	-	-	-	-	$67	$67	$67	**$200**
Total	$4	$41	$84	$138	$157	$132	$107	$148	$123	$95	**$1027**

Exhibit 5-4. *Estimated Phase A–D InterMeso budget profile table (in millions of FY22 dollars). Cells may not add across due to rounding.*

5.2.1 Phase E and Extended Mission Cost Estimates

Cost estimates of both Phase E and the extended mission were calculated by extrapolating VAP costs. The mission operations for the four spacecraft were conservatively estimated as being twice the two-spacecraft VAP mission. Additionally, GDS and instrument labor costs were estimated to increase by 25% from the VAP costs. See **Exhibit 5-5** for Phase E and extended mission cost profiles for Mission Operations, Ground Data Systems, and Instrument labor.

	Commissioning and Primary Mission (44 months)				Extended Mission (24 months)	
	Year 1	Year 2	Year 3	Year 4 (8 months)	Year 1	Year 2
Annual Cost	$22,806	$25,604	$26,260	$13,650	$18,644	$24,354
Monthly Cost:	$1,900	$2,134	$2,188	$1,706	$1,554	$2,029
Percent of Max Cost	87%	98%	100%	78%	71%	93%

The Phase E cost is thus estimated to be slightly more than $88 million for the prime mission (including commissioning) for an average monthly cost of roughly $2 million. The cost of a possible 2-year extended mission is estimated to be $43 million, with an average monthly cost of $1.8 million. Extended mission costs could be lowered with a simplified Concept of Operations that eliminates burst mode coverage.

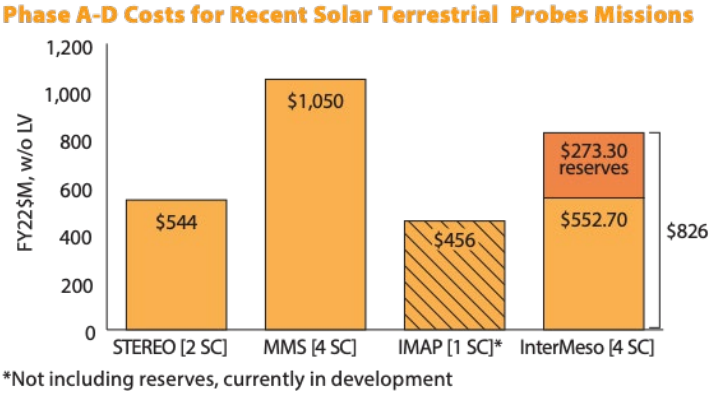

Exhibit 5-3. *Phase A–D cost of InterMeso with 50% reserves compared to the previous three STP-class missions.* InterMeso is well within the family of costs for the STP program.

5.2.2 Summary

The Phase A–D cost estimate for InterMeso demonstrates that the mission can be realized for $826 million (FY22, excluding launch vehicle) including 50% Phase B–D reserves, putting it well within historical STP missions (**Exhibit 5-3**). Cost confidence and risk analysis (**Appendix E**) indicate a high level of certainty that the mission could be completed within the allotted cost with reserves. *InterMeso is well within the historical cost scope of an STP-class mission with STP-class science objectives and is actionable within the next decade without additional technology investment or development.*

Appendix A: APL Margin and Risk Definitions

Margin Calculations

All technical resource margins are calculated using APL Quality Management System Standards. Unallocated margin is calculated as follows:

$$Unallocated\ Margin = Max\ Possibie\ Value - Max\ Expected\ Value$$

$$Unallocated\ Margin(\%) = \left(\frac{Max\ Possible\ Value - Max\ Expected\ Value}{Max\ Expected\ Value}\right) \times 100\%$$

The total margin is expressed as the sum of the allocated and unallocated margins calculated as follows:

$$Total\ Margin = Max\ Possible\ Value - Current\ Best\ Estimate$$

$$Total\ Margin(\%) = \left(\frac{Max\ Possible\ Value - Current\ Best\ Estimate}{Current\ Best\ Estimate}\right) \times 100\%$$

Risk Definitions

The risks and consequences identified in **Section 3.5** were evaluated using the standard rankings defined in **Exhibits A-1** and **A-2**.

Likelihood of Risk	
1. Very Low	Tech: 0.1% < P < 2%; Cost/Sched: P < 10%
2. Low	Tech: 2% < P < 15%; Cost/Sched: 10% < P < 25%
3. Moderate	Tech: 15% < P < 25%; Cost/Sched: 25% < P < 50%
4. High	Tech: 25% < P < 50%; Cost/Sched: 50% < P < 75%
5. Very High	Tech: P > 50%; Cost/Sched: P > 75%

Exhibit A-1. *Definition of risk likelihood.*

Consequence of Risk	
1. Very Low	Minimal impact to schedule, cost, performance, or design margin
2. Low	Potential overrun < 3%; non-critical path schedule slip; decrease in spacecraft or payload capability/margin but mission requirements met
3. Moderate	Potential overrun 3–10%; schedule slip affecting critical path, but not delivery; major loss of capability
4. High	Potential overrun > 10%; schedule slip 1–3 months; failure to meet > one L1 requirement; loss of functionality
5. Very High	Potential overrun > 20%; >3-month schedule slip; loss of spacecraft or payload

Exhibit A-2. *Definition of risk consequence.*

Appendix B: Detailed Schedule (Phases B–D)

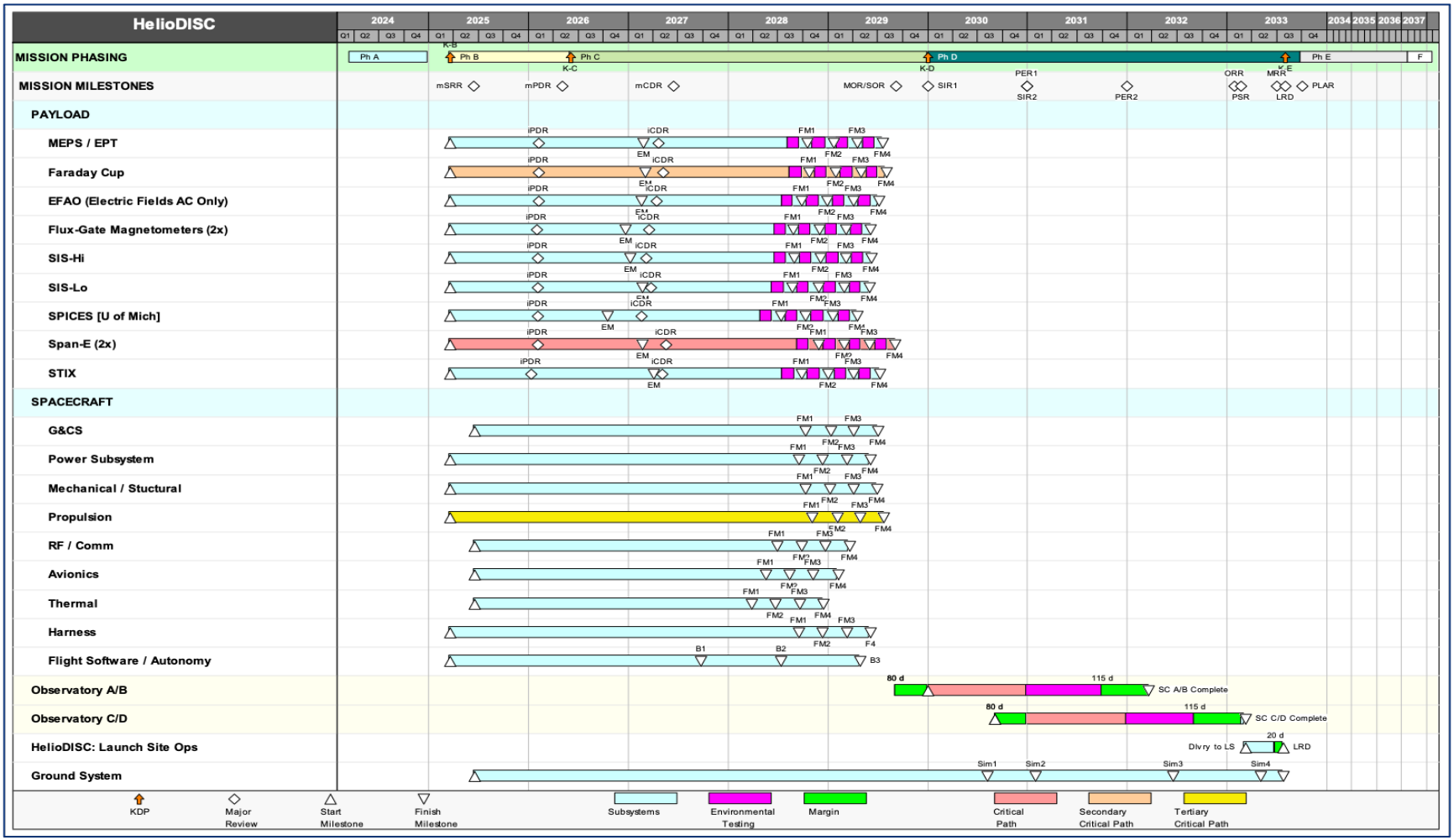

Exhibit B-1. *Detailed InterMeso schedule for Phases B–D.*

Appendix C: Detailed Instrument Descriptions

Faraday Cup

Bulk solar wind plasma moments (density, velocity, temperature) are captured via a Faraday cup, which has a long history on spaceflight missions including Voyager 1 and Voyager 2, Wind, Parker Solar Probe, and the upcoming Europa Clipper and HelioSwarm missions. Faraday cups measure current produced on a metal plate by charged particles. Placing a charged grid over the Faraday cup rejects particles with a parallel energy/charge under the voltage applied to the grid, while particles with an $E_{\parallel}/q$ larger than the voltage on the grid enter the sensor. Oscillating the voltage of the grid between produces an alternating current (AC) on the back plate, which is recorded by the instrument electronics. Dividing the back plate into wedges allows for the construction of a reduced distribution function of the thermal solar wind ions, and the ratio of the currents give the precise flow angle of the plasma.

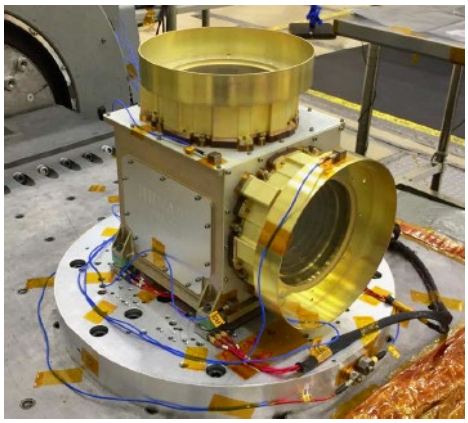

Exhibit C-1. *Photo of the Europa Clipper PIMS Faraday cup used as the basis for InterMeso. InterMeso would only require one cup with less shielding.* Currently TRL 7 with pathway to higher TRL after launch in 2024.

The InterMeso Faraday cup is baselined off a single-cup version of the Plasma Instrument for Magnetic Sounding (PIMS), which will fly on Europa Clipper (*Grey et al.*, 2018; **Exhibit C-1**). A single Faraday cup is all that is required to produce bulk solar wind ion measurements. Significant mass savings from the initial PIMS design were realized by lessening the radiation shielding and removing foils/grids for electron observations. The Faraday cup produces both survey and burst data. The CONOPS for the handling of these data streams in presented in **Section 3.2**. PIMS has already gone through environmental testing and has been delivered and is due to launch in 2024. Due to only minor design simplifications of PIMS (e.g., removing passive radiation shielding and only comprising one Faraday cup rather than the two-per-unit on PIMS), the TRL of the instrument is assessed at 7. Specifications for the modified PIMS used in this study are given in **Exhibit C-2**.

Item	Value
Size/dimensions	0.3 × 0.29 × 0.23 m
Instrument mass (CBE)	5.9 kg
Instrument average payload (CBE)	5.0 W
Instrument science data rates (CBE)	3 kbps (survey) 5 kbps (burst)
Instrument Fields of View	90° cone
Pointing requirements (knowledge)	<0.5°
Pointing requirements (control)	Few degrees
Pointing requirements (stability)	n/a

Exhibit C-2. *InterMeso Faraday cup specifications.*

While this report baselined a modified PIMS, multiple institutions are currently developing and/or operating alternative Faraday cups with TRLs ranging from 6 to 9, allowing multiple partners to compete for this instrument in an open bid.

SPICES

The Solar wind and Pickup Ion Composition-Energy Spectrometer (SPICES) is a time-of-flight energy (ToF-E) spectrometer dedicated to measuring the thermal solar wind (including >70 resolved ion charge states including H^{+}, $^{4}He^{2+}$, $^{4}He^{+}$, C^{1-6+}, O^{1-8+}, Ne^{1-10+}, Si^{6-12+}, Fe^{6-20+}) over an energy range extending from 0.5 to 100 keV/e. Its operation is identical to the Ulysses/SWICS and ACE/SWICS implementations, which have decades of successful flight operations. The geometry factor of SPICES is significantly larger than Solar Orbiter Heavy Ion Sensor (HIS), enabling observation of kinetic behavior down to 1 s for heavy ions (720× faster than SWICS, 4× faster than HIS burst mode). This unprecedented time resolution of heavy ion composition is necessary to reveal mesoscale variability in the heating and acceleration of particles in the heliosphere.

The Electrostatic Analyzer (ESA) consists of 17 identical side-by-side deflection channels, each with one ground and one high-voltage metal deflection plate. A thin insulating gap separates adjacent pairs of ground and high-voltage plates. The curved electrodes select particles based on mass, charge, and velocity; a technique common

in ESA-based instrumentation. Ions that fall within a pass-band (<10% of the E/q corresponding to a given voltage step) pass through the ESA without hitting the walls. All modules are logarithmically stepped over their full energy range.

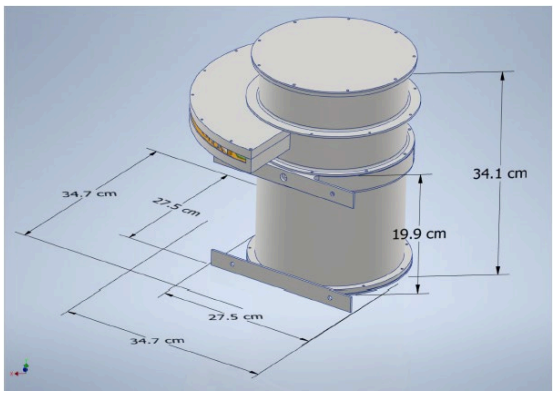

Exhibit C-3. *Schematic of the InterMeso SPICES instrument,* currently under NASA-funded development to TRL 6 by September 2022.

The ToF-E section, located behind the ESAs, is housed inside the cylindrically shaped high voltage bubble, which is separated from all ground surfaces. This ToF-E consists of four rectangular thin-window low-noise SSDs, a 1–2 μg/cm^2 grid-supported carbon foil, start and stop chevron microchannel plate (MCP) assemblies and secondary electron steering plates. A post-acceleration region is located between the ESA entrance system and the ToF section, which is maintained at a potential of −50 keV. As such, ions that successfully pass through the ESA gain kinetic energy proportional to their charge and impact a thin carbon foil, where they experience mass-dependent angular scattering and energy loss (1–5 keV). The post-acceleration region ensures incident ions experience minimal relative energy loss in the carbon foil, have energies larger than the solid-state detector (SSD) low-energy threshold, and that low charge state ions and isotopes (e.g., ^{3}He, ^{4}He, ^{22}Ne, ^{20}Ne) can be effectively resolved. A schematic of SPICES is shown in **Exhibit C-3** with instrument specifications in **Exhibit C-4**.

The components of SPICES have substantial heritage on Ulysses/SWICS, ACE/SWICS, and Solar Orbiter/HIS with most components at or above TRL 6. The HVPS is currently being developed under NASA contract 80GSFC20C0052 to be TRL 6 by the end of the 2022 fiscal year and putting the instrument at a PDR stage of development by September 2022. *No additional investment would be required prior to Phase A.*

Item	Value
Size/dimensions	0.35 × 0.35 × 0.54 m
Instrument mass (CBE)	13.14 kg
Instrument average payload (CBE)	24.17 W
Instrument science data rates (CBE)	1.5 kbps (survey) 15 kbps (burst)
Instrument Fields of View	Elevation: −4° to 4° Azimuth: −30° to 80°
Pointing requirements (knowledge)	<0.5°
Pointing requirements (control)	Few degrees
Pointing requirements (stability)	n/a

Exhibit C-4. *InterMeso SPICES specifications.*

SIS-Lo

The Suprathermal Ion Spectrometer-Lo (SIS-Lo; shown in **Exhibit C-5**) enables lower-energy suprathermal ions (1.5–200 keV/e) charge and mass separation. *These measurements, coupled with the measurements from SPICES and SIS-Hi, are critical in allowing InterMeso to understand the mesoscale variability of particle acceleration and source populations.* SIS-Lo leverages heritage from ACE/ULEIS and Solar Orbiter/SIS. The specifications of SIS-Lo are provided in **Exhibit C-6**.

Employing two independent electrostatic analyzers (ESAs), SIS-Lo is capable of achieving measurements over the entire suprathermal energy range at high cadences and high-energy resolution with ionization-state determination. One part of the SIS-Lo ESA is a conventional equal-distance, curved analyzer covering the energy range from 1.5 to 10 keV/e with ten logarithmic steps and an energy resolution of ~7%. The relatively narrow energy range that this ESA covers allows the geometry factor to be optimized for maximum sensitivity while still distinguishing the pickup ion distribution from the solar wind high-energy tail. For higher energy suprathermal ions, SIS-Lo uses a separate, dispersive ESA to cover the energy range from 10 to 200 keV/e. This innovative dispersive ESA is fully tested (TRL 6). It has an unusual shape (wide opening and exit apertures with a narrow gap in the middle) that allows ions in a large E/q range and FOV to be measured

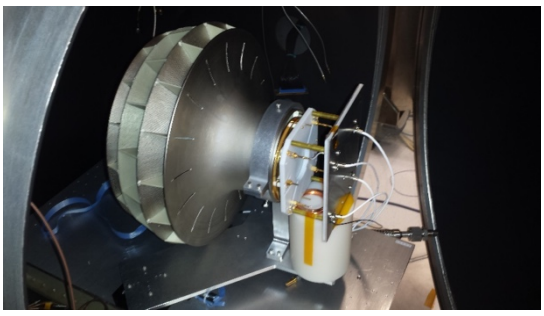

Exhibit C-5. *Photo of the SIS-Lo prototype,* currently TRL 6.

simultaneously with a single voltage setting. Upon exiting the analyzer, the ion passes through a collimator, is post-accelerated by ~12 kV, and enters the ToF chamber. The voltage setting on the analyzer, collimation of allowed trajectories, and exit location on the ESA identifies each ion's E/q and incident angle. The traditional, equal-distance, curved plate ESA occupies the inner annulus of the ToF chamber's aperture, while the dispersive ESA utilizes the outer annulus. Placement of SIS-Lo such that the nominal parker spiral is within its FOV allows the instrument to measure suprathermal particles leaving the Sun with additional detail on particle anisotropy.

Item	Value
Size/dimensions	0.48 × 0.25 × 0.23 m
Instrument mass (CBE)	3.7 kg
Instrument average payload (CBE)	0.8 W
Instrument science data rates (CBE)	0.7 kbps
Instrument Fields of View	360° × 60°
Pointing requirements (knowledge)	<1°
Pointing requirements (control)	Few degrees
Pointing requirements (stability)	n/a

Exhibit C-6. *InterMeso SIS-Lo specifications.*

Laboratory measurements by *Allegrini et al.* (2016) demonstrated the dispersive ESA with ToF chamber is able to resolve H^+, He^+, N^+, and O^+. Each ESA has its own set of voltage plates (ground, high voltage) that is serrated and coated to attenuate ultraviolet reflection. The SIS-Lo ToF chamber is based on the ACE/ULEIS and Solar Orbiter/SIS instruments and operates with a pre-acceleration voltage of −12 kV, enough for the ions to penetrate the 1 mg/cm^2 carbon foils with minimal scattering. An additional −13 kV of post-acceleration is placed on the junction of the SSDs, providing a total acceleration of −25 kV, sufficient for detection of >2 keV ions in the SSD. Secondary electrons (e-) emitted when the ion passes through the entrance and detector-foils are accelerated to ~1 kV and directed via isochronous electrostatic-mirrors onto MCP Z-stacks. Fast signals from the MCPs provide "start" and "stop" signals. In addition, the positions of the incident ion at the entrance and detector-foils are fully preserved by the electrostatic-mirror and measured by MCP position anodes; these data are then used to resolve the ion's E/q, incident angle, and corrected exact ToF path. The SSD measures the residual energy (E') of the ion. The energy per charge (E/q), energy (E'), ToF (τ), and corrected flight path in the telescope are combined to give the particle mass (m and q), which has been successfully demonstrated in multiple missions, including the SWICS instruments on Ulysses, ACE, and Wind. Each of the components of SIS-Lo are at or above TRL 6 with the instrument being at TRL 6.

SIS-Hi

The SIS-Hi instrument measures higher energy suprathermal ions from 50 keV/nucleon to energetic ions at 10 MeV/nucleon with a large FOV and geometry factor (24 cm^2-sr; *20× increase from ACE/ULEIS*) to characterize the quiet-time suprathermal ion distribution at high enough cadence to satisfy the STM (**Exhibit 1-12**). SIS-Hi is a ToF-E telescope modeled after Solar Orbiter/SIS and ACE/ULIES. Similar to the method used in the SIS-Lo ToF chamber, the combination of ToF and residual energy (E') allows for the accurate determination of the particles mass. However, unlike SIS-Lo, the instrument does not have an ESA, and as such can determine mass to high accuracy but is unable to resolve charge states. Additionally, SIS-Hi consists of only two MCPs and one SSD, allowing for only a single ToF to be measured. *SIS-Hi is fully optimized to make high time resolution observations of mesoscale variabilities in the quite time populations as well as to investigate mesoscale changes in accelerated ions at solar wind transients.* SIS-Hi, an enlarged version of a single Solar Orbiter/SIS ToF chamber (prototypes shown in **Exhibit C-7**, with instrument specifications shown in **Exhibit C-8**), has been prototyped and tested to TRL 6.

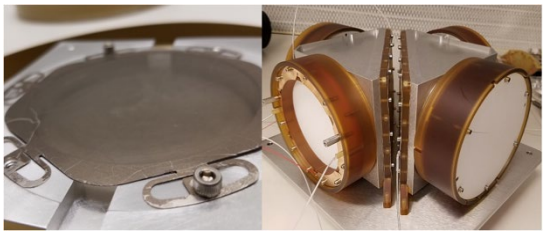

Exhibit C-7. *Photos of SIS-Hi prototype components, currently TRL 6.*

Item	Value
Size/dimensions	0.45 × 0.25 × 0.21 m
Instrument mass (CBE)	2.4 kg
Instrument average payload (CBE)	0.4 W
Instrument science data rates (CBE)	0.5 kbps
Instrument Fields of View	68° cone
Pointing requirements (knowledge)	<1°
Pointing requirements (control)	Few degrees
Pointing requirements (stability)	n/a

Exhibit C-8. *InterMeso SIS-Hi specifications.*

SPAN-E

InterMeso is equipped with two ESA-based low-energy electron sensors based on SPAN-B from PSP (i.e., the SPAN-E sensor on the anti-ram side of PSP, *Whittlesey et al.*, 2020; *Kasper et al.*, 2016). The ESAs allow only a set energy window of electrons to reach the back-end MCPs, allowing for the determination of differential flux. Each SPAN-E has a FOV of 240° × 120°. Similar as to on PSP, the combination of both SPAN-E sensors, placed on opposite sides of the spacecraft, allow for most of the sky with the exception of blockages from the spacecraft (e.g., solar panels). The combined SPAN-E sensors are able to measure the 3D VDF of electrons from 2 eV to 30 keV, capturing the core, halo, and strahl populations. *These observations are critical for determining mesoscale variations in solar wind structures and transients.*

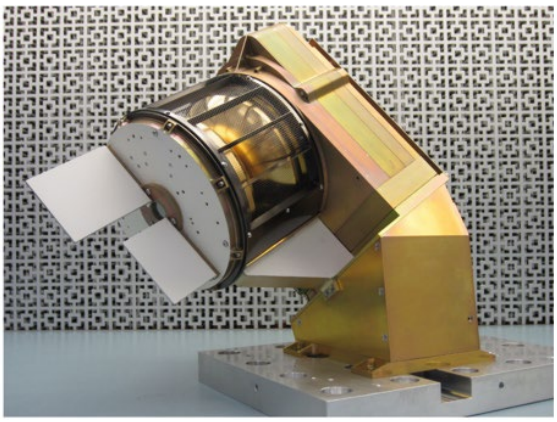

Exhibit C-9. *Photo of the PSP SPAN-B instrument, which is a single SPAN-E telescope. InterMeso will fly an exact copy of this proven technology,* currently TRL 9.

While the effective energy floor can be affected by spacecraft charging, initial spacecraft potential simulations have shown this effect, after mitigation efforts, to be small enough to not impact the science of InterMeso (see **Section 3.2.8**). Heritage for SPAN-E includes PSP, MAVEN, HERMES, Wind, FAST, THEMIS. As this is an exact copy of SPAN-B, a single SPAN-E telescope assembly, currently operating on PSP (shown in **Exhibit C-9** with instrument specifications in **Exhibit C-10**), the *TRL of the instrument is 9*.

Item	Value
Unites	2
Size/dimensions	0.17 × 0.15 × 0.13 m
Instrument mass (CBE)	2.4 kg
Instrument average payload (CBE)	2.2 W
Instrument science data rates (CBE)	2.5 kbps
Instrument Fields of View	240* × 120°
Pointing requirements (knowledge)	<1°
Pointing requirements (control)	Few degrees
Pointing requirements (stability)	n/a

Exhibit C-10. *InterMeso SPAN-E specifications.*

MEPS

The Medium Energy Particle Spectrometer (MEPS) was chosen as the candidate instrument to measure the energetic electron (25–500 keV) and total energetic ion content (30 keV/nuc to 8 MeV/nuc). *High time resolution energetic electrons allow for precise determinations of acceleration injection times and path-length calculations using FVDA analysis and the different look directions allow for investigations of electrons reflected off interplanetary structures* (see **Section 1**).

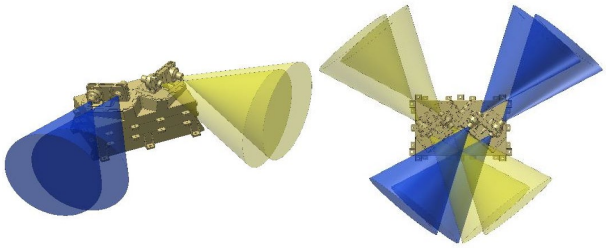

Exhibit C-11. *Schematics of MEPS with the 8 FOVs shown. With heritage drawing from instruments such as Solar Orbiter EPT, this instrument is* currently TRL 6.

Item	Value
Size/dimensions	0.30 × 0.20 × 0.20 m
Instrument mass (CBE)	4.8 kg
Instrument average payload (CBE)	10.0 W
Instrument science data rates (CBE)	0.7 kbps (survey) 10 kbps (burst)
Instrument Fields of View	8 double FOVs with a 45° full angle
Pointing requirements (knowledge)	<2°
Pointing requirements (control)	Few degrees
Pointing requirements (stability)	n/a

Exhibit C-12. *InterMeso MEPS specifications.*

MEPS is a double-ended telescope based on Solar Orbiter/EPT with one side using a polymide layer to stop ions while allowing electrons through, and the other side using permanent magnets to deflect away the electrons but allowing energetic ions to pass unaffected. The MEPS instrument combines the two units of Solar Orbiter/EPT into one unit for simplicity. The positioning of MEPS on the spacecraft is such that two of the FOVs are centered along or opposed to the direction of the nominal parker spiral with the other two FOVs offset 90° (shown in **Exhibit C-11**). The four FOVs allow for measurements of the energetic particle anisotropy during SEP events both sunward versus anti-sunward as well as transverse to the nominal IMF. MEPS

has heritage from SOHO/ERNE, STEREO/SEPT, and Solar Orbiter/EPT. Instrument specifications for MEPS are shown in **Exhibit C-12**. While most of the components of MEPS are 8–9, the TRL of the full instrument is 6.

Fluxgate Magnetometer (FGM)

High-precision magnetic field measurements are critical for understanding the nature of the mesoscale solar wind and transients and provide vital context for plasma and energetic particle dynamics. The magnetic field sensors on InterMeso are two tri-axial fluxgate magnetometers that measure the DC vector magnetic field and low-frequency magnetic field wave modes. FGM is based off the PSP-FIELDS/MAG (*Bale et al.*, 2016) and the STEREO-IMPACT/MAG "conventional" three-axis fluxgate sensors (*Acuña et al.*, 2008; shown in **Exhibit C-13**), a part of a long-standing heritage of tri-axial ring-core fluxgate magnetometers (e.g., *Acuña*, 2002; *Acuña et al.*, 1992; *Lohr et al.*, 1997; *Anderson et al.*, 2007; *Kletzing et al.*, 2013). These sensors consist of three orthogonal ring-cores for sensing the vector field, and, in the case of PSP-MAG and STEREO-MAG, use analog signal processing electronics.

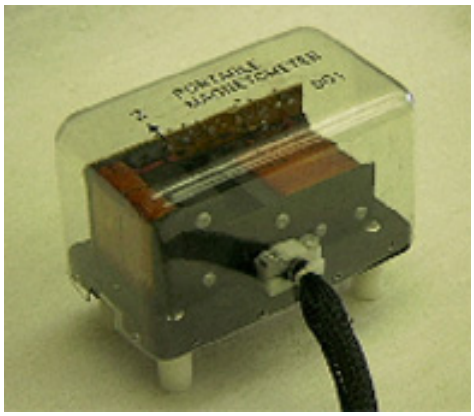

Exhibit C-13. *Heritage fluxgate magnetometer from STEREO.* The InterMeso FGM-boom assembly is currently TRL 8.

On each InterMeso spacecraft, the two identical fluxgate sensors of FGM are placed on a 4.5-m deployable boom, one at 2.5 m away from the spacecraft, and the other at the end of the boom. This follows a widely used inboard-outboard configuration design that allows for one-dimensional gradiometry corrections of spacecraft-generated magnetic field contamination signals (e.g., *Ness et al.*, 1971). The InterMeso FGM boom is based on the PSP-FIELDS/MAG boom design, but slightly lengthened to allow for additional magnetic cleanliness. This 4.5-m boom is a carbon composite rigid boom placed on the anti-sunward face of the spacecraft, deployed via a shoulder hinge at the spacecraft and a single-joint hinge at approximately half the length of the fully deployed boom. The TRL of this instrument is assessed as 8, primarily due to the lengthening of the boom to accommodate cleaner magnetic measurements. Instrument specifications are provided in **Exhibit C-14**.

Item	Value
Units	2
Size/dimensions	0.15 × 0.12 × 0.09 m
Instrument mass (CBE)	1.49 kg (both units + electronics) 6.27 kg (4.5-m boom)
Instrument average payload (CBE)	2.49 W (per unit)
Instrument science data rates (CBE)	1.3 kbps (survey – per unit) 8 kbps (burst – per unit)
Pointing requirements (knowledge)	<0.5°
Pointing requirements (control)	n/a
Pointing requirements (stability)	n/a

Exhibit C-14. *InterMeso FGM specifications.*

Electric Fields Antennas

The InterMeso Electric Fields Antennas are based on STEREO SWAVES (*Bougeret et al.*, 2008) and were baselined to provide radio and Langmuir wave observations. *Electric field and radio waves are required for mesoscale variations in connectivity of the spacecraft to particle acceleration sites.* This instrument, shown in **Exhibit C-15**, is composed of three 6-m beryllium-copper stacer monopole antennae. The 6-m length allows effects of sidelobes and phase perturbations near quarter-wave resonance to be above of the frequency bands of interest in the solar wind at 1 au (c.f., *Bale et al.*, 2008; *Bougeret et al.*, 2008).

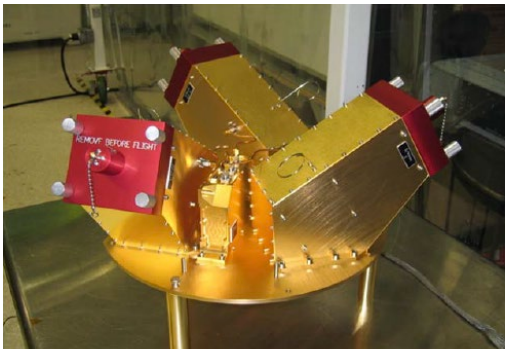

Exhibit C-15. *Electric field stacers from STEREO/WAVES.* The InterMeso electric field antennas are currently TRL 7.

The lower frequency range of the electric field measurements (~10 Hz to 200 kHz) is used to detect the ambient plasma density via quasi-thermal noise measurements and Langmuir waves driven by electron beams passing over the spacecraft. Sampling this frequency range with spectral and peak detection data at 0.5-s

cadence enables observation of ~200-km structures. The higher frequency range (~10 kHz to 20 MHz) of electric field measurement consists of spectral and cross-spectral data (~160 freq. bins, 0.25-s cadence) to identify particle acceleration event start times and determine electron beam trajectories through the heliosphere. Instrument specifications are provided in **Exhibit C-16**. Based on substantial overlap with STEREO/WAVES, the TRL of this instrument is 7.

Item	Value
Units	3
Size/dimensions	6 m antenna deployed (×3), 0.27 × 0.22 × 0.17 m (DPU)
Instrument mass (CBE)	7.53 kg (total) 12.37 kg (DPU & harness, shared with B-field)
Instrument average payload (CBE)	10.54 W (total)
Instrument science data rates (CBE)	6.6 kbps (survey, total) 26.3 kbps (burst, total)
Pointing requirements (knowledge)	<0.5°
Pointing requirements (control)	n/a
Pointing requirements (stability)	n/a

Exhibit C-16. *InterMeso E-Fields instrument specifications.*

STIX

The Spectrometer/Telescope for Imaging X-rays (STIX) from Solar Orbiter, shown in **Exhibit C-17**, is baselined for a single InterMeso spacecraft to provide solar flare associated X-ray observations. Bremsstrahlung radiation is produced in the X-ray range as solar-flare-accelerated energetic electrons decelerate in the solar corona due to coronal protons encounters. As such, *STIX will provide precise timing and initial electron spectra for solar energetic electrons*, which will be compared against mesoscale variability observed by the in situ instrumentation. STIX has an energy range from 4 to 150 keV, providing information on the tail of the flare-accelerated electron distribution. The use of non-focusing grid techniques (e.g., *Hurford*, 2013) allows STIX to minimize its mass and volume requirements (*Krucker et al.*, 2020).

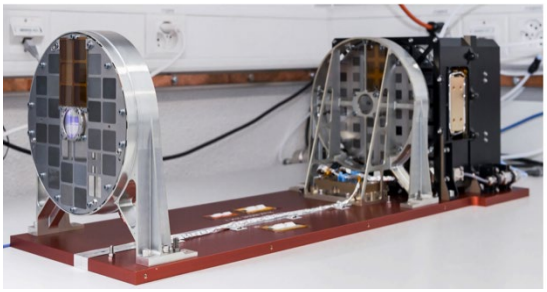

Exhibit C-17. *Photo of Solar Orbiter STIX.* The InterMeso STIX is currently TRL 8.

Only one of the InterMeso spacecraft is outfitted with a STIX instrument as the spacecraft separation is not likely to result in significant variations of X-ray observations. The other three spacecraft are fitted with a mass simulator. A student payload instrument could be considered as an alternative but was not evaluated for this study. To optimize the resolution of Solar Orbiter STIX at 1 au, the separation between the two optical grids has been increased to 1 m (was 0.55 m), but otherwise the instrument is an exact copy of Solar Orbiter STIX. As such, the InterMeso STIX is TRL 8. Instrument specifications are provided in **Exhibit C-18**.

Item	Value
Size/dimensions	1.35 × 0.30 × 0.30 m
Instrument mass (CBE)	7.0 kg
Instrument average payload (CBE)	7.0 W
Instrument science data rates (CBE)	0.1 kbps (survey) 5 kbps (burst)
Instrument Fields of View	1° × 1°
Pointing requirements (knowledge)	<0.25°
Pointing requirements (control)	0.25°
Pointing requirements (stability)	5 arcsec over a 10-s interval

Exhibit C-18. *InterMeso STIX specifications.*

Appendix D: Supplemental Mission Design and Navigation Information

Mission Design Requirements

InterMeso requires four spacecraft inserted into Earth-trailing orbits in the ecliptic plane. Each spacecraft features a unique Earth-relative drift rate allowing the constellation to spread out over time, *enabling measurements across the critical ranges of mesoscale variabilities*. The Mission Design was driven by both a desire to have a slow constellation drift from Earth for robust downlink margins and an end of mission separation between the first and last spacecraft in the constellation of at least 7°. **Exhibit D-1** shows the angle of separation between the Earth and each individual spacecraft (left) and the inter-spacecraft separation between the first and nth spacecraft (right) for the commissioning, primary, and potential extended mission. The extended mission values assume no additional maneuvering after the initial drifts are set at the beginning of mission.

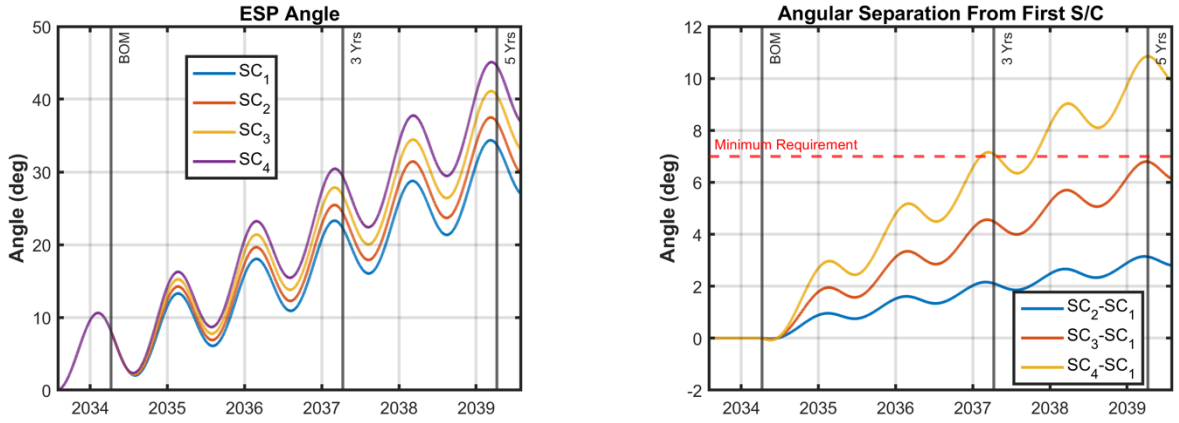

Exhibit D-1. *Earth–Sun–Probe angle for each spacecraft (left) and the relative separation between the first spacecraft and the remaining three over the course of the mission (right).*

As seen in **Exhibit D-1** (left), and similar to the STEREO orbits, the slight eccentricity of the orbits around the Sun lead to the spacecraft to, at times, have a retrograde orbit with respect to Earth. This can result in significant third-body perturbations when the spacecraft make their closest approach to Earth. The primary effect of these perturbations is an increase to the drift rate with respect to Earth. This effect decreases as the mission progresses and the spacecraft get farther from Earth. The inter-spacecraft range stays evenly distributed throughout the mission with a relative solar range between spacecraft less than 0.01 au, enabling more accurate investigations of mesoscale longitudinal variability by minimizing radial evolution.

Navigation

The baseline tracking schedule during the science orbit for orbit determination purposes is one 5.5-hour pass of two-way coherent Doppler measurements per week, utilizing the DSN 34-m antennas. Approximately one in three passes is done from the Southern Hemisphere to give geographic diversity. This provides a spacecraft position reconstructed uncertainty of ~900-km 3σ of each spacecraft in the science orbit. This can be improved to 120-km 3σ with the addition of sequential ranging data during one pass per month, however this is not required to meet science requirements. **Exhibit D-2** gives the representative 3σ reconstructed orbit position uncertainty in the radial (pos_r), in-track (pos_I), and cross-track (pos_c) directions during the science orbit. This is sufficient to meet the science requirement of 1000 km of position uncertainty.

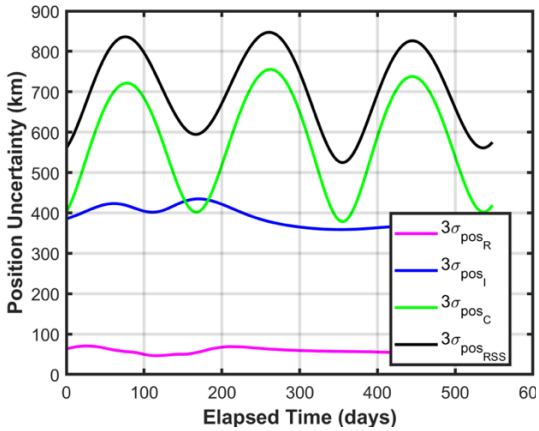

Exhibit D-2. *Reconstructed orbit determination uncertainty in radial, in-track, and cross-track directions along with the residual sum of squares (RSS) during the science orbit.*

Appendix E: Supplemental Cost Estimate Information

Ground Rules and Assumptions

The InterMeso cost estimate is generated consistent with the Solar and Space Physics (Heliophysics) Decadal Study and NASA Heliophysics Mission Concept Study guidance. Key ground rules and mission assumptions include the following:

- Estimates and budgets are presented in fiscal year 2022 (FY22) dollars. Adjustments to prior year costs and prices are based on the 2021 NASA New Start Inflation Indices (NNSII).
- The mission's implementing organization is unspecified. Cost estimates assume that NASA will competitively select a contractor with experience delivering multiple spacecraft and integrating instruments from multiple organizations.
- The mission assumes a Class-C risk classification, consistent with previous STP-line missions.
- No technology development activities are required before the start of InterMeso implementation. All components and elements are at or above TRL 6 with the exception is the Thermal Ion Composition instrument high-voltage power supply (HVPS). NASA is currently funding development of an HVPS Engineering Model and associated testing under contract 80GSFC20C0052, which is on track for delivery in September 2022.
- Commercial off-the-shelf (COTS) components needed for spacecraft propulsion, RF, avionics, and guidance and control subsystems are assumed to be available at the start of InterMeso implementation. COTS parts with equivalent performance and price are assumed to be available if currently identified components become obsolescent.
- NASA Science Mission Directorate will provide the implementing organization a 9-month Phase-A budget to cover planning and early engineering development activities.
- Unallocated cost reserves of 50% are added to the Phase B–D cost estimate excluding Launch Vehicles and Services and 25% reserves are added to the Phase E estimate.
- The InterMeso mission requires four identical spacecraft with near-identical instrument flight suites. Four instrument flight units each will be delivered at 3-month intervals for integration to each of the four spacecraft. All instrument deliveries are completed before spacecraft integration starts with the following exceptions:
    - Only one Hard X-ray Imager is required for the mission. The three other spacecraft will include a mass simulator in place of an Imager.
    - Two copies of the Low-Energy Electron instrument are required for each spacecraft. Pairs of those instruments will be delivered every 3 months.
    - Pairs of fluxgate magnetometers (FGMs) together with one boom and DPU (Digital Processing Unit) are delivered for integration every 3 months.
- The first two InterMeso spacecraft are assembled and integrated simultaneously, with harness installation as the pacing activity. After assembly and integration, these spacecraft are treated as protoflight units and subjected to Full Environmental Testing. The second pair of spacecraft start assembly when the initial pair move to environmental testing (i.e., the second pair being integration one year after the start of the first, see **Appendix B**).
- Time from Phase B start to Launch Readiness Review (LRR) is approximately 8 years, including 3 years of System I&T and schedule margin. See **Section 4** and **Appendix B** for schedule details. After launch and 1 month of Phase D baseline checkout, the 43-month Phase E starts with up to 7 months for additional transit and commissioning followed by 36 months of prime mission science data collection.

- Launch of the four InterMeso spacecraft requires one Option 2 launch vehicle (LV) with a 5-m fairing. Option 2 is described in the Launch Vehicle Guidance. The implementing organization will cover the $700K costs of a single ESPA Grande spacecraft-to-LV adapter (or equivalent) and a C-22 adapter ring.
- Spacecraft provide dual Ka- and X-band telecommunications. Ka-band is used for downlinking science data and X-band for low-rate spacecraft bus telemetry and commanding. All ground communications are through the Deep Space Network (DSN). Estimated DSN charges are reported but not included in the InterMeso mission cost.

Estimating Copy Costs

InterMeso Phase B–D mission cost is primarily driven by the implementing organization's capability to deliver exact copies of subsystem and instrument assemblies on schedule and at budget. Cost assessments of the STEREO and VAP (Van Allen Probes) missions, for which APL delivered pairs of nearly identical spacecraft and instruments, resulted in cost data useful for estimating subsystem-level cost-to-copy (CtoC) factors (*Whitley et al.*, 2013). These estimates, presented in **Exhibit E-1**, assume that only recurring costs are incurred when delivering flight unit copies. The aggregate CtoC factor for a second spacecraft as a whole is 36%, equal to the CtoC factor estimated by the Team X at JPL (*Warfield and Roust*, 1998). Neither estimate assumes any discounts beyond the cost-to-copy savings realized between the first and second flight unit deliveries. Presumably additional savings will be realized as organizations build additional flight units past the first two. For example, *Whitley et al.* (2013) found additional cost savings between Juno Jupiter Energetic-Particle Detector Instrument (JEDI) and VAP RBSPICE from having a shared learning curve.

Subsystem	First-Unit Cost		Cost to Copy (2 Units)
	Nonrecurring	Recurring	
Guidance & Control	45%	56%	38%
Power, including PDU	63%	38%	23%
Harness	45%	55%	38%
Mechanical/Structural	57%	44%	28%
Thermal	42%	58%	41%
RF/Communications	45%	56%	38%
Command & Data Handling (IEM)	30%	71%	54%
Propulsion	47%	54%	37%
Flight Parts Qualification	45%	56%	38%
Flight Software (FSW)	100%	0%	0%
Aggregate (excl. FSW)	47%	53%	36%

Exhibit E-1. *Percentage of nonrecurring and recurring costs by subsystem, based on the median of the STEREO and VAP missions.*

Subsystems with relatively high design (nonrecurring) costs, including the Power and Mechanical/Structural subsystems, have lower CtoC factors while subsystems with relatively high production (recurring) costs, such as command and data handling (C&DH), have higher CtoC factors (**Exhibit E-1**). These historical percentages and CtoC factors are applied at the subsystem level to estimate the costs of the four spacecraft flight units (either in the case of SPAN-E and the magnetometers). For instruments, InterMeso cost estimates conservatively use the spacecraft aggregate 36% CtoC factor reported by both *Warfield and Roust* (1998) and *Whitley et al.* (2013).

Instrument Cost Details

Estimated instrument costs are shown in **Exhibit E-2**. The total estimated cost of the work breakdown structure (WBS) 05 element, which covers all instrument design work, engineering units, and flight units to be delivered for integration to a spacecraft, is $149.3 million (FY22). Note that WBS 05 also includes $11.7 million for the Implementing Organization for Instrument Management and Oversight derived from historical cost factors.

Two "first-unit" cost estimates were generated and averaged for each instrument on InterMeso. Estimates were generated with Version 9 of the system-level cost estimating equations of the NASA Instrument Cost Model (NICM9) and the Galorath SEER for Space costing framework. For the Thermal Ion Composition (SPICES) instrument, a component-level master equipment list (MEL) provided inputs to the NICM9 subsystem-level estimating equations and the TruePlanning costing framework. Uncertainty effects were estimated by including using CBE mass and power values as low parameters and MEV mass and power values as high parameters. The

predicted design life parameter was permitted to range from 44 months, the anticipated duration from launch to the end of Phase E, to 68 months to allow for a two-year extended mission option. A comparison of 70th-percentile estimates of the two models for the "first-unit" cost of each instrument is shown in the fourth and fifth columns of **Exhibit E-2**.

Results were cross-checked, where possible, against the costs of previous instrument builds. The SPICES instrument has the largest cost uncertainty. As the University of Michigan completes development of a TRL-6 high-voltage power supply board test unit for delivery to NASA by September 2022, before the release of the Solar and Space Physics (Heliophysics) decadal report, both the cost uncertainty and likely cost of SPICES should decline.

Instrument Description	Heritage Mission(s) (Start TRL)	Analogy Instrument(s)	First-Unit Estimates (70th percentile)		Total Baseline Estimated Cost	Notes
			NICM9	SEER for Space		
WBS 05. Instruments					$149.3	Baseline cost estimate
Instrument Management & Oversight					$11.7	Historical mission cost factor applied to total instrument estimated cost.
Bulk Solar Wind Plasma Instrument (Faraday Cup)	Europa Clipper (7)	PIMS	$6.0	$4.1	$11.3	Single Faraday cup per spacecraft Previous implementation required multiple Cups. Significant mass reduction due to lower radiation environment.
Thermal Ion Composition (SPICES)	ACE, Solar Orbiter, MESSENGER (6)	SWICS, HIS, FIPS	$23.5 (Subsystem)	$17.3 (TP)	$37.6	A unit with a new HVPS is being built now by U. Michigan. Subsystem-Level Model and TruePlanning (TP) framework used to estimate cost of this relatively large instrument. Appreciable volume and mass are from high-voltage standoff distances, rather than instrument complexity.
Suprathermal Ion Composition (SIS-Lo)	ACE, Solar Orbiter (6)	ULEIS, SIS	$4.9	$6.3	$12.5	Partial rebuild of SIS with the addition of a prototyped electrostatic analyzer.
Energetic Ion Composition (SIS-Hi)	ACE, Solar Orbiter (6)	ULEIS, SIS	$3.1	$2.2	$5.9	Partial rebuild of Solar Orbiter SIS with minor modifications.
Low-Energy Electron Distribution (SPAN-E) (2 per spacecraft)	PSP (9)	SPAN-E	$2.6	$1.8	$12.5	The SPAN-E copies are the only instrument that will start at TRL 9. Total cost is for 8 flight units, 2 per spacecraft.
Energetic Electron Distribution (MEPS)	Solar Orbiter, STEREO (6)	EPT SEPT	$6.2	$11.7	$18.2	Minor modifications will be made to heritage design.
Hard X-Ray Imager (STIX) (only 1 flight model required)	Solar Orbiter (8)	STIX	$6.5	$6.4	$6.4	Only 1 flight unit will be a rebuild of Solar Orbiter STIX.
Fluxgate Magnetometers (two per spacecraft) plus Boom (FGM)	PSP (8)	FGM (8)	$4.9	$5.4	$12.6	Build to print FGM with lengthened boom.
MAG/Electric Fields DPU & Harness	PSP (8)	Inst. DPU	---	$1.4	$2.7	Minor modifications will be made to heritage design to support both MAG and Electric Fields.
Electric Fields	STEREO (7)	WAVES	$9.6	$7.4	$18.0	Partial rebuild of STEREO WAVES.

Exhibit E-2. *Estimated instrument costs (in millions of FY22 dollars).*

Spacecraft Cost Details

The estimated total cost of all four spacecraft is presented in **Exhibit E-3**. The first spacecraft includes all nonrecurring costs and recurring costs. All other spacecraft estimates only include recurring costs. Recurring and nonrecurring costs by subsystem as a percentage of first-unit costs are shown in **Exhibit E-1**. Three hardware-subsystem-level cost estimates were generated as follows:

- The preliminary estimate is based on analysis of STEREO spacecraft cost history. This estimate is calculated by adding the estimated costs of two additional spacecraft to the reported cost of the STEREO spacecraft. This estimate includes STEREO FSW development cost. Historical cost-to-copy factors calculated from STEREO's cost history ensure that the costs of the third and fourth spacecraft include only recurring costs. This preliminary benchmark estimate exceeds the other estimates due to the large mass difference between the lighter InterMeso and more extensively outfitted STEREO spacecraft, presented in column 5 of **Exhibit E-3**. Overall InterMeso MEV mass is only about half that of STEREO with fewer instruments than STEREO. In addition, InterMeso utilizes less expensive software-based radios and single board computers, resulting in this estimate being highly conservative.
- The second estimate uses cost-per-kilogram factors derived from the two-spacecraft STEREO mission cost data. STEREO provides a starting point for InterMeso spacecraft estimation because it is a multi-spacecraft mission with two near-identical spacecraft. Subsystem-level estimates were calculated by multiplying cost-per-kilogram factors by the MEV subsystem masses. Much of the difference between the previous estimate and this cost-per-kilogram estimate is the reduced masses of the structure-and-mechanical and communications subsystems.
- The third estimate uses results from the Galorath SEER for Space model. SEER for Space enables spacecraft estimates at the subsystem level with probabilistic cost estimates. CBE values are used as low parametric inputs and MEV values as high inputs. The model then calculates a four spacecraft cost based on the breakout of Design and Production costs and a 95% learning curve.

Hardware Development (Nonrecurring) and Production (Recurring) cost estimates are calculated as the average of the STEREO actuals and SEER-Space estimates. The $15.429 million (FY22) estimated cost of flight software (FSW) resulted from a detailed estimate based on InterMeso FSW, testbed software, and autonomy rules requirements after accounting for existing APL software and reusable code.

Exhibit E-3 shows the details of the spacecraft cost estimate. Column 8 shows that the recurring cost of the first flight unit is $31.5 million. That estimate is within a few percent of STEREO recurring actuals for one spacecraft (column 5) and the SEER for Space estimate (column 7). Only Guidance & Control, Communications, and C&DH show significant differences between actuals and estimates. STEREO's lower C&DH estimate would be closer to the other estimates if flight parts qualification costs were allocated to the appropriate subsystems.

The cost of the first InterMeso spacecraft flight unit, shown in column 9 of **Exhibit E-3**, is $110.5 million (FY22) with $95.1 million for hardware and $15.4 million for FSW. The most expensive subsystems are Power at $21.8 million, C&DH at $15.3 million, and Communications at $14.9 million. The cost of the Mechanical and Structures subsystem is $10.3 million, or more than 10% of the cost of the first flight unit hardware, consistent with previous APL spacecraft builds. Column 10 adds the recurring costs for three additional spacecraft to that of the first flight unit for a total four-spacecraft cost of $205.1 million (FY22).

As a cross-check, MMS Launch CADRe data was used to calculate cost-per-kilogram factors for spacecraft bus subsystems that corresponded to those for InterMeso. Factor development assumed that almost all MMS avionics costs were nonrecurring engineering (NRE) for C&DH development and that dollars spent prior to Phase D were NRE/Development. While the latter is an assumption that overstates development expenditures and results in an underestimate of Recurring/Production costs, more accurate pre-removal of non-standard MMS mechanical-and-structural costs (such as for a launch vehicle adapter development and production) from the analysis would lower the relevant cost-per-kilogram. The InterMeso spacecraft estimate that resulted using MEV inputs and the MMS cost-per-kilogram factors was $234.4 million (FY22), or about 14% higher the presented estimates. More-detailed selection of MMS costs to include in the cost-per-kilogram analysis would reduce the difference between the InterMeso estimate and the MMS cross-check.

	NRE (Development) Cost			Recurring Cost: First Flight Unit Only				Total Est. Cost	
Subsystem [1]	STEREO [2]	SEER for Space [3]	Est. Cost [4]	STEREO Cost [5]	STEREO (Mass Adjusted) [6]	SEER for Space [7]	Est. Cost [8]	First Flight Unit [9]	Four Flight Units [10]
Total Estimated Cost	**$61,211**	**$89,171**	**$79,014**	**$33,347**	**$25,755**	**$32,463**	**$31,524**	**$110,538**	**$205,110**
Spacecraft Hardware	***$48,406***	***$73,742***	***$63,585***	***$33,347***	***$25,755***	***$32,463***	***$31,524***	***$95,109***	***$189,681***
Guidance & Control	$5,441	$6,763	$6,102	$6,336	$45,835	$8,765	$6,979	$13,081	$34,017
Power, including PDU	$13,034	$19,110	$16,072	$5,957	$4,991	$6,357	$5,769	$21,840	$39,146
Harness	$1,174	$2,385	$1,779	$1,610	$998	$917	$1,175	$2,954	$6,479
Mechanical/Structural	$4,875	$9,539	$7,207	$3,742	$1,804	$3,667	$3,071	$10,279	$19,492
Thermal	$1,122	$4,291	$2,706	$858	$725	$1,522	$1,035	$3,741	$6,846
RF/Communications	$5,802	$11,450	$8,626	$8,367	$6,274	$4,123	$6,255	$14,881	$33,646
C&DH (IEM)	$8,620	$13,995	$11,307	$3,114	$3,871	$5,040	$4,008	$15,316	$27,341
Propulsion	$3,315	$6,209	$4,762	$1,858	$1,257	$2,071	$1,728	$6,491	$11,676
Flight Parts Qualification	$5,023		$5,023	$1,504			$1,504	$6,526	$11,038
Flight Software (FSW)	***$12,805***	***$15,429***	***$15,429***					***$15,429***	***$15,429***

Exhibit E-3. *Estimated costs of four InterMeso spacecraft (in millions of FY22 dollars).*

Mission Operations

Phase B–D mission operations costs were estimated by starting with actual STEREO mission costs reported in the Launch CADRe, inflating them to FY22 dollars, and then adding the cost of additional Mission Operations staff members required to support planning, checkout, and initial operations of the additional two spacecraft.

System Integration and Testing (SI&T) Cost

Initial SI&T estimates were generated by extrapolating STEREO and VAP SI&T costs from two to four spacecraft. The cost factor was then bolstered to account for additional GSE and facilities, as well as simultaneous SI&T activity on all four spacecraft (using the pair system outlined in **Section 4.2**). The estimated cost of $61.8 million is 17.4% of the estimated costs of Instruments and Spacecraft. It is also within 10% of the $66.1 million spend on more complex MMS SI&T.

Cost Confidence and Risk

A Monte Carlo risk analysis was conducted to assess the adequacy of unallocated reserves to achieving mission cost. Statistical variance is primarily driven by cost and schedule uncertainties associated with delivering multiple flight units. Hardware and software designs with substantial heritage present relatively fewer than normal technical risks. For example, while spacecraft harnesses tend to be low risk technically, the InterMeso spacecraft harness is assigned a medium risk value because of the possibility that spacecraft and instrument deliveries are assigned to organizations without multiple spacecraft build expertise, allowing for a conservative estimate of the InterMeso cost confidence.

Probability distributions were assigned to each instrument and spacecraft subsystem as well as to non-hardware level-2 WBS elements. Instruments with long heritage and/or recent flight builds, i.e., the Faraday cup, SIS-Lo, SIS-Hi, SPAN-E, MEPS, FGM, electric fields, and STIX, were assigned low risk. The Thermal Ion Composition instrument (SPICES) is the highest risk instrument, due to the instrument's HVPS being currently developed for delivery to NASA in September 2022, and is assigned a medium-to-high risk value. All spacecraft subsystems and SI&T were assigned medium risk.

The Phase A–D Monte Carlo results are shown in **Exhibit E-4** as a cumulative ascending probability distribution, or "S curve." The curve shows the $753 million baseline estimated cost (without reserves) falling at the 34th percentile–in other words, that Phase A–D cost expenditures would not exceed the baseline about one-third of the time. The baseline cost estimate with required cost reserves falls at the 67th percentile. *Knowledge that*

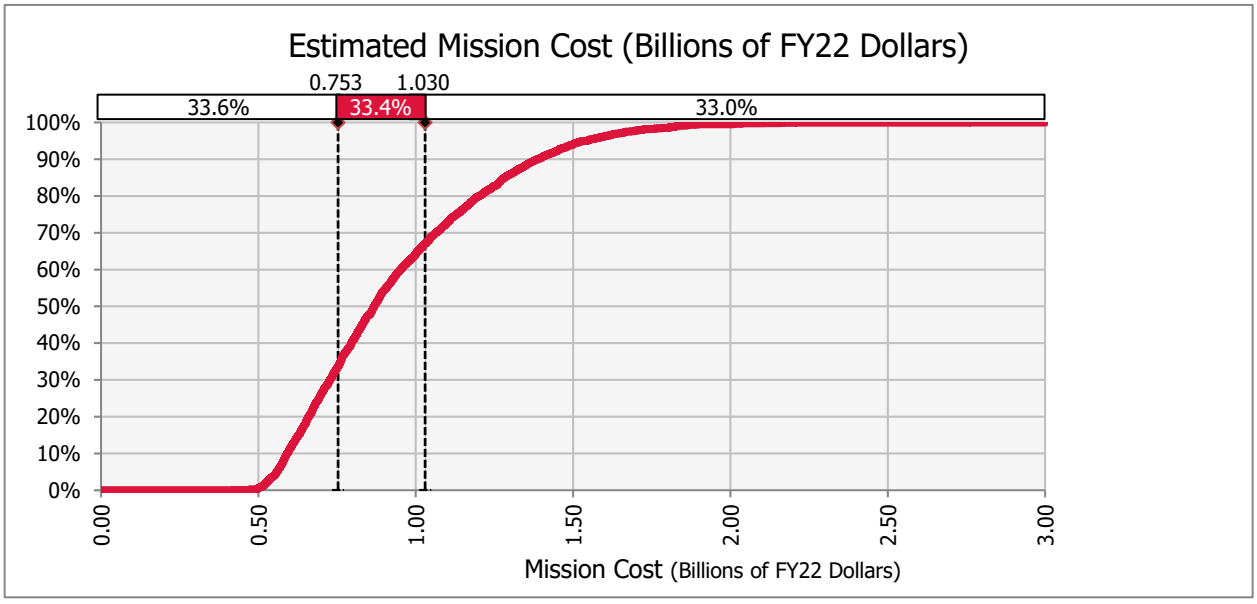

Exhibit E-4. *Monte Carlo results of mission cost (in billions of FY22 dollars).*

the mission would be implemented by organizations experienced with multiple spacecraft builds would raise confidence above the 70th percentile.

System I&T presents the highest risk to schedule and cost. Delays in unit delivery can create test facility bottlenecks and anomalies can lead to the retest of multiple units across the all the spacecraft. Higher cost risk is also assigned to WBS 05 instruments as implementers may lack experience in the delivery of this many flight units. Phase B–D Cost growth for APL's two dual-spacecraft missions, STEREO and VAP, is presented in **Exhibit E-5**.

Subsystem Cost Growth in Dual-Spacecraft APL Missions, Phases B–D			
	STEREO	**VAP**	**Average for Two-Spacecraft Builds**
Structures & Mechanisms	155%	5%	80%
Thermal Control	82%	−23%	30%
Electrical Power	49%	24%	37%
PDU (Power Distribution Unit)	155%	15%	85%
Harness	314%	42%	178%
GN&C	23%	−18%	2%
Propulsion	24%	11%	17%
Communications	27%	60%	43%
C&DH	22%	30%	26%
Software	45%	13%	29%
Total	**39%**	**23%**	**31%**

Exhibit E-5. *Spacecraft subsystem cost growth from start of Phase B to end of Phase D for multi-spacecraft STEREO and VAP missions.*

The average aggregate reserve expenditure for the two-spacecraft missions was 31%. Percentage wise, the highest average reserve expenditure across the two mission was associated with Structures & Mechanisms, Harness, and Communications. The relatively better reserve expenditure performance on the VAP mission, launched in August 2012, compared to STEREO, launched in October 2006, suggests benefit in selecting an Implementing Organization that has already built multi-spacecraft missions. Only the VAP Communications and C&DH subsystems experience a higher percent reserve expenditure than their corresponding STEREO subsystems. All VAP reserve expenditure was less than 30% with the exception of Harness and Communications. STEREO and VAP performance data implies that InterMeso spacecraft reserve expenditure risk is likely to be consistent with a medium rating.

As for instruments, a CADRe comparison (in Real Year dollars) of the predicted costs at PDR and actual costs post launch finds that the average aggregate reserve expenditure of the STEREO instrument pairs was 38%. Higher percentage growth was associated with the lower cost instruments. The PDR-Post Launch reserve expenditure of SWAVES, precursor of the InterMeso electric fields instrument, was only 18%.

Anticipating that the InterMeso concept will not evolve radically, it seems likely that Phase B–D reserve expenditure is unlikely to exceed the 50% observed by Aerospace in its cost-to-go analyses of NASA robotic space missions. *That implies that a baseline InterMeso mission with 50% unallocated cost reserves assigned to Phases B–D, has a high probability of success.*

References

Ala-Lahti, M., J. Ruohotie, S. Good, E. K. J. Kilpua & N. Lugaz (2020) Spatial coherence of interplanetary coronal mass ejection sheaths at 1 AU, *J. Geophys. Res. Space Physics*, 125, e2020JA028002, doi: 10.1029/2020JA028002.

Acuña, M. H., J. E. P. Connerney, P. Wasilewski, R. P. Lin, K. A. Anderson, et al. (1992) Mars Observer Magnetic Fields Investigation, *J. Geophys. Res.*, 97 (E5), 7799– 7814, doi: 10.1029/92JE00344.

Acuña, M. H. (2002) Space-based Magnetometers, *Review of Scientific Instruments*, 73, 3717, doi: 10.1063/1.1510570.

Acuña, M. H., D. Curtis, J. L. Scheifele, C. T. Russell, P. Schroeder, et al. (2008) The STEREO/IMPACT Magnetic Field Experiment, *Space Sci. Rev.*, 136, doi: 10.1007/s11214-007-9259-2.

Ala-Lahti, M., J. Ruohotie, S. Good, E. K. J. Kilpua, & N. Lugaz (2020) Spatial coherence of interplanetary coronal mass ejection sheaths at 1 AU, *J. Geophys. Res. Space Physics*, 125, e2020JA028002, doi: 10.1029/2020JA028002.

Allegrini, F., Ho, G. C., Desai, M. I., Ebert, R. W., Nelson, K., and Ogasawara, K. (2016), A comprehensive suite of suprathermal ion sensors, *J. Geophys. Res. Space Physics*, 121, 11,637– 11,646, doi: 10.1002/2016JA022531.

Allen, R. C., D. Lario, D. Odstrcil, G. C. Ho, L. K. Jian, et al. (2020) Solar wind streams and string interaction regions observed by the Parker Solar Probe with corresponding observations at 1 au, *The Astrophysical Journal Supplements*, 246, 36, doi: 10.3847/1538-4365/ab578f.

Allen, R. C., G. C. Ho, G. M. Mason, G. Li, L. K. Jian, S. K. Vines, et al. (2021a) Radial evolution of a CIR: Observations from a nearly radially aligned event between Parker Solar Probe and STEREO-A, *Geophys. Res. Lett.*, 48, e2020GL091376, doi: 10.1029/2020GL091376.

Allen, R. C., G. M. Mason, G. C. Ho, J. Rodríguez-Pacheco, R. F. Wimmer-Schweingruber, et al. (2021b), Suprathermal particles from corotating interactions regions during the first perihelion pass of Solar Orbiter, *Astron. Astrophys.*, 656, L2, doi: 10.1051/0004-6361/202039870.

Anderson, B. J., M. H. Acuńa, D. A. Lohr, J. Scheifele, A. Raval, et al. (2007) The Magnetometer Instrument on MESSENGER, *Space Sci. Rev.*, 131, doi: 10.1007/s11214-007-9246-7.

Ashraf, M. & G. Li (2019) Propagation of Scatter-free Solar Energetic Electrons in a Meandering Interplanetary Magnetic Field, *The Astrophysical Journal*, 887, 102, doi: 10.3847/1538-4357/ab4f68.

Bale, S. D., M. J. Reiner, J.-L. Bougeret, M. L. Kaiser, S. Krucker, D. E. Larson, & R. P. Lin (1999) The source region of an interplanetary type II radio burst, *Geophys. Res. Lett.*, 26, 11, doi: 10.1029/1999GL900293.

Bale, S. D., R. Ullrich, K. Goetz, N. Alster, B. Cecconi, et al. (2008) The Electric Antennas for the STEREO/WAVES Experiment, *Space Sci. Rev.*, 136, doi: 10.1007/s11214-007-9251-x.

Bale, S. D., K. Goetz, P. R. Harvey, P. Turin, J. W. Bonnell, et al. (2016) The FIELDS Instrument Suite for Solar Probe Plus, *Space Sci. Rev.*, 204, 49-82, doi: 10.1007/s11214-016-0244-5.

Bandyopadhyay, R., A. Chasapis, R. Chhiber, T. N. Parashar, B. A. Maruca, et al. (2018) Solar wind turbulence studies using MMS fast plasma investigation data, *The Astrophysical Journal*, 866, 81, doi: 10.3847/1538-4357/aade93.

Bian, N. H. & G. Li (2021) Stochastic Parker spirals in the solar wind, *The Astrophysical Journal*, 908, 45, doi: 10.3847/1538-4357/abd39a.

Borovsky, J. E. (2008) Flux tube texture of the solar wind: Stands of the magnetic carpet at 1 AU?, *J. Geophys. Res. Space Physics*, 113, A08110, doi: 10.1029/2007JA012684.

Bougeret, J. L., K. Goetz, M. L. Kaiser, S. D. Bale, P. J. Kellogg, et al. (2008) S/WAVES: The radio and plasma wave investigation on the STEREO mission, *Space Sci. Rev.*, 136, 487-528, doi: 10.1007/s11214-007-9298-8.

Burch, J. L., T. E. Moore, R. B. Torbert, & B. L. Giles (2016) Magnetospheric Multiscale Overview and Science Objectives, *Space Sci. Rev.*, 199, doi: 10.1007/s11214-015-0164-9.

Burlaga, L., E. Sittler, F. Mariani, & R. Schwenn (1981) Magnetic loop behind an interplanetary shock: Voyager, Helios, and IMP 8 observations, *J. Geophys. Res.*, 86(A8), 6673– 6684, doi: 10.1029/JA086iA08p06673.

Case, A. C., J. C. Kasper, M. L. Stevens, K. E. Korreck, K. Paulson, et al. (2020) The Solar Probe Cup on the Parker Solar Probe, *The Astrophysical Journal Supplements*, 246, 43, doi: 10.3847/1538-4365/ab5a7b.

Chen, J. H., N. A. Schwadron, E. Möbius, & M. Gorby (2015) Modeling interstellar pickup ion distributions in corotating interaction regions inside 1 AU, *J. Geophys. Res. Space Physics*, 120, 9269– 9280, doi: 10.1002/2014JA020939.

D'Amicis, R., L. Matteini, & R. Bruno (2019) On the slow solar wind with high Alfvénicity: from composition and microphysics to spectral properties, *MNRAS*, 483, 4, doi: 10.1093/mnras/sty3329.

Desai, M. I., D. G. Mitchell, J. R. Szalay, E. C. Roelof, J. Giacalone, M. E. Hill, et al. (2020) Properties of suprathermal-through-energetic He ions associated with stream interaction regions observed over the Parker Solar Probe's first two orbits, *The Astrophysical Journal Supplements*, 246(2), 56, doi: 10.3847/1538-4365/ab65ef.

Ebert, R. W., M. A. Dayeh, M. I. Desai, & G. M. Mason (2012) Corotating interaction region associated suprathermal helium enhancements at 1 au: Evidence for local acceleration at the compression region trailing edge, *The Astrophysical Journal*, 749, 73, doi: 10.1088/0004-637X/749/1/73.

Escoubet, C. P., M. Fehringer, & M. Goldstein (2001) Introduction The Cluster Mission, *Ann. Geophys.*, 19, doi: 10.5194/angeo-19-1197-2001.

Farrugia, C. J., D. B. Berdichevsky, C. Möstl, A. B. Galvin, M. Leitner, et al. (2011) Multiple, distant (40°) in situ observations of a magnetic cloud and a corotating interaction region complex, *JASP*, 73, 10, doi: 10.1016/j.jastp.2010.09.011.

Fisk, L. A., & M. A. Lee (1980) Shock acceleration of energetic particles in corotating interaction regions in the solar wind, *The Astrophysical Journal*, 237, 620– 626, doi: 10.1086/157907.

Fisk, L. A. & G. Gloeckler (2006) The common spectrum for accelerated ions in the quiet-time solar wind, *The Astrophysical Journal*, 640, L79, doi: 10.1086/503293.

Geyer, P., M. Temmer, J. Guo, & S. G. Heinemann (2021) Properties of steam interaction regions at Earth and Mars during the declining phase of SC 24, *Astron. Astrophys.*, 649, A80, doi: 10.1051/0004-6361/202040162.

Giacalone, J., J. R. Jokipii, & J. Kóta (2002). Particle acceleration in solar wind compression regions, *The Astrophysical Journal*, 573(2), 845, doi: 10.1086/340660.

Gloeckler, G., J. Geiss, H. Balsinger, P. Bedini, J. C. Cain, et al. (1992) The Solar Wind Ion Composition Spectrometer, *Astron. Astrophys. Suppl.*, 92, 2, bib: 1992A&AS...92..267G.

Grey, M., J. Westlake, S. Liang, E. Hohlfeld, A. Crew, & R. McNutt (2018) Europa PIMS Prototype Faraday Cup Development, *IEEE Aerospace Conference*, doi: 10.1109/AERO.2018.8396522.

Hu, J., G. Li, S. Fu, G. Zank, & X. Ao (2018), Modeling a Single SEP Event from Multiple Vantage Points Using the iPATH Model, *The Astrophysical Journal Lett.*, 854, L19, doi: 10.3847/2041-8213/aaabc1.

Hurford, G. (2013) X-ray imaging with collimators, masks, and grids, *in Observing Photons in Space*, doi: 10.1007/978-1-4614-7804-1.

Jian, L. K., C. T. Russell, J. G. Luhmann, R. M. Skoug, & J. T. Steinberg (2008) Evolution of Solar Wind Structures from 0.72 to 1 AU, *Adv. Space Res.*, 41, 259-266, doi: 10.1016/j.asr.2007.03.023.

Jian, L. K., J. G. Luhmann, C. T. Russell, & A. B. Galvin (2019), Solar Terrestrial Relations Observatory (STEREO) Observations of Stream Interaction Regions in 2007-2016: Relationship with Heliospheric Current Sheets, Solar Cycle Variations, and Dual Observations, *Solar Phys.*, 294, 31, doi: 10.1007/s11207-019-1416-8.

Joyce, C. J., D. J. McComas, N. A. Schwadron, E. R. Christian, M. E. Wiedenbeck, et al. (2021) Time evolution of stream interaction region energetic particle spectra in the inner heliosphere, *Astron. Astrophys. Lett.*, doi: 10.1051/0004-6361/202039330.

Kaiser, M. K., T. A. Kucera, J. M. Davila, O. C. S. Cyr, M. Guhathakurta, & E. Christian (2008) The STEREO mission: An introduction, Space Science Rev., 136, doi: 10.1007/s11214-007-9277-0.

Kasper, J. C., R. Abiad, G. Austin, M. Balat-Pichelin, S. D. Bale, et al. (2016) Solar Wind Electrons Alphas and Protons (SWEAP) Investigation: Design of the Solar Wind and Coronal Plasma Instrument Suite for Solar Probe Plus, *Space Science Rev.*, 204, 131-186, doi: 10.1007/s11214-015-0206-3.

Kilpua, E. K., J. Pomoell, A. Vourlidas, R. Vainio, J. Luhmann, et al. (2009) STEREO observations of interplanetary coronal mass ejections and prominence deflection during solar minimum period, *Ann. Geophys.*, 27, doi: 10.5194/angeo-27-4491-2009.

Klassen, A., N. Dresing, R. Gómez-Herrero, B. Heber, & R. Müller-Mellin (2016), Unexpected spatial intensity distributions and onset timing of solar electron events observed by closely spaced STEREO spacecraft, *Astron. Astrophys.*, 593, A31, doi: 10.1051/0004-6361/201628734.

Kletzing, C. A., W. S. Kurth, M. Acuña, R. J. MacDowall, R. B. Torbert, et al. (2013) The Electric and Magnetic Field Instrument Suite and Integrated Science (EMFISIS) on RBSP, *Space Sci. Rev.*, 179, doi: 10.1007/s11214-013-9993-6.

Knock, S. A., I. H. Cairns, P. A. Robinson, & Z. Kuncic (2003), Theoretically predicted properties of type II radio emission from an interplanetary foreshock, *J. Geophys. Res. Space Physics*, 108, 1126, doi: 10.1029/2002JA009508.

Kollhoff, A., A. Kouloumvakos, D. Lario, N. Dresing, R. Gómez-Herrero, et al. (2021) The first widespread solar energetic particle event observed by Solar Orbiter on 2020 November 29, *Astron. Astrophys.*, 656, A20, doi: 10.1051/0004-6361/202140937.

Koval, A. & A. Szabo (2010) Multispacecraft observations of interplanetary shock shapes on the scales of the Earth's magnetosphere, *J. Geophys. Res. Space Physics*, 115, A12105, doi:10.1029/2010JA015373.

Krucker, S., G. J. Hurford, O. Grimm, S. Kögl, H.-P. Gröbelbauer, et al. (2020) The Spectrometer/Telescope for Imaging X-rays (STIX), *Astron. Astrophys.*, 642, A15, doi: 10.1051/0004-6361/201937362.

Lazarian, A., G. L. Eyink, A. Jadari, G. Kowal, H. Li, et al. (2020) 3D turbulent reconnection: Theory, tests, and astrophysical implications, *Physics of Plasmas*, 27, 1, doi: 10.1063/1.5110603.

Li, G., L. Zhao, L. Wang, W. Liu, & X. Wu (2020) Identification of two distinct electron populations in an impulsive solar energetic electron event, *The Astrophysical Journal Lett.*, 900, L16, doi: 10.3847/2041-8213/abb098.

Liewer, P., J. Qiu, A. Vourlidas, J. R. Hall, & P. Penteado (2020) Evolution of a steamer-blowout CME as observed by imagers on Parker Solar Probe and the Solar Terrestrial Relations Observatory, *Astron. Astrophys.*, doi: 10.1051/0004-6361/202039641.

Lohr, D. A., L. J. Zanetti, B. J. Anderson, T. A. Potemra, J. R. Hayes, et al. (1997) Near Magnetic Field Investigation, Instrumentation, Spacecraft Magnetics, and Data Access, *Space Sci. Rev.*, 82, doi: 10.1023/A:1005089829882.

Lugaz, N., C. J. Farrugia, R. M. Winslow, N. Al-Haddad, A. B. Galvin, et al. (2018) On the spatial coherence of magnetic ejecta: Measurements of coronal mass ejections by multiple spacecraft longitudinally separated by 0.01 au, *The Astrophysical Journal*, 864, L7, doi: 10.3847/2041-8213/aad9f4.

Maksimovic, M., S. D. Bale, T. Chust, Y. Khotyaintsev, V. Krasnoselskikh, et al. (2020) The Solar Orbiter Radio and Plasma Waves (RPW) instrument, *Astron. Astrophys.*, 642, A12, doi: 10.1051/0004-6361/201936214.

Maruca, B. A., J. A. A. Rueda, R. Bandyopadhyay, F. B. Bianco, A. Chasapis, et al. (2021) MagneToRE: Mapping the 3-D magnetic structure of the solar wind using a large constellation of nanosatellites, *Front. Astron. Space Sci.*, doi: 10.3389/fspas.2021.665885.

Mason, G. M., & T. R. Sanderson (1999) CIR associated energetic particles in the inner middle heliosphere, *Space Sci. Rev.*, 89, 77– 90, doi: 10.1023/A:1005216516443.

Mason G. M., R. Von Steiger, R. B. Decker, M. I. Desai, J. R. Dwyer, et al. (1999) Origin, Injection, and Acceleration of CIR Particles: Observations. In: Balogh A., Gosling J.T., Jokipii J.R., Kallenbach R., Kunow H. (Eds.) *Corotating Interaction Regions. Space Sciences Series of ISSI*, vol 7. Springer, Dordrecht, doi: 10.1007/978-94-017-1179-1_16.

Mason, G. M., M. I. Desai, U. Mall, A. Korth, R. Bucik, T. T. von Rosenvinge, et al. (2009). In situ observations if CIRs on STEREO, wind, and ACE during 2007-2008, *Solar Physics*, 256, 393– 408, doi: 10.1007/s11207-009-9367-0.

Mazur, J. E., G. M. Mason, J. R. Dwyer, J. Giacalone, J. R. Jokipii, & E. C. Stone (2000) Interplanetary Magnetic Field Line Mixing Deduced from Impulsive Solar Flare Particles, *The Astrophysical Journal Lett.*, 532, L79-L82, doi: 10.1086/312561.

Murphy, N., E. J. Smith, & N. A. Schwadron (2002) Strongly underwound magnetic fields in co-rotating rarefaction regions: Observations and implications, *Geophys. Res. Lett.*, 29(22), 2066, doi: 10.1029/2002GL015164.

NAS (2012), Solar and Space Physics: A Science for a Technological Society, *National Academics Press*, doi: 10.17226/13060.

NASA (2014), Our Dynamic Space Environment: Heliophysics Science and Technology Roadmap for 2014-2033, url: https://smd-prod.s3.amazonaws.com/science-red/s3fs-public/atoms/files/2014_HelioRoadmap_Final_Reduced_0.pdf.

Ness, N. F., K. W. Behannon, R. P. Lepping, and K. H. Schatten (1971), Use of two magnetometers for magnetic field measurements on a spacecraft, *J. Geophys. Res.*, 76, doi: 10.1029/JA076i016p03564.

Neugebauer, M. & J. Giacalone (2005) Multispacecraft observations of interplanetary shocks: Nonplanarity and energetic particles, *J. Geophys. Res.*, 110, A12106, doi: 10.1029/2005JA011380.

Neugebauer, M., J. Giacalone, E. Chollet, & D. Lario (2006), Variability of low-energy ion flux profiles on interplanetary shock fronts, *J. Geophys. Res. Space Physics*, 111, A12107, doi: 10.1029/2006JA011832.

Owens, M. J., M. Lockwood, & L. A. Barnard (2017) Coronal mass ejections are not coherent magnetohydrodynamic structures, *Sci. Rep.*, 7, 4152, doi: 10.1038/s41598-017-04546-3.

Perrone, D., D. Stansby, T. S. Horbury, & L. Matteini (2019) Radial evolution of the solar wind in pure high-speed streams: HELIOS revised observations, *MNRAS*, 483, 3, doi: 10.1093/mnras/sty3348.

Pulupa, M. & S. D. Bale (2008) Structuring on interplanetary shock fronts: Type II radio burst source regions, *The Astrophysical Journal*, 676, 1330, doi: 10.1086/526405.

Richter, A. K., & A. H. Luttrell (1986) Superposed epoch analysis of corotating interaction regions at 0.3 and 1.0 AU: A comparative study, *J. Geophys. Res. Space Physics*, 91(A5), 5873– 5878, doi: 10.1029/JA091iA05p05873.

Roberts, O. W., R. Nakamura, K. Torkar, Y. Narita, J. C. Holmes, et al. (2020) Sub-ion Scale Compressive Turbulence in the Solar Wind: MMS Spacecraft Potential Observations, *The Astrophysical Journal Supplements*, 250, 35, doi: 10.3847/1538-4365/abb45d.

Rodríguez-Pacheco, J., R. F. Wimmer-Schweingruber, G. M. Mason, G. C. Ho, S. Sánchez-Prieto, et al. (2020) The Energetic Particle Detector: Energetic particle instrument suite for the Solar Orbiter mission, *Astron. Astrophys.*, 642, A7, doi: 10.1051/0004-6361/201935287.

Schwadron, N. A. (2002) An explanation for strongly underwound magnetic field in co-rotating rarefaction regions and its relationship to footpoint motion on the sun, *Geophys. Res. Lett.*, 29(14), 1663, doi: 10.1029/2002GL015028.

Schwadron, N. A., C. J. Joyce, A. Aly, C. M. S. Cohen, M. I. Desai, D. J. McComas, et al. (2020) A new view of energetic particles from stream interaction regions observed by Parker Solar Probe, *Astron. Astrophys.*, doi: 10.1051/0004-6361/202039352.

Schwenn, R. (1990) Large-scale structure of the interplanetary medium, In R. Schwenn & E. Marsch (Eds.), *Physics of the inner heliosphere I. Physics and chemistry in space, space and solar physics* (Vol. 20). Berlin, Heidelberg: Springer, doi: 10.1007/978-3-642-75361-9_3.

Tritschler, A., T. R. Rimmele, S. Berukoff, R. Casini, J. R. Kuhn, et al. (2016) Kaniel K. Unouye Solar Telescope: High-resolution observing of the dynamic Sun, *Astron. Nachr.*, 337, doi: 10.1002/asna.201612434.

Warfield, K. and R. Kevin (1998) The JPL Advanced Projects Design Team Space Instrument Cost Model: An Objective Multivariate Approach, *First Annual Joint ISPA/SCEA International Conference*, Toronto, ON, Canada.

Whitley, S., M. Hahn, & N. Powers (2013) The Incremental Cost of One or More Copies – Quantifying Efficiencies from Building Spacecraft and Instrument Constellations, *AIAA/Utah State University Small Satellite Conference*.

Whittlesey, P. L., D. E. Larson, J. C. Kasper, J. Halekas, M. Abatcha, et al. (2020) The Solar Probe Analyzers – Electrons on the Parker Solar Probe, *The Astrophysical Journal Supplements*, doi: 10.3847/1538-4365/ab7370.

Wimmer-Schweingruber, R. F., N. P. Janitzek, D. Pacheco, I. Cernuda, F. Espinosa Lara, et al. (2021) First year of energetic particle measurements in the inner heliosphere with Solar Orbiter's Energetic Particle Detector, *Astron. Astrophys.*, 656, A22, doi: 10.1051/0004-6361/202140940.

Verscharen, D., K. G. Klein, & B. A. Maruca (2019) The Multi-scale nature of the Solar Wind, *Living Reviews in Solar Physics*, 16, 5, doi: 10.1007/s41116-019-0021-0.

Zhao, L., G. Li, R. W. Ebert, M. A. Dayeh, M. I. Desai, G. M. Mason, Z. Wu, & Y. Chen (2016), Modeling transport of energetic particles in corotating interaction regions: A case study, *J. Geophys. Res. Space Physics*, 121, 77– 92, doi:10.1002/2015JA021762.

Zhao, L., G. Li, M. Zhang, L. Wang, A. Moradi, & F. Effenberger (2019) Statistical analysis of interplanetary magnetic field path lengths from solar energetic electron events observed by WIND, *The Astrophysical Journal*, 878, 107, doi: 10.3847/1538-4357/ab2041.

List of Acronyms

AC	Alternating Current
ACE	Advanced Composition Explorer
ACS	Attitude Control System
APL	Johns Hopkins Applied Physics Laboratory
AR	Anti-reflective
BOL	Beginning of Life
C&DH	Command and Data Handling
CBE	Current Best Estimate
CFDP	CCSDS File Delivery Protocol
CIR	Corotating Interaction Region
CME	Coronal Mass Ejection
CONOPS	Concept of Operations
COTS	Commercial Off-the-Shelf
CPU	Central Processing Unit
CtoC	Cost-to-Copy
DART	Double Asteroid Redirection Test
DPU	Digital Processing Unit
DSN	Deep Space Network
EELV	Evolved Expendable Launch Vehicle
EOL	End of Life
EPT	Energetic Particle Telescope
ESA	European Space Agency
FGM	Fluxgate Magnetometer
FOV	Field of View
FSW	Flight Software
FVDA	Fractional Velocity Dispersion Analysis
GDS	Ground Data System
GOES	Geostationary Operational Environmental Satellite
GSE	General Support Equipment
HGA	High-Gain Antenna
HIS	Heavy Ion Sensor
HSO	Heliophysics System Observatory
HVPS	High-Voltage Power Supply
IEM	Integrated Electronics Module

IMAP	Interstellar Mapping and Acceleration Probe
IMF	Interplanetary Magnetic Field
IMU	Inertial Measurement Unit
I&T	Integration and Testing
JEDI	Jupiter Energetic-Particle Detector Instrument
JPL	Jet Propulsion Laboratory
LGA	Low-Gain Antennas
LRR	Launch Readiness Review
LV	Launch Vehicle
LV&S	Launch Vehicle and Services
MCP	Microchannel Plate
MEL	Master Equipment List
MEPS	Medium Energy Particle Spectrometer
MIDEX	Medium-Class Explorer
MLI	Multilayer Insulation
MMS	Magnetospheric Multiscale Mission
MUSE	Multi-slit Solar Explorer
NNSII	NASA New Start Inflation Indices
NOAA	National Oceanic and Atmospheric Administration
NRE	Nonrecurring Engineering
PDR	Preliminary Design Review
PIMS	Plasma Instrument for Magnetic Sounding
PLA	Payload Adaptor
PSE	Power System Electronics
PSP	Parker Solar Probe
PSU	Power Switching Unit
PUNCH	Polarimeter to Unify the Corona and Heliosphere
QMS	Quality Management System
RF	Radio Frequency
RIU	Remote Interface Unit
RPW	Radio Plasma Waves
RSS	Residual Sum of Squares
SBC	Single Board Computer
SCIF	Spacecraft Interface Card
SEP	Solar Energetic Particle
SG	Science Goal

SI&T	System Integration & Testing
SIR	Stream Interaction Region
SIR	System Integration Review
SIS	Suprathermal Ion Spectrograph
SOC	Science Operations Center
SPICES	Solar wind and Pickup Ion Composition-Energy Spectrometer
SSD	Solid-State Detector
STEREO	Solar Terrestrial Relations Observatory
STIX	Spectrometer Telescope for Imaging X-rays
STM	Science Traceability Matrix
STP	Solar Terrestrial Probes
SWICS	Solar Wind Ion Composition Spectrometer
TAC	Thruster/Actuator Controller
ToF	Time of Flight
TP	TruePlanning
TRL	Technology Readiness Level
TWTA	Traveling-Wave Tube Amplifier
VAP	Van Allen Probes
WBS	Work Breakdown Structure